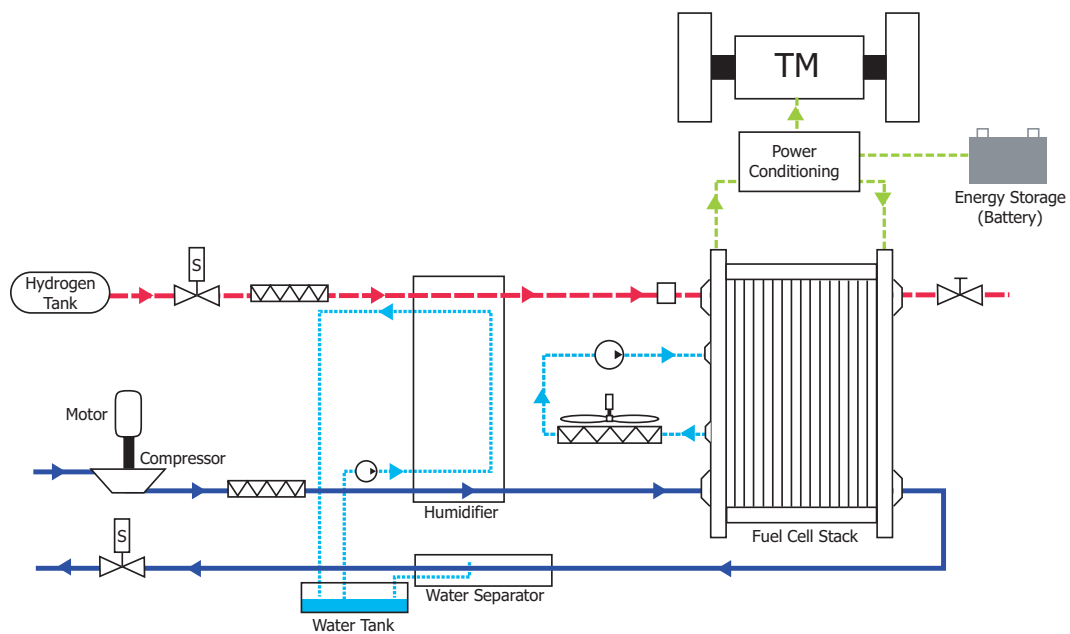Department of Mechanical Engineering
The University of Michigan, Ann Arbor, Michigan

MODELING AND CONTROL OF FUEL CELL SYSTEMS AND FUEL PROCESSORS

Jay Tawee Pukrushpan

MODELING AND CONTROL OF FUEL CELL SYSTEMS AND FUEL PROCESSORS

by

Jay Tawee Pukrushpan

A dissertation submitted in partial fulfillment
of the requirements for the degree of
Doctor of Philosophy
(Mechanical Engineering)
in The University of Michigan
2003

Doctoral Committee:

Associate Professor Anna Stefanopoulou, Co-Chair
Associate Professor Huei Peng, Co-Chair
Professor Dionissios Assanis
Professor Erdogan Gulari

ABSTRACT

MODELING AND CONTROL OF FUEL CELL SYSTEMS AND FUEL PROCESSORS

by

Jay Tawee Pukrushpan

Co-Chairs: Anna Stefanopoulou and Huei Peng

Fuel cell systems offer clean and efficient energy production and are currently under intensive development by several manufacturers for both stationary and mobile applications. The viability, efficiency, and robustness of this technology depend on understanding, predicting, and controlling the unique transient behavior of the fuel cell system. In this thesis, we employ phenomenological modeling and multivariable control techniques to provide fast and consistent system dynamic behavior. Moreover, a framework for analyzing and evaluating different control architectures and sensor sets is provided.

Two fuel cell related control problems are investigated in this study, namely, the control of the cathode oxygen supply for a high-pressure direct hydrogen Fuel Cell System (FCS) and control of the anode hydrogen supply from a natural gas Fuel Processor System (FPS). System dynamic analysis and control design is carried out using model-based linear control approaches. A system level dynamic model suitable for each control problem is developed from physics-based component models. The transient behavior captured in the model includes flow characteristics, inertia dynamics, lumped-volume manifold filling dynamics, time evolving spatially-homogeneous reactant pressure or mole fraction, membrane humidity, and the Catalytic Partial Oxidation (CPOX) reactor temperature.

The goal of the FCS control problem is to effectively regulate the oxygen concentration in the cathode by quickly and accurately replenishing oxygen depleted during power generation. The features and limitations of different control configurations and the effect of various measurement on the control performance are examined. For example, an observability analysis suggests using the stack voltage measurement as feedback to the observer-based controller to improve the closed loop performance. The objective of the FPS control system is to regulate both the CPOX temperature and anode hydrogen concentration. Linear multivariable system analysis is used to identify the limitation of a decentralized controller and to design a model-based multivariable controller with significantly improved performance in CPOX temperature regulation. Further analysis unveils the critical controller cross-coupling term that contributes to the superior performance of the multivariable controller.

To my parents

Acknowledgements

First and foremost, I would like to express my respect and sincere gratitude to both of my advisors, Dr. Huei Peng and Dr. Anna Stefanopoulou. Without their invaluable guidance, encouragement, insightful comments and extraordinary patience, this work would never have been possible. I would also like to express my gratitude to the other members of my committee, Dr. Dennis Assanis and Dr. Erdogan Gulari, for their helpful advice and comments. Thanks are also due to Dr. James Freudenberg for his help and advice.

I am deeply indebted to the Royal Thai government for granting me a scholarship for my graduate study and to the Department of Mechanical Engineering at Kasetsart University for supporting my study leave. I would also like to acknowledge the Automotive Research Center at the University of Michigan, and the National Science Foundation for their financial support over the past two years.

It was an honor to have the opportunity to work at the United Technology Research Center during the past summer. I wish to thank Subbarao Varigonda, Jonas Eborn, Thordur Runolfsson, Christoph Haugstetter, Lars Pedersen, Shubhro Ghosh, and Scott Bortoff, for their help and for sharing with me their insightful knowledge of fuel processor systems.

I am grateful to Scott Staley, Doug Bell, Woong-Chul Yang, and James Adams at the Ford Motor Company for their helpful suggestions and for providing me with valuable data on the fuel cell. I also owe a note of thanks to Larry Mianzo and Shankar Raman for allowing me to earn valuable research and work experience during my internship at Visteon Corporation.

At the University of Michigan, I have worked alongside many talented students. My thanks go to all of them for their kindness and friendship, but particularly to Chan-Chiao (Joe) Lin, Hyungpil Moon, Kangwon (Wayne) Lee, Ali Yigit Ungoren, Bo-Chiuan Chen, Ashish Deshpande, James Dunn, Dongmei Chen, and Konstantinos Varsos. I greatly appreciate all the good times we had together.

My deepest thanks go to my dearest parents, Dr. Thanong and Dr. Lukchon, for their hard work and great sacrifices to see that their children got a good education, and above all, for always being there for me. I extend my thanks to Parnchat (Pe), my wonderful sister and my best friend. Lastly, my thanks and appreciation go to my wife, Chutamanee. Her love, understanding and companionship are elements that have sustained me throughout my graduate career.

Contents

Chapter 1

Background and Introduction

Fuel Cells are electrochemical devices that convert the chemical energy of a gaseous fuel directly into electricity and are widely regarded as a potential alternative stationary and mobile power source. They complement heat engines and reduce the ubiquitous dependence on fossil fuels and thus have significant environmental and national security implications. As such, they are actively studied for commercial stationary power generation, residential applications, and transportation technologies. Recent study has shown that, in the United States, Carbon dioxide (CO_2) accounts for more than 80% of greenhouse gases released [41] and the transportation sector is responsible for 32% of the overall CO_2 emission [32]. In this thesis, we concentrate on the fuel cell control requirement during transients. Application of fuel cells in automotive powertrains is emphasized, partly because ground vehicle propulsion conditions present the most challenging control problem, and partly due to their importance in global fuel consumption and emission generation.

Fuel cell stack systems are under intensive development by several manufacturers, with the Polymer Electrolyte Membrane (PEM) Fuel Cells (also known as Proton Exchange Membrane Fuel Cells) currently considered by many to be in a relatively more developed stage for ground vehicle applications. PEM Fuel Cells have high power density, solid electrolyte, long cell and stack life, as well as low corrosion. They have greater efficiency when compared to heat engines and their use in modular electricity generation and propulsion of electric vehicles is promising [62]. Fuel cell efficiency is high at partial loads which correspond to the majority of urban and highway driving scenarios [88]. At a nominal driving speed (30 mph) the efficiency of a fuel cell electric drive using direct hydrogen from natural gas is two times higher than that of a conventional internal combustion engine [91]. Using pure hydrogen as fuel can eliminate local emissions problems in densely populated urban environments. A hydrogen generation and distribution infrastructure based on renewable energy from wind, water, and sun, or fuel processors will help reduce our dependency on fossil fuels.

To compete with the ICE engines, however, fuel cell systems must operate and function at least as well as conventional engine. Transient behavior is a key requirement for the success of fuel cell vehicles. The fuel cell system power response is limited only by the air and hydrogen feed, flow and pressure regulation, and heat and water management. As current is instantaneously drawn from the load source connected to the fuel cell stack, heat and water are generated, whereas oxygen is depleted. During this transient, the fuel cell stack breathing control system is required to maintain optimal temperature, membrane hydration, and partial pressure of the reactants across the membrane in order to avoid detrimental degradation of the stack voltage, and thus, efficiency reduction. These critical fuel cell parameters can be controlled for a wide range of current, and thus power, by a series of actuators such as valves, pumps, compressor motors, expander vanes, fan motors, humidifiers, and condensers. The resulting auxiliary actuator system is needed to make fine and fast adjustments to satisfy performance, safety, and reliability standards that are independent of age and operating conditions. Model-based dynamic analysis and control design give insight of the subsystem interactions and control design limitations. It also provides guidelines for sensor selection and control coordination between subsystems. Creating a control-oriented dynamic model of the overall system is an essential

first step not only for understanding of system behavior but also for the development and design of the model-based control methodologies. The goal of this research is to develop physic-based dynamic models of fuel cell systems and fuel processor systems and then apply multivariable control techniques to study their behavior. The analysis will give insight into the control design limitations and provide guidelines for the necessary controller structure and system re-design.

1.1   Fuel Cell

We summarize here the principle and potential benefits of fuel cell power generation. The fuel cell principle was discovered in 1839 by William R. Grove, a British physicist [55]. A fuel cell consists of an electrolyte sandwiched between two electrodes. The electrolyte has a special property that allows positive ions (protons) to pass through while blocking electrons. Hydrogen gas passes over one electrode, called an anode, and with the help of a catalyst, separates into electrons and hydrogen protons (Figure 1.1)

$$2H_2 \Rightarrow 4H^+ + 4e^- \tag{1.1}$$

The protons flow to the other electrode, called a cathode, through the electrolyte while the electrons flow through an external circuit, thus creating electricity. The hydrogen protons and electrons combine
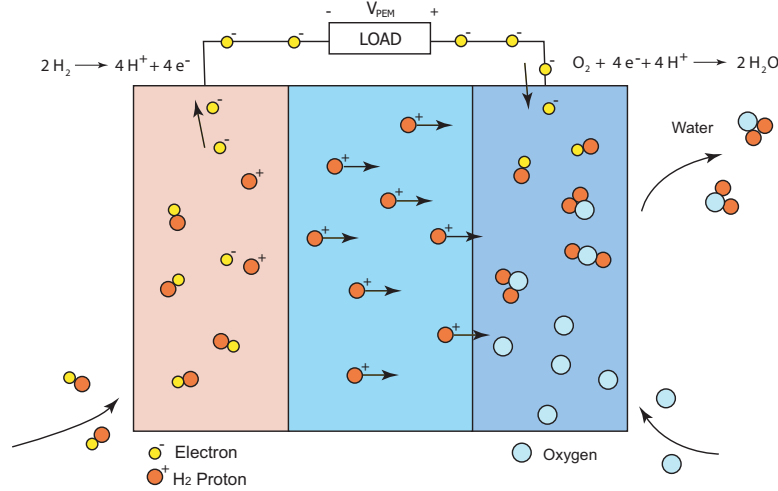
Figure 1.1: Fuel cell reaction

with oxygen flow through the cathode, and produce water.

$$O_2 + 4H^+ + 4e^- \Rightarrow 2H_2O \tag{1.2}$$

The overall reaction of the fuel cell is therefore

$$2H_2 + O_2 \Rightarrow 2H_2O \tag{1.3}$$

The voltage produced from one cell is between 0 to 1 volts [69] depending on fuel cell operating conditions and the size of load connected to the fuel cell. The typical value of the fuel cell voltage is about 0.7 volts. To get higher voltage, multiple cells are stacked in series. The total stack voltage is the number of cells multiplied by the average cell voltage. Like other electrical devices, there are electrical resistances in the fuel cell. The loss associated with the resistance is dissipated in the form of heat. In other words, heat is released from the fuel cell reaction.

Fuel cells have several advantages over internal combustion engines (ICE) and batteries. To generate mechanical energy, the ICE first converts fuel energy to thermal energy by combusting fuel with

oxygen at high temperature. The thermal energy is then used to generate mechanical energy. Since thermal energy is involved, the efficiency of the conversion process is limited by the Carnot Cycle [106]. Unlike ICE, fuel cells directly convert fuel energy to electrical energy and its maximum efficiency is not subjected to Carnot Cycle limitations. Higher energy conversion efficiency can potentially be achieved by fuel cells. If hydrogen is used as fuel, the outcome of the fuel cell reaction is water and heat. Therefore, fuel cells are considered to be a zero emission power generator. They do not create pollutants such as hydrocarbon or oxide of nitrogen. A battery is also an electrochemical device that converts chemical energy directly to electricity. However, the battery reactants are stored internally and when used up, the battery must be recharged or replaced. The reactants of fuel cell are stored externally. Oxygen is typically taken from atmospheric air and hydrogen is stored in high-pressure or cryogenic tanks which can be refueled. Refueling fuel tanks requires significantly less time than recharging batteries [106].

There are different types of fuel cells, distinguished mainly by the type of electrolyte used. The differences in cell characteristics, such as cell material, operating temperature, and fuel diversity, make each type of fuel cell suitable for different applications. It is known that Polymer Electrolyte Membrane Fuel Cells (PEMFC) are suitable for automobile applications. PEM fuel cells have high power density, a solid electrolyte, long life, as well as low corrosion. PEM fuel cells operate in the temperature range of 50 - 100°C which allows safer operation and eliminates the need of thermal insulation. The polymer electrolyte membrane is an electronic insulator but an excellent conductor of hydrogen ions. The typical membrane material consists of a fluorocarbon backbone to which sulfonic acid groups ($SO_3^- H^+$) are attached [106]. When the membrane becomes hydrated, the hydrogen ions (H^+) in the sulfonic group are mobile. Depending on membrane manufacturers and the versions of the membrane, properties of the membranes differ. The thickness of the membrane varies from 50 to 175 microns, which is approximately 2 to 7 papers thick [106]. The membrane is sandwiched between two electrodes (anode and cathode) made from a highly conducting material such as porous graphite. A small amount of platinum is applied to the surface of the anode and cathode to help increase the rate of reaction. The three components (anode, electrolyte, and cathode) are sealed together to form a single membrane electrolyte assembly (MEA), shown in Figure 1.2, which is typically less than a millimeter thick.
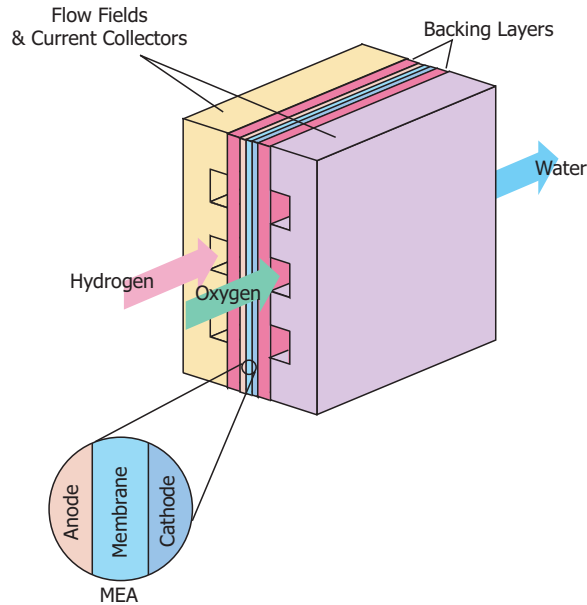

Figure 1.2: Fuel cell structure

The MEA is sandwiched by two backing layers made from porous carbon. The porous nature of

the backing layer ensures effective diffusion of each reactant gas to the catalyst site on the MEA. The outer surface of the backing layer is pressed against the flow field plates which serve as both reactant gas flow field and current collector. The plate is made of a light-weight, strong, gas impermeable, electron conducting material such as graphite or composite materials. The other side of the flow field plate is connected to the next cell. The number of cells stacked in one fuel cell stack depends on the power requirement of the stack, which varies across different applications.

Depending on its operating condition, a single fuel cell can provide a voltage from 0 to 1.0 volts with the nominal value of 0.7 volts. Typical characteristics of fuel cells are normally given in the form of a polarization curve, shown in Figure 1.3, which is a plot of cell voltage versus cell current density (current per unit cell active area). The differences between actual voltage and the ideal voltage of the fuel cell represent the loss in the cell. As shown in Figure 1.3, as more current is drawn from the fuel cell, the voltage decreases, due to fuel cell electrical resistance, inefficient reactant gas transport and low reaction rate. Since lower voltage indicates lower efficiency of the fuel cell, low load (low current) operation is preferred. However, this will increase the fuel cell volume and weight. Moreover, constant operation at low load is not practical in automobile applications where frequent load changes are demanded. The polarization curve shown in Figure 1.3 is for a specific operating condition. The curve varies with different operating conditions, including different pressure, temperature, reactant partial pressure, and membrane humidity. An example of pressure effects on the polarization curve is shown in Figure 1.4. The data, kindly given to us by the Ford Research Laboratory [29], are from a generic PEM fuel cell stack used in a fuel cell prototype vehicle.
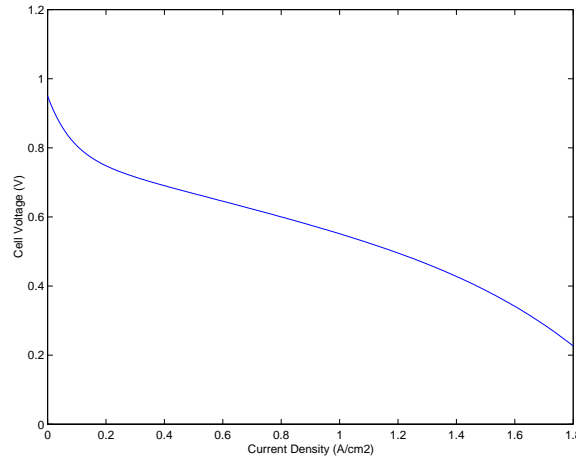
Figure 1.3: Typical fuel cell polarization curve

1.2   Fuel Cell Propulsion System for Automobiles

In order to be used to power an automobile, a fuel cell stack needs to be integrated with other components to form a fuel cell system. The diagram in Figure 1.5 shows the minimal components required for a pressurized fuel cell engine. The fuel cell stack requires four flow systems: (i) hydrogen supply system to the anode (ii) air supply system to the cathode (iii) de-ionized water serving as coolant in the stack cooling channel and (iv) de-ionized water supply to the humidifier to humidify the hydrogen and the air flows. These four subsystems are denoted by control inputs u_1 to u_4 in Figure 1.5.

Operation at high pressure significantly improves the reaction rate, and thus, the fuel cell efficiency and power density [8], a compressor and an electric drive motor are needed to compress air to a desired pressure level. Due to high temperature of the air leaving the compressor, an air cooler is needed to reduce the air temperature before it enters the stack. A humidifier is used to add vapor into the
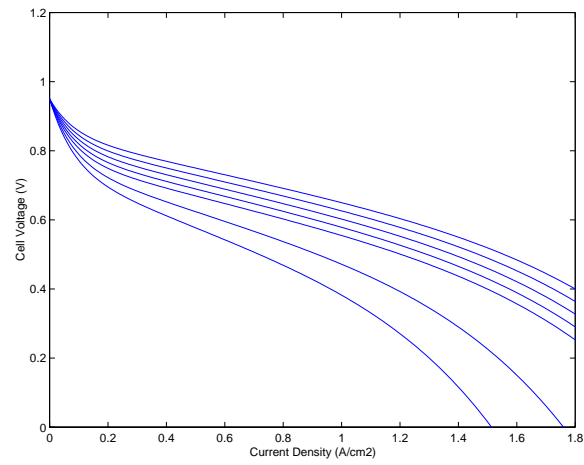
Figure 1.4: Fuel cell polarization for different operating pressures
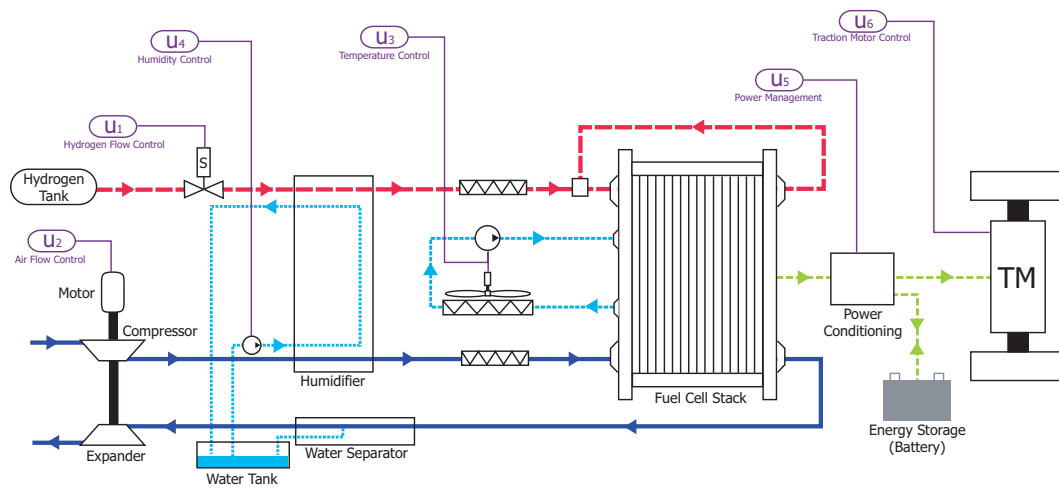
Figure 1.5: Automotive fuel cell propulsion system

air flow, as illustrated in Figure 1.5, in order to prevent dehydration of the membrane. As the air leaves the stack, it carries vapor produced in the fuel cell. For an automotive fuel cell system, a water separator is needed in order to recover the water. On the anode side, hydrogen is supplied from a container which can store pressurized hydrogen or liquid hydrogen. A valve is used to control the flow rate of hydrogen. A humidifier is also used to humidify the hydrogen flow. Since the temperature of the stack must be maintained below 100 $^\circ C$ for the membrane to be properly humidified, excessive heat released in the fuel cell reaction is removed by a de-ionized water coolant. As illustrated in Figure 1.5, the coolant leaving the stack then passes through a heat exchanger or a radiator in order to remove heat from the system. A power conditioner, denoted as control input u_5 in Figure 1.5, is frequently needed since the voltage of the fuel cell stack varies significantly and is not suitable for typical electronic components nor traction motors. The conditioned power is supplied to the traction motor connected to the vehicle drivetrain. The control input u_6 in Figure 1.5 represents the control of traction motor drive.

Reactant flow rate, total pressure, reactant partial pressure, temperature, and membrane humidity are the main parameters that need to be regulated in order to ensure (i) fast transient response, consistent warm-ups, and safe shutdown and (ii) robustness and adaptation to changing power. The main control devices are the compressor motor for the air flow and pressure regulations, the valve for hydrogen flow rate and pressure regulations, the water pump or radiator fan speed for the temperature regulations, and the humidifier for the humidity control. However, the changes in the parameters are not independent. Changes in one parameter influence the others. For example, consider the following: an increase in air flow rate can cause an increase in air pressure but can also vary the amount of vapor and heat entering and leaving the stack, thus affecting the humidity of the membrane and temperature of the stack. Stack temperature also affects the humidity of the air and hydrogen inside the stack since the vapor saturation pressure depends strongly on the temperature.

During vehicle operation, various load levels as well as sudden load changes are expected. For fuel cell vehicles to be commercialized, these vehicle operations need to be well handled. During this transient, the control system is required to maintain optimal temperature, membrane hydration, and partial pressure of the reactants in order to avoid detrimental degradation of the fuel cell voltage, and thus, an efficiency reduction and fuel cell life shortening.

1.3   System Interactions

Precise control of the reactant flow and pressure, stack temperature, and membrane humidity is critical to the viability, efficiency, and robustness of fuel cell propulsion systems. The resulting task is complex because of subsystem interactions and conflicting objectives. The overall system could be partitioned into four subsystems. Each system has a corresponding control objective and also interactions with other subsystems. The subsystems are the reactant flow, the heat and temperature, the water management, and the power management subsystems.

1.3.1   Reactant Flow Subsystem

The reactant flow subsystem consists of hydrogen supply and air supply loops. As the vehicle traction motor draws current, hydrogen and oxygen become depleted in the fuel cell stack. The hydrogen flow in the anode and the air flow in the cathode are adjusted using the valve and compressor motor commands, respectively. The control objective is to provide sufficient reactant flows (to keep the desired excess ratio) to ensure fast transient responses and to minimize auxiliary power consumption. The non-minimum phase behavior of the fuel cell power output to changes in compressor motor input limits the closed-loop bandwidth of this loop. A few early patents [75, 81] recognize this difficulty and avoid a slow response by relying on a feedforward map that must be tuned at different ambient conditions [83]. Several experimental systems use a fixed speed motor which supplies air flow that satisfies maximum traction requirements. This results in unnecessary auxiliary power consumption during low load operations where less flow is needed.

1.3.2 Heat and Temperature Subsystem

The heat and temperature subsystem includes the fuel cell stack cooling system and the reactant temperature system. As current is drawn by the traction motor, heat is generated in the fuel cell. The thermal management of the fuel cell stack is more challenging than that of the internal combustion engine. First, de-ionized water is used as coolant in the stack instead of an effective coolant fluid. Second, the PEM fuel cell is designed to operate at the temperature around $80°C$. Therefore, the exhaust air exiting the stack, which has temperature around $80°C$, has less ability to carry out heat than the ICE exhaust gas which is over $500°C$ [59]. Heat rejection for the fuel cell stack is therefore a responsibility of the cooling system. Furthermore, the low temperature difference between the stack and the water coolant limits the effectiveness of the heat transfer from the stack to the coolant. With the stack size required for passenger vehicles, the heat generated cannot be passively dissipated by air convection and radiation through the external surface of the stack. This requires active cooling through the reactant flow rate and the cooling system. Apart from the water coolant flow rate and its temperature, the temperature of inlet reactant air also affects the temperature of the stack. The heat management system can vary the speed of the cooling fan and the recirculation pump in coordination with adjusting a by-pass valve. The goal of thermal management is fast warm-up with no stack temperature overshoot and low auxiliary fan and pump power.

1.3.3 Water Management Subsystem

The task of the water management system is to maintain hydration of the polymer membrane and to balance water usage/comsumption in the system. The amount of reactant flow and the water injected into the anode and cathode flow streams affect the humidity of the membrane. Dry membranes and flooded fuel cells cause high polarization losses. As the current is drawn from the fuel cell, water molecules are both produced in the cathode and dragged from the anode to the cathode by the hydrogen protons. As the concentration of water in the cathode increases, the concentration gradient causes water to diffuse from the cathode to the anode. Perturbation in fuel cell humidity can be caused by different mechanisms: water generated while load increases, changes in the absolute and relative reactant pressure across the membrane, changes in air flow rate, and changes in stack temperature, which change the vapor saturation pressure. These mechanisms indicate strong and nonlinear interactions among the humidity control tasks, the reactant flow management loop, the heat management loop, and the power management loop. A 20-40% drop in voltage can occur if there is no proper humidification control [24].

1.3.4 Power Management Subsystem

The power management subsystem controls the power drawn from the fuel cell stack. Without considering power management, the load current can be viewed as a disturbance to the fuel cell system. However, as shown above, the current drawn has a direct impact on other subsystems. If a battery is used as another power source in the system, the power management between two power sources could be applied with the objective of giving a satisfactory vehicle transient response and assisting the fuel cell system.

1.3.5 Fuel Processor Subsystem

Inadequate infrastructure for hydrogen refueling, distribution, and storage makes fuel processor technology an important part of the fuel cell system. Methanol, gasoline, and natural gas are examples of fuels being considered as fuel cell energy sources. Figure 1.6 illustrates different processes involved in converting carbon-based fuel to hydrogen [18, 23]. Interactions between the components and many additional control actuators in the fuel processor introduce additional complexity to the control problem. In addition to the fuel cell variables, the fuel processor variables that require precise control include the temperature of the reactors and the concentration of hydrogen and carbon-monoxide in the gas stream.
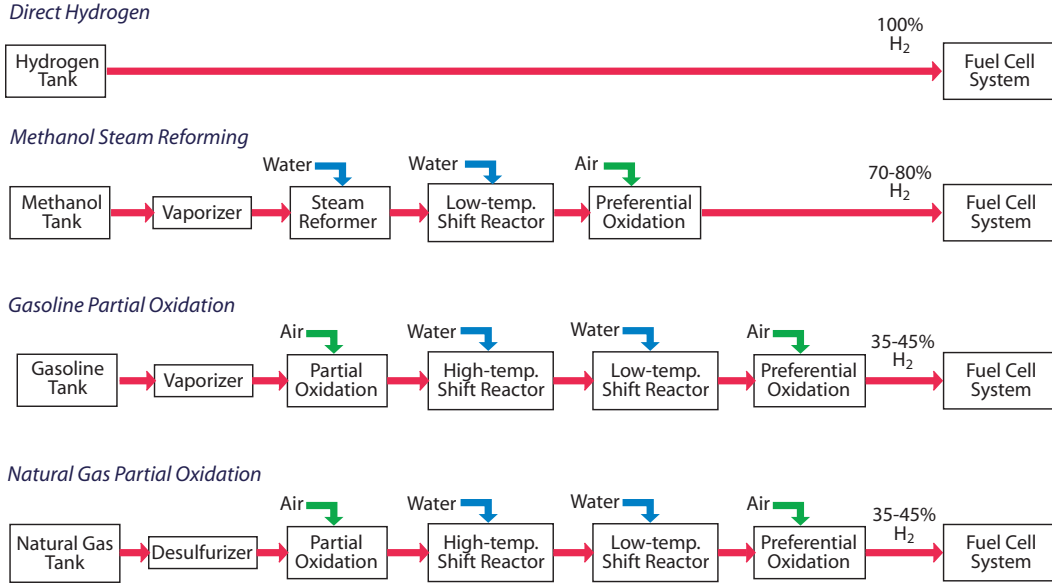
Figure 1.6: Fuel sources for fuel cell systems [18, 23]

1.4 Literature Review

To achieve high efficiency and a long life cycle of the fuel cell stack, the reactant gas supply and water and heat subsystems need to be properly controlled both during steady-state and transient operations. During vehicle transient operation, delivering torque to meet driveability performance while meeting safety and efficiency criteria is of concern [102]. Yang et al. [111] described the control challenges and the methodologies being used in fuel cell prototype vehicles. A variety of control problems were identified and discussed. Another report [64] discussed the importance of subsystem management, or balance of plant, and control needed for each subsystem. The difficulties of the thermal management system are explained in [46]. The interactions between thermal management and stack performance are also addressed. Several integration issues and trade-offs within the fuel cell system are discussed. The impact of stack water and thermal managements on the fuel cell system is studied in [10]. In [47] and [12], fuel cell stack in-vehicle performance was shown to be lower than performance on a laboratory test-stand due to the discrepancy in fuel cell operating conditions, particularly inadequate air supply and insufficient humidification. The need for control strategies that can respond fast and can regulate the fuel cell operating conditions was emphasized.

Despite a large number of publications on fuel cell modeling, models of fuel cell systems suitable for control studies are still lacking. The models developed in the literature can be classified into three main categories, namely, fuel cell performance models, steady-state fuel cell system models, and dynamic fuel cell system models.

Most of the publications on fuel cell modeling have targeted the fuel cell performance prediction. Models in this category are mostly steady-state. They are developed at the cell level and include spatial variations of the fuel cell parameters. Complex electrochemical, thermodynamic, and fluid mechanics principles are used to develop these models. The performance or efficiency of the fuel cell under different steady-state operating conditions can be determined using this type of model. The main purposes of these models are to design the fuel cell components and to choose the fuel cell operating points. While these models are not suitable for control studies, they establish the fundamental effects of operating parameters, such as pressure and temperature, on the fuel cell voltage. Several publications [5, 65, 77, 78] presented the formulation of fuel cell resistances which is used to predict fuel cell polarization characteristics at different operating conditions. Mass transport of gas and water was also included in several publications with both one-dimensional [4, 16, 17, 100] and two-dimensional

models [31, 56, 95]. Springer et al. [100] also presented a model predicting net water flow per proton through the membrane and the increase in membrane resistance due to the membrane water content. Many publications addressed the water and thermal management of the fuel cell. Nguyen and White [82] developed a model investigating the effectiveness of various humidification designs. Fuller and Newman [48] developed a two-dimensional mass transport model of membrane electrode assembly to examine the water, thermal, and reactant utilization of the fuel cell. Okada et al. [86] presented a method to analytically calculate water concentration profiles in the membrane. A three-dimensional numerical model that predicts the mass flow between the cathode and anode channels was presented in [39]. Bernardi [15] and Büchi [24] presented models that identify operating conditions that result in water balance in the fuel cell. Baschuk and Li [13] developed a model that includes the effect of water flooding in the cathode catalyst layer. Wöhr et al. [110] presented a dynamic model of heat and water transport in the fuel cell and showed the effects of various current density variations on the fuel cell performance. Interestingly, they showed that different rates of load changes can lead to a different level of fuel cell voltage as a result of water deficiency. Several models were developed to represent fuel cell stacks [72, 104]. In [72], the model was used to determine operating configurations. The stack model in [104] was used in the stack flow field design. A model predicting transient responses of the fuel cell stack was given in [6]. The heat transfer transient phenomena were incorporated into this model. All the papers in the above category used a combination of experiments and physical laws to derive their models.

An interesting set of papers with experimental results of fuel cell performance during dynamic excitation appeared in the literature recently. Specifically, Chu and Jiang evaluated fuel cell performance under various conditions. Different types of membrane were tested in [27] and the humidity and hydrogen flow effects were presented in [28]. The voltage-time behaviors of the fuel cell stack at constant current discharge were studied and a model representing the behavior was presented in [61]. The stack structure designs were tested in [60]. Laurencelle et al. [70] presented experimental results of fuel cell stack responses during load transitions. The transient behavior of stack voltage during positive load switching was observed in the experiment.

Steady-state system models are typically used for component sizing, static trade-off analysis, and cumulative fuel consumption or hybridization studies. The models in this category represent each component such as the compressors, heat exchangers, and fuel cell stack voltage as a static performance or efficiency map. The only dynamics considered in this type of model is the vehicle effective inertia. Barbir et al. [11] presented a steady-state model of the entire system that calculates the system and component parameters for various operating pressures, temperatures and power levels. System efficiency was also evaluated. The size of heat exchanger or radiator was determined for each system configuration. Equations presented in [45] were used to find operating strategies based on the efficiency of each individual component in an indirect methanol fuel cell system. A method to optimize the net power output was presented. The fuel cell system models in [3, 9, 19, 84] were used in fuel cell/battery hybrid studies. Fuel economy was determined and supervisory vehicle control was studied using the model in [19]. The model in [3] was used to study the trade-off between maximum acceleration and auxiliary power sources. The vehicle inertia dynamics were the only transient phenomena in this model. Sizing of the fuel cell and battery in a hybrid configuration was studied in [9]. This model was used to choose the degree of hybridization that offers high fuel economy and to study power management strategies between the fuel cell stack and battery. Steady-state models of the fuel cell stack, air supply system, and thermal management system were incorporated into vehicle simulation program in [94]. The model was used to predict the acceleration, braking and drive cycle fuel economy performance of a fuel cell stack and ultracapacitor hybrid SUV vehicles. In most of these papers, the fuel cell stack is modeled with a static polarization relationship for fixed fuel cell operating parameters.

Several dynamic fuel cell system models exist in the literature. Different levels of dynamic behavior were incorporated into each of the models. The thermal dynamics are considered to be the slowest dynamics in the fuel cell system. Therefore, several publications have included only the temperature dynamic in their models and ignored the other dynamics such as air supply and humidity. Turner et al. [109] and Geyer et al. [51] included the transient effect of fuel cell stack temperature rise in their models. By including only temperature dynamics, the system transient behavior can be clearly

observed during the warm-up period as shown in [20]. Hauer et al. [58] represented the dynamics of the fuel reformer with the dynamics of its temperature rise by using a second-order transfer function with an adjustable time constant. Kim and Kim [66] simplified the system model further by using first-order time delay electrical circuit to represent the fuel reformer and the fuel cell stack voltage. The model is connected to a step-up chopper. A fuzzy controller was designed to improve system performance. A few publications [57, 87, 90] included the dynamics of the air supply system, i.e., considered the dynamics of the air compressor and the manifold filling and their consequences to the fuel cell system model. However, neither modeling details nor simulation results were given in these papers.

From the literature review above, it is obvious that a comprehensive control-oriented model is needed. The field is fast evolving and there is a lot of excitement but also a lot of commercial or confidentiality considerations that does not allow state-of-the-art results to be published. The exercise of developing such a model is critical for future control development.

1.5   Thesis Overview

The development of a model of a dynamic fuel cell reactant supply subsystem that is suitable for control study is explained in Chapters 2 and 3. The model incorporates the transient behaviors that are important for integrated control design and analysis. Models of the auxiliary components, namely a compressor, manifolds, an air cooler, and a humidifier, are presented in Chapter 2. Inertia dynamics along with nonlinear curve fitting of the compressor characteristic map are used to model the compressor. The manifold dynamic models are based on lumped-volume filling dynamics. Static models of the air cooler and air humidifier are developed using thermodynamics.

The fuel cell stack model in Chapter 3 is composed of four interacting sub-models, namely stack voltage, cathode flow, anode flow, and membrane hydration models. The stack voltage is calculated as a function of stack current, cell temperature, air pressure, oxygen and hydrogen partial pressures, and membrane humidity. The voltage function presented in Section 3.1 is based on the Nernst open circuit voltage, and activation, ohmic, and concentration losses. Flow equations, mass continuity, and electrochemical relations are used to create lumped-parameter dynamic models of the flow in the cathode and anode in Sections 3.2 and 3.3. Mass transport of water across the fuel cell membrane is calculated in the membrane hydration model in Section 3.4.

A perfect control of air humidifier and a simple proportional control of the hydrogen supply valve are integrated into the model to allow us to focus on the analysis and control design of the air supply system. In Chapter 4, we perform a steady-state analysis of the model in order to determine the optimal value of the air flow setpoint, termed oxygen excess ratio, that results in the maximum system net power. The resulting value agrees with the fuel cell specification in the literature, and thus indirectly validates the accuracy of the model. Results from the simulation of the model with a static feedforward controller based on the optimal setpoint are presented in Section 4.3. The model predicts transient behavior similar to that reported in the literature.

The control design of the air supply system using model-based linear control techniques is presented in Chapter 5. Several control configurations are studied and the advantages and disadvantages of each configuration are also explained. Additionally, the performance limitations of the controller due to measurement constraints are also illustrated. In Section 5.6, the results from an observability analysis suggest the use of stack voltage measurement in the feedback to improve the performance of the observer-based controller. The analogy between the fuel cell closed-loop current-to-voltage transfer function and an electrical impedance, discussed in Section 5.8, can be useful to researchers in the area of power electronics. Section 5.9 presents an analysis of the tradeoff between regulation of cathode oxygen and desired net power during transient. A range of frequencies associated with the tradeoff is determined.

In Chapters 6 and 7, a control problem of the partial oxidation based natural gas fuel processor is studied. The components and processes associated with the processor are explained in Section 6.1. A dynamic model of the processor is also presented in Chapter 6. Transient flow, pressure and

reactor temperature characteristics are included. The reaction products are determined based on the chemical reactions, and the effects of both the oxygen to carbon ratio and the reactor temperature on the conversion are included. The model is validated with a high-order detailed model of the fuel cell and fuel processor system, and the results are shown in Section 6.11.

A two-input two-output control problem of regulating the catalytic partial oxidation (CPOX) temperature and the stack anode hydrogen concentration using natural gas valve and air blower commands is studied in Chapter 7. Section 7.3 illustrates the use of the relative gain array method to find appropriate pairings of the system input and output and also to analyze the system interactions. The analysis shows that large system interactions degrade the performance of the decentralized controller, especially during transient operation. A model-based multivariable controller for the fuel processor system is designed in Section 7.5 using the linear quadratic optimal method. It is shown that significant improvement in CPOX temperature regulation can be achieved with the designed multivariable controller. The controller is then analyzed to determine the important terms that contribute to the improvement of the closed loop performance. This will be useful in the simplification and implementation of the controller.

Chapter 8 provides a summary and contributions of the work. Several topics that need to be addressed and several other interesting areas to study are also given.

1.6 Contributions

Fuel cells are widely regarded as a potential stationary and mobile power source for the future. At present, however, the fuel cell systems are at an early stage of development. Success of fuel cell power generation system will offer tremendous benefits to both consumers and the society. Satisfactory transient behavior of the fuel cell system is one of the key requirements for the success of the fuel cell technology. Many publications have discussed the importance and the need for a well-designed control system for the fuel cell power plant. However, we are not aware of any prior publication presenting a systematic approach in analyzing the dynamic behavior and designing robust controllers for fuel cells. In this thesis, we perform control analysis and design for two fuel cell control problems using model-based control methodologies. Our work provides a comprehensive control analysis of the fuel cell system that not only can be used to develop robust controllers but also can help in making decisions on system re-design for improved performance.

The major contributions of the dissertation include

- Two control problems of the fuel cell power generation system are formulated in this disseration. The first problem is the control of air supply system for a high-pressure direct hydrogen fuel cell system (FCS). The objective is to control the compressor motor command to quickly and efficiently replenish the cathode oxygen depleted during system power generations. The second problem is the control of a low-pressure natural gas fuel processor system (FPS). The goal is to coordinate an air blower and a fuel valve in order to quickly replenish the hydrogen depleted in the fuel cell anode while maintaining the desired temperature of the catalytic partial oxidation (CPOX) reactor.

- Control-oriented dynamic models suitable for control design and analysis are created. The complexity of the models is kept minimal by considering only physical effects relevant to the control problems. The models are developed using physics-based principles allowing them to be used for different fuel cell systems requiring only parameter modifications. Moreover, the variables in the models represent real physical variables providing insight into the dynamic behavior of the real system. The causality of the process is clearly demonstrated in the models.

- The models are used in the model-based control analysis to develop controllers and to determine required control structures that provide an enhanced performance over conventional controllers. Moreover, the analysis provides insight into the performance limitations associated with plant architecture, sensor location and actuator bandwidth.

– For the FCS, the limitations of using integral control and observer-based controller arise from sensor locations. In particular, a direct measurement of the performance variable, i.e. the oxygen excess ratio, is not possible. The compressor flow rate, which is located upstream from the stack, is traditionally used as the only feedback to the controller. Our observability analysis shows that the stack voltage measurement can be used to enhance the closed-loop system performance and robustness. The voltage measurement is currently used only for safety monitoring. However, we demonstrate that the fuel cell stack mean voltage can be used for active control of fuel cell stack starvation. This result exemplifies our contributions in defining critical and cost-effective sensor location for the FCS.

– An additional limitation arises when the FCS architecture dictates that all auxiliary equipments are powered directly from the fuel cell with no secondary power sources. This plant configuration is preferred due to its simplicity, compactness and low cost. We used linear optimal control design to identify the frequencies at which there is severe tradeoff between the transient system net power performance and the stack starvation control. The result can be used to determine the required size of additional energy or oxygen storage devices in the case that fast transient response is required. We demonstrated that the multivariable controller improves the performance of the FCS and results in a different current-voltage dynamic relationship that is captured by the closed-loop FCS impedance. We expect that the derived closed-loop FCS impedance will be very useful and will provide the basis for a systematic design of fuel cell electronic components.

– Multivariable feedback analysis using the control-oriented model of the FPS indicates large system interactions between the fuel and the air loops at high frequencies. Our analysis shows that the magnitude and speed of the fuel valve limit the closed-loop bandwidth in the fuel loop, thus affect hydrogen starvation. We demonstrate that fast regulation of CPOX temperature, which is the objective in the air loop, requires a fast blower and air dynamics if a decentralized control structure is used. On the other hand, a slow blower can also accomplish similar performance if it is coordinated with the fuel valve command. The coordination is achieved with a model-based controller that decouples the two loops at the frequencies of high interaction. With this result we provide rigorous guidelines regarding actuator specifications and the necessary software complexity for multiple actuator coordination.

Chapter 2

Fuel Cell System Model: Auxiliary Components

Models developed specifically for control studies have certain characteristics. Important characteristics such as dynamic (transient) effects are included while some other effects, such as spatial variation of parameters, are lumped and included in ordinary differential or difference equation forms. Furthermore, only dynamic effects that are related to automobile operations are integrated into the models. The relevant time constant for an automotive propulsion-sized PEM fuel cell system are summarized in [57]

- Electrochemistry $O(10^{-19}$ sec$)$

- Hydrogen & air manifolds $O(10^{-1}$ sec$)$

- Membrane water content O(unclear)

- Flow control/supercharging devices $O(10^0$ sec$)$

- Vehicle inertia dynamics $O(10^1$ sec$)$

- Cell and stack temperature $O(10^2$ sec$)$

where O stands for the order of magnitude. The extremely fast transient phenomena of both electrochemical reactions and electrode electrical dynamics have minimal effects in automobile application and can be ignored. The transient behaviors due to manifold filling dynamics, membrane water content, supercharging devices, and temperature may impact the behavior of the vehicle, and thus, must be included in the model. Interactions between processes, when appropriate, are also included. However, with relatively slow responses, the cell and stack temperature may be viewed as a separate control system which is equipped with a separate controller. The temperature can then be considered as a constant for other faster subsystems.

The system block diagram showing the subsystem blocks along with input/output signals is illustrated in Figure 2.1. In this chapter, the models of several components shown in the figure are explained. In this study, we focus on the reactant supply subsystem and thus the models of the components related to this subsystem are developed. The component models for the heat management subsystem are left for future study. Figure 2.2 illustrates the components and flows related to the reactant supply subsystem. In this chapter, the modeling of the auxiliary components is explained. The compressor dynamic model is explained in Section 2.1 followed by an explanation of the manifold filling model in Section 2.2. Static models of the air cooler and the air humidifier are explained in Sections 2.4 and 2.5. In the next chapter, the development of the fuel cell stack model, which consists of stack voltage, anode flow, cathode flow and membrane hydration models, is presented.
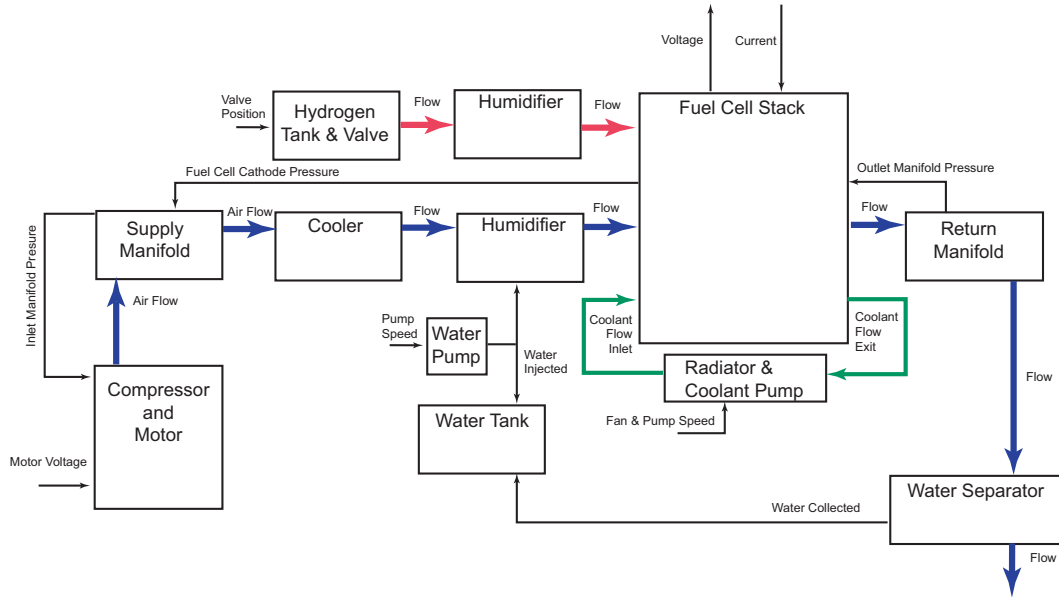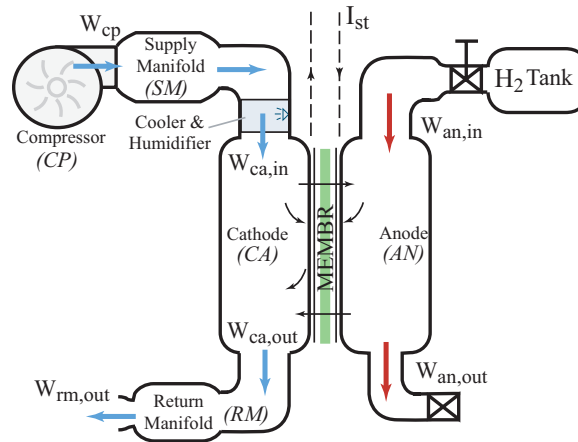
Figure 2.1: System block diagram

Figure 2.2: Reactant supply subsystem model

2.1   Compressor Model

The compressor model is separated into two parts, as shown in Figure 2.3. The first part is a static compressor map which determines the air flow rate through the compressor. Thermodynamic equations are then used to calculate the exit air temperature and the required compressor power. The second part represents the compressor and motor inertia and defines the compressor speed. The speed is consequently used in the compressor map to find the air mass flow rate.
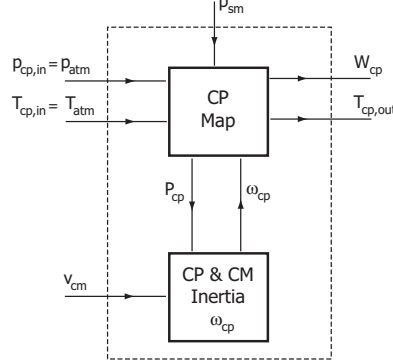

Figure 2.3: Compressor block diagram

The only dynamic state in the model is the compressor speed, ω_{cp}. The inputs to the model include inlet air pressure, $p_{cp,in}$, its temperature, $T_{cp,in}$, voltage command to compressor motor, v_{cm}, and downstream pressure, which is the supply manifold pressure, $p_{cp,out} = p_{sm}$. The inlet air is typically atmospheric and its pressure and temperature are assumed to be fixed at $p_{atm} = 1$ atm and $T_{atm} = 25°C$, respectively. The motor command is one of the inputs to the fuel cell system. The downstream pressure is determined by the supply manifold model.

The compressor air mass flow rate, W_{cp} (kg/sec), is determined, through a compressor flow map, from the pressure ratio across the compressor and the speed of the compressor. However, supplying the compressor flow map in the form of a lookup table is not well-suited for dynamic system simulations [79]. Standard interpolation routines are not continuously differentiable and extrapolation is unreliable. Therefore, a nonlinear curve fitting method is used to model the compressor characteristics. The Jensen & Kristensen method, described in [79], is used in our model.

To reflect variations in the inlet condition of the compressor, which are the inlet flow pressure and temperature, the "corrected" values of mass flow rate and compressor speed are used in the compressor map. The corrected values [30] are the corrected compressor speed (rpm), $N_{cr} = N_{cp}/\sqrt{\theta}$, and the corrected mass flow, $W_{cr} = W_{cp}\sqrt{\theta}/\delta$, where corrected temperature $\theta = T_{cp,in}/\,288\,\mathrm{K}$ and corrected pressure $\delta = p_{cp,in}/1$ atm. Using the Jensen & Kristensen method, the dimensionless head parameter Ψ is first defined:

$$\Psi = \frac{C_p T_{cp,in}\left[\left(\dfrac{p_{cp,out}}{p_{cp,in}}\right)^{\frac{\gamma-1}{\gamma}} - 1\right]}{\frac{1}{2}U_c^2} \tag{2.1}$$

where the inlet air temperature, $T_{cp,in}$, is in Kelvin and U_c is the compressor blade tip speed (m/s)

$$U_c = \frac{\pi}{60}d_c N_{cr} \tag{2.2}$$

d_c is the compressor diameter (m) and γ is the ratio of the specific heats of the gas at constant pressure, C_p/C_v, which is equal to 1.4 in the case of air. The normalized compressor flow rate, Φ, is defined by

$$\Phi = \frac{W_{cr}}{\rho_a \frac{\pi}{4}d_c^2 U_c} \tag{2.3}$$

where ρ_a is air density (kg/m^3). The normalized compressor flow rate, Φ, is then correlated with the head parameter, Ψ, by the equation

$$\Phi = \Phi_{max}\left(1 - \exp^{\beta\left(\frac{\Psi}{\Psi_{max}} - 1\right)}\right) \tag{2.4}$$

where Φ_{max}, β, and Ψ_{max} are polynomial functions of the Mach number, M,

$$\begin{aligned}
\Phi_{max} &= a_4 M^4 + a_3 M^3 + a_2 M^2 + a_1 M + a_0 \\
\beta &= b_2 M^2 + b_1 M + b_0 \\
\Psi_{max} &= c_5 M^5 + c_4 M^4 + c_3 M^3 + c_2 M^2 + c_1 M + c_0
\end{aligned} \tag{2.5}$$

The inlet Mach number, M, is defined by

$$M = \frac{U_c}{\sqrt{\gamma R_a T_{cp,in}}} \tag{2.6}$$

where R_a is the air gas constant. In Equation (2.5), a_i, b_i, and c_i are regression coefficients obtained by curve fitting of the compressor data. The air mass flow in kg/sec is then calculated using Equation (2.3):

$$W_{cr} = \Phi \rho_a \frac{\pi}{4} d_c^2 U_c \tag{2.7}$$

The parameters used in the model are given in Table 2.1. The compressor model used here is for an

Table 2.1: Compressor map parameters

Parameter	Value	Units
R_a	2.869×10^2	J/(kg·K)
ρ_a	1.23	kg/m^3
d_c	0.2286	m

Allied Signal compressor. The data were obtained by digitizing the compressor map given in [30]. The regression coefficients obtained by curve fitting are given in Table 2.2. Figure 2.4 shows that the curve fitting scheme represents the compressor data very well.

Table 2.2: Compressor map regression coefficients

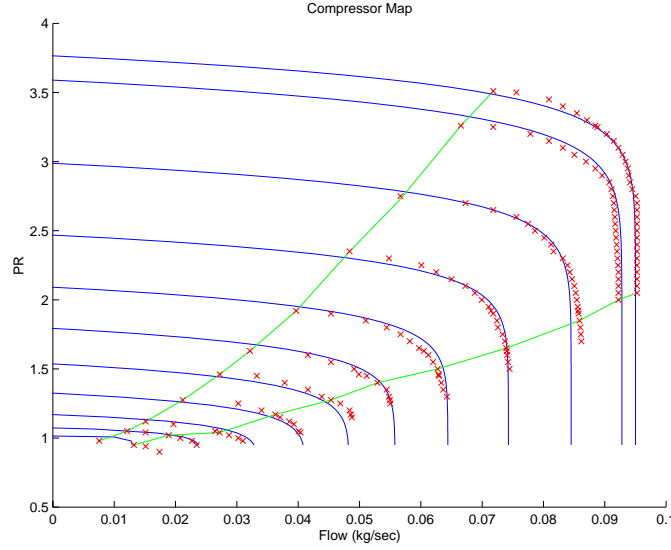| Parameter	Value
a_4	-3.69906×10^{-5}
a_3	2.70399×10^{-4}
a_2	-5.36235×10^{-4}
a_1	-4.63685×10^{-5}
a_0	2.21195×10^{-3}
b_2	1.76567
b_1	-1.34837
b_0	2.44419
c_5	-9.78755×10^{-3}
c_4	0.10581
c_3	-0.42937
c_2	0.80121
c_1	-0.68344
c_0	0.43331

Figure 2.4: Compressor map

A lookup table of the compressor efficiency, η_{cp}, is used to find the efficiency of the compressor from the mass flow rate and pressure ratio across the compressor. The maximum efficiency of the compressor is 80%. The temperature of the air leaving the compressor is calculated from the equation

$$T_{cp,out} = T_{cp,in} + \frac{T_{cp,in}}{\eta_{cp}} \left[\left(\frac{p_{cp,out}}{p_{cp,in}} \right)^{\frac{\gamma-1}{\gamma}} - 1 \right] = T_{atm} + \frac{T_{atm}}{\eta_{cp}} \left[\left(\frac{p_{sm}}{p_{atm}} \right)^{\frac{\gamma-1}{\gamma}} - 1 \right] \tag{2.8}$$

The torque required to drive the compressor is calculated using thermodynamic equations:

$$\tau_{cp} = \frac{C_p}{\omega_{cp}} \frac{T_{atm}}{\eta_{cp}} \left[\left(\frac{p_{sm}}{p_{atm}} \right)^{\frac{\gamma-1}{\gamma}} - 1 \right] W_{cp} \tag{2.9}$$

where τ_{cp} is the torque needed to drive the compressor in N-m
C_p is the specific heat capacity of air $= 1004 \quad$ J·kg^{-1}·K^{-1}
γ is the ratio of the specific heats of air $= 1.4$

Derivations of Equations (2.8) and (2.9) are standard and can be found in the thermodynamics or turbine literature [21, 53].

A lumped rotational parameter model with inertia is used to represent the dynamic behavior of the compressor speed:

$$J_{cp} \frac{d\omega_{cp}}{dt} = (\tau_{cm} - \tau_{cp}) \tag{2.10}$$

where J_{cp} is the combined inertia of the compressor and the motor (kg·m^2)
ω_{cp} is the compressor speed (rad/sec)
τ_{cm} is the compressor motor torque input (N-m)
τ_{cp} is the torque required to drive the compressor (N-m) calculated in (2.9)

The compressor motor torque is calculated using a static motor equation:

$$\tau_{cm} = \eta_{cm} \frac{k_t}{R_{cm}} (v_{cm} - k_v \omega_{cp}) \tag{2.11}$$

where k_t, R_{cm}, and k_v are motor constants and η_{cm} is the motor mechanical efficiency. The values are given in Table 2.3.

Table 2.3: Compressor motor parameters

Parameter	Value
k_v	0.0153 V/(rad/sec)
k_t	0.0153 N-m/Amp
R_{cm}	0.82 Ω
η_{cm}	98%

2.2   Lumped Model of the Manifold Dynamics

The manifold model represents the lumped volume associated with pipes and connections between each device. The supply manifold volume includes the volume of the pipes between the compressor and the fuel cell stack including the volume of the cooler and the humidifier (Figure 1.5). The return manifold represents the pipeline at the fuel cell stack exhaust.
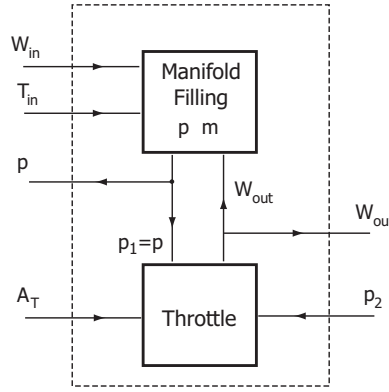

Figure 2.5: Manifold block diagram

Block diagram of the manifold model is shown in Figure 2.5. The mass conservation principle is used to develop the manifold model. For any manifold,

$$\frac{dm}{dt} = W_{in} - W_{out} \tag{2.12}$$

where m is the mass of the gas accumulated in the manifold volume and W_{in} and W_{out} are mass flow rates into and out of the manifold. If we assume that the air temperature is constant in the manifold, T, and equal to the inlet flow temperature, $T = T_{in}$, the manifold filling dynamics follow an isothermic relation:

$$\frac{dp}{dt} = \frac{R_a T}{V}(W_{in} - W_{out}) \tag{2.13}$$

where R_a is the gas constant of air and V is the manifold volume. If the air temperature is expected to change in the manifold, the pressure dynamic equation, which is derived from the energy conservation and the ideal gas law,

$$\frac{dp}{dt} = \frac{\gamma R_a}{V}(W_{in}T_{in} - W_{out}T) \tag{2.14}$$

is used in addition to the mass balance equation (2.12). The air temperature, T, in (2.14), is calculated from m in (2.12) and p in (2.14) using the ideal gas law. In summary, if the temperature of the air in the manifold is assumed constant, Equation (2.13) is used to model the manifold dynamics. If the temperature of the air is expected to change, Equations (2.12) and (2.14) are used.

The nozzle flow equation, derived in [59], is used to calculate the outlet flow of the manifold. The rate of flow through a nozzle is a function of the upstream pressure, p_1, and the downstream pressure,

p_2, of the nozzle. The flow characteristic is divided into two regions by the critical pressure ratio:

$$\left(\frac{p_2}{p_1}\right)_{crit} = \left(\frac{2}{\gamma+1}\right)^{\frac{\gamma}{\gamma-1}} \tag{2.15}$$

where γ is the ratio of the specific heat capacities of the gas, C_p/C_v. In the case of air, $\gamma = 1.4$ and the critical pressure ratio is equal to 0.528. For sub-critical flow where the pressure drop is less than the critical pressure ratio, $\frac{p_2}{p_1} > \left(\frac{2}{\gamma+1}\right)^{\frac{\gamma}{\gamma-1}}$, the mass flow rate is calculated from

$$W = \frac{C_D A_T p_1}{\sqrt{\bar{R} T_1}} \left(\frac{p_2}{p_1}\right)^{\frac{1}{\gamma}} \left\{ \frac{2\gamma}{\gamma-1} \left[1 - \left(\frac{p_2}{p_1}\right)^{\frac{\gamma-1}{\gamma}} \right] \right\}^{\frac{1}{2}} \quad \text{for} \quad \frac{p_2}{p_1} > \left(\frac{2}{\gamma+1}\right)^{\frac{\gamma}{\gamma-1}} \tag{2.16}$$

Parameter C_D is the discharge coefficient of the nozzle, A_T is the opening area of the nozzle (m^2), and $\bar{R}$ is the universal gas constant. For critical flow (or choked flow), the mass flow rate is given by

$$W_{choked} = \frac{C_D A_T p_1}{\sqrt{\bar{R} T_1}} \gamma^{\frac{1}{2}} \left(\frac{2}{\gamma+1}\right)^{\frac{\gamma+1}{2(\gamma-1)}} \quad \text{for} \quad \frac{p_2}{p_1} \leq \left(\frac{2}{\gamma+1}\right)^{\frac{\gamma}{\gamma-1}} \tag{2.17}$$

The plot of W/W_{choked} is shown as a dashed line in Figure 2.6. If the pressure difference between the
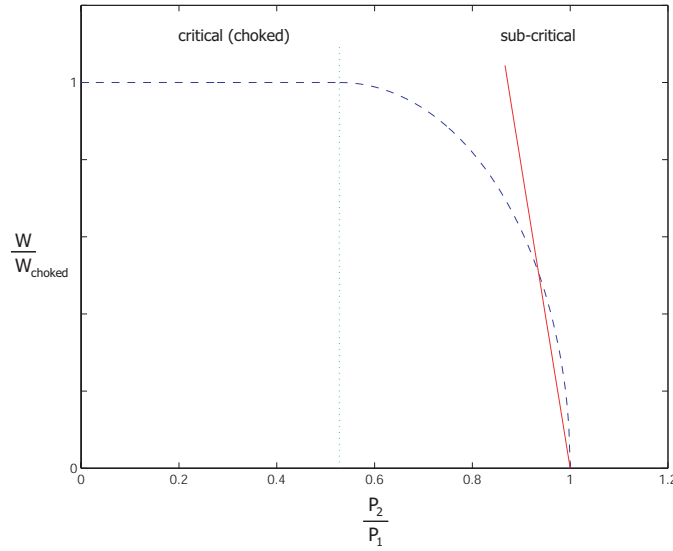
Figure 2.6: Dashed line - relative mass flow rate as a function of nozzle pressure ratio eqns. (2.16)-(2.17), Solid line - linearized mass flow rate at low pressure difference eqn (2.18)

manifold and the downstream volume is small and always falls into the sub-critical flow region, the flow rate can be calculated by a linearized form of the sub-critical nozzle flow equation (2.16)

$$W = k(p_1 - p_2) \tag{2.18}$$

where k is the nozzle constant. The plot of the linearized equation (2.18) for various manifold pressures is shown in Figure 2.7 as a solid line, compared to the plot of Equation (2.16) shown as a dashed line.

2.2.1 Supply Manifold

For the supply manifold, the inlet mass flow is the compressor flow, W_{cp}, and the outlet mass flow is $W_{sm,out}$. Since the pressure difference between the supply manifold and the cathode is relatively

small,

$$W_{sm,out} = k_{sm,out}(p_{sm} - p_{ca}) \tag{2.19}$$

where $k_{sm,out}$ is the supply manifold outlet flow constant. Since the temperature of the air in the supply manifold is high, it is expected that the air temperature changes inside the manifold. Thus, Equations (2.12) and (2.14) are used to model the supply manifold

$$\frac{dm_{sm}}{dt} = W_{cp} - W_{sm,out} \tag{2.20}$$

$$\frac{dp_{sm}}{dt} = \frac{\gamma R_a}{V_{sm}} \left(W_{cp} T_{cp,out} - W_{sm,out} T_{sm} \right) \tag{2.21}$$

where V_{sm} is the supply manifold volume and T_{sm} is the supply manifold air temperature, which is calculated from m_{sm} and p_{sm} using the ideal gas law. Block diagram of the supply manifold is shown
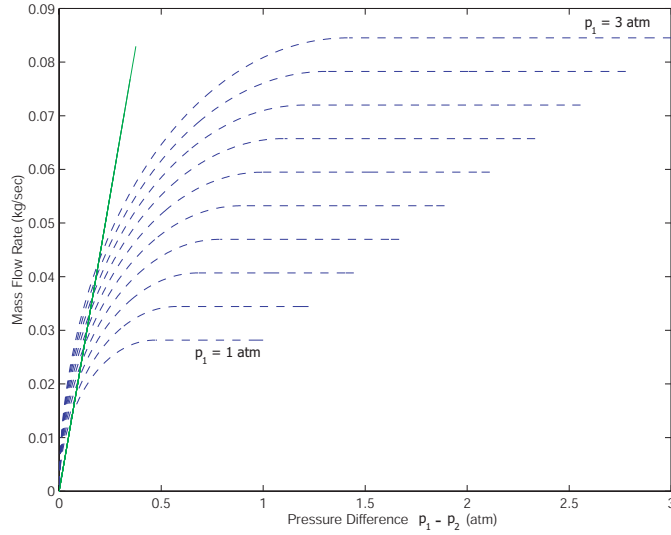

Figure 2.7: Comparison of nozzle flow rate from nonlinear and linear nozzle equations
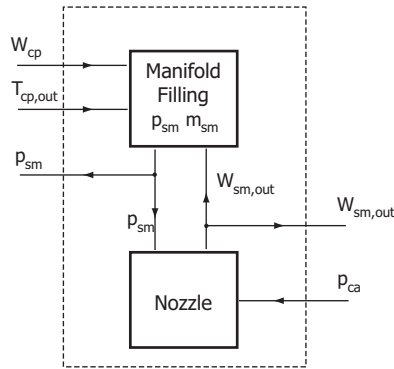
in Figure 2.8.

Figure 2.8: Supply manifold block diagram

2.2.2 Return Manifold

The temperature of the air leaving the stack is relatively low when compared to the air leaving the compressor. Therefore, the changes of air temperature in the return manifold are negligible, and the return manifold pressure is modeled by

$$\frac{dp_{rm}}{dt} = \frac{R_a T_{rm}}{V_{rm}}(W_{ca,out} - W_{rm,out}) \tag{2.22}$$

where V_{rm} is the return manifold volume and T_{rm} is the temperature of the gas in the return manifold. The flow entering the return manifold, $W_{ca,out}$, is calculated in Equation (3.47), which is in the same form as Equation (2.19). The outlet mass flow of the return manifold is governed by nozzle (throttle) equations (2.16)-(2.17). The outlet mass flow is a function of the manifold pressure, p_{rm}, and the pressure downstream from the manifold, which is assumed to be fixed at p_{atm}. Since the pressure drop between the return manifold and the atmospheric is relatively large, the equations of return manifold exit flow are

$$W_{rm,out} = \frac{C_{D,rm}A_{T,rm}p_{rm}}{\sqrt{\bar{R}T_{rm}}}\left(\frac{p_{atm}}{p_{rm}}\right)^{\frac{1}{\gamma}}\left\{\frac{2\gamma}{\gamma-1}\left[1-\left(\frac{p_{atm}}{p_{rm}}\right)^{\frac{\gamma-1}{\gamma}}\right]\right\}^{\frac{1}{2}} \quad \text{for} \quad \frac{p_{atm}}{p_{rm}} > \left(\frac{2}{\gamma+1}\right)^{\frac{\gamma}{\gamma-1}} \tag{2.23}$$

and

$$W_{rm,out} = \frac{C_{D,rm}A_{T,rm}p_{rm}}{\sqrt{\bar{R}T_{rm}}}\gamma^{\frac{1}{2}}\left(\frac{2}{\gamma+1}\right)^{\frac{\gamma+1}{2(\gamma-1)}} \quad \text{for} \quad \frac{p_{atm}}{p_{rm}} \leq \left(\frac{2}{\gamma+1}\right)^{\frac{\gamma}{\gamma-1}} \tag{2.24}$$

The throttle opening area, $A_{T,rm}$, can be set constant or can be used as an extra control variable to regulate the return manifold pressure, and thus the cathode pressure. The values of $C_{D,rm}$ and the nominal value of $A_{T,rm}$ used in the model are given in Table 4.1. Block diagram of the return manifold model is shown in Figure 2.9.
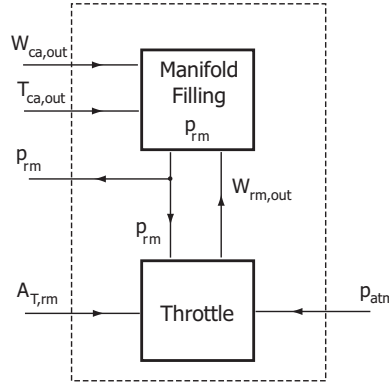
Figure 2.9: Return manifold block diagram

The pressure calculated in the supply manifold model is used in the compressor model to determine the pressure ratio across the compressor. The return manifold pressure calculated in the return manifold model is used to determine the flow rate exiting the fuel cell cathode. The model of the cathode along with other parts of the fuel cell stack will be described in the next chapter.

2.3 Review of the Thermodynamics of Gas Mixtures

In this subsection, we review the basic thermodynamic properties of gas mixtures that we use extensively in the model. Details can be found in [98]. We also focus on the mixture involving gases and water vapor.

Here, we consider properties of ideal gases. Specifically, each component of the mixture is independent of the presence of other components and each component can be treated as an ideal gas. Consider the mixture of gas A and gas B. From the ideal gas law, we have

$$pV = n\bar{R}T = mRT \tag{2.25}$$

where p is the gas pressure, V is the gas volume, n is the number of moles of the gas, m is the mass of the gas, $\bar{R}$ is the universal gas constant, R is the gas constant, and T is the gas temperature. The total number of moles of the mixture is equal to the sum of the number of moles of each component:

$$n = n_A + n_B. \tag{2.26}$$

If we treat each component as an ideal gas, the law in Equation (2.25) holds for each component:

$$\begin{aligned} p_A V &= n_A \bar{R}T \\ p_B V &= n_B \bar{R}T \end{aligned} \tag{2.27}$$

where p_A and p_B are the partial pressures. By substitution of Equations (2.25) and (2.27) into Equation (2.26), we get

$$p = p_A + p_B \tag{2.28}$$

Thus, for a mixture of ideal gases, the pressure of the mixture is the sum of the partial pressures of the individual components.

Let us now consider a mixture of air and water vapor. The humidity ratio, ω, is defined as the ratio of the mass of water vapor, m_v, to the mass of dry air, m_a:

$$\omega = \frac{m_v}{m_a} \tag{2.29}$$

The total mass of the mixture is $m_a + m_v$. The humidity ratio does not give a good representation of the humidity of the mixture since the maximum amount of water vapor that the air can hold (saturation) depends on the temperature and pressure of the air. The relative humidity, which represents the amount of water in the air relative to the maximum possible amount, is therefore more widely used. The relative humidity, ϕ, is defined as the ratio of the mole fraction of the water vapor in the mixture to the mole fraction of vapor in a saturated mixture at the same temperature and pressure. With the assumption of ideal gases, the definition reduces to the ratio of the partial pressure of the water vapor, p_v, in the mixture to the saturation pressure of the vapor at the temperature of the mixture, p_{sat}:

$$\phi = \frac{p_v}{p_{sat}} \tag{2.30}$$

The saturation pressure, p_{sat}, depends on the temperature and is easily obtained from a thermodynamic table of vapor [98]. In the model, the saturation pressure is calculated from an equation of the form given in [82]. The saturation pressure data in [98] is used to obtain the coefficients in the equation:

$$\log_{10}(p_{sat}) = -1.69 \times 10^{-10} T^4 + 3.85 \times 10^{-7} T^3 - 3.39 \times 10^{-4} T^2 + 0.143\, T - 20.92 \tag{2.31}$$

where the saturation pressure, p_{sat}, is in kPa and the temperature, T, is in Kelvin.

The relation between the humidity ratio and the relative humidity can be derived from the ideal gas law:

$$\omega = \frac{m_v}{m_a} = \frac{p_v V / R_v T}{p_a V / R_a T} = \frac{R_a p_v}{R_v p_a} = \frac{M_v}{M_a} \frac{p_v}{p_a} \tag{2.32}$$

where M_v and M_a, both in kg/mol, are the molar mass of vapor and dry air, respectively. By using Equations (2.28) and (2.30), the relative humidity can be calculated from dry air pressure and humidity ratio

$$\phi = \omega \frac{M_a}{M_v} \frac{p_a}{p_{sat}} \tag{2.33}$$

There are two issues that should be pointed out. First, relative humidity having a value of one means that the mixture is saturated or fully humidified. If there is more water content in the mixture, the extra amount of water will condense into a liquid form. Second, with the ideal gas assumption, various components in the mixture can be treated separately when performing the internal energy and enthalpy calculations.

2.4 Air Cooler (Static) Model

The temperature of the air in the supply manifold is typically high due to the high temperature of air leaving the compressor. To prevent any damage to the fuel cell membrane, the air needs to be cooled down to the stack operating temperature. In this study, we do not address heat transfer effects and thus we assume that an ideal air cooler maintains the temperature of the air entering the stack at $T_{cl} = 80°C$. It is assumed that there is no pressure drop in the cooler, $p_{cl} = p_{sm}$. Since temperature change effects gas humidity, the humidity of the gas exiting the cooler is calculated

$$\phi_{cl} = \frac{p_{v,cl}}{p_{sat}(T_{cl})} = \frac{p_{cl}p_{v,atm}}{p_{atm}p_{sat}(T_{cl})} = \frac{p_{cl}\phi_{atm}p_{sat}(T_{atm})}{p_{atm}p_{sat}(T_{cl})} \tag{2.34}$$

where $\phi_{atm} = 0.5$ is the average ambient air relative humidity and $p_{sat}(T_i)$ is the vapor saturation pressure that is a function of temperature, T_i.

2.5 Humidifier (Static) Model

Air flow from the cooler is humidified before entering the stack by injecting water into the air stream in the humidifier. Here, the volume of the humidifier is small and hence it can be considered as part of the supply manifold volume. A static model of the humidifier is used to calculate the change in air humidity due to the additional injected water. The temperature of the flow is assumed to be constant, thus, $T_{hm} = T_{cl}$. The water injected is assumed to be in the form of vapor or the latent heat of vaporization is assumed to be taken into account in the air cooler. Based on the condition of the flow exiting the cooler ($W_{cl} = W_{sm,out}$, p_{cl}, T_{cl}, ϕ_{cl}), the dry air mass flow rate, $W_{a,cl}$, the vapor mass flow rate, $W_{v,cl}$, and the dry air pressure, $p_{a,cl}$, can be calculated using the thermodynamic properties discussed in Section 2.3. The vapor saturation pressure is calculated from the flow temperature using Equation 2.31. Then, the vapor pressure is determined using Equation (2.30):

$$p_{v,cl} = \phi_{cl}p_{sat}(T_{cl}) \tag{2.35}$$

Since humid air is a mixture of dry air and vapor, dry air partial pressure is the difference between the total pressure and the vapor pressure:

$$p_{a,cl} = p_{cl} - p_{v,cl} \tag{2.36}$$

The humidity ratio can then be calculated from

$$\omega_{cl} = \frac{M_v}{M_a}\frac{p_{v,cl}}{p_{a,cl}} \tag{2.37}$$

where M_a is the molar mass of dry air (28.84×10^{-3} kg/mol). The mass flow rate of dry air and vapor from the cooler is

$$W_{a,cl} = \frac{1}{(1 + \omega_{cl})}W_{cl} \tag{2.38}$$

$$W_{v,cl} = W_{cl} - W_{a,cl} \tag{2.39}$$

The mass flow rate of dry air remains the same for inlet and outlet of the humidifier, $W_{a,hm} = W_{a,cl}$. The vapor flow rate increases by the amount of water injected is

$$W_{v,hm} = W_{v,cl} + W_{v,inj} \tag{2.40}$$

The vapor pressure also changes and can be calculated using Equation (2.32):

$$p_{v,hm} = \omega_{cl} \frac{M_a}{M_v} p_{a,cl} = \frac{W_{v,hm}}{W_{a,cl}} \frac{M_a}{M_v} p_{a,cl}. \tag{2.41}$$

The vapor pressure, $p_{v,hm}$, can then be used to determine the exit flow relative humidity

$$\phi_{hm} = \frac{p_{v,hm}}{p_{sat}(T_{hm})} = \frac{p_{v,hm}}{p_{sat}(T_{cl})}. \tag{2.42}$$

Since the vapor pressure increases, the total pressure also increases. Thus,

$$p_{hm} = p_{a,cl} + p_{v,hm} \tag{2.43}$$

The humidifier exit flow rate is governed by the mass continuity

$$W_{hm} = W_{a,cl} + W_{v,hm} = W_{a,cl} + W_{v,cl} + W_{v,inj} \tag{2.44}$$

The flow leaving the humidifier enters the fuel cell cathode and thus in the next chapter, the humidifier exit flow is referred to as cathode inlet (ca, in) flow, for example, $W_{ca,in} = W_{hm}$ and $\phi_{ca,in} = \phi_{hm}$.

The models of auxiliary components in the fuel cell system are developed in this chapter. These models will interact with the fuel cell stack model. In the next chapter, the fuel cell stack model and its sub-models are described.

Chapter 3

Fuel Cell System Model: Fuel Cell Stack

The fuel cell stack model contains four interacting sub-models which are the stack voltage, the anode flow, the cathode flow, and the membrane hydration models. A block diagram of the stack model is shown in Figure 3.1. A stack thermal sub-model can be added in the future when temperature changes are taken into account. In this model, although we calculate the heat generated due to the reaction, the stack temperature is assumed to be constant. In the voltage model, an equation
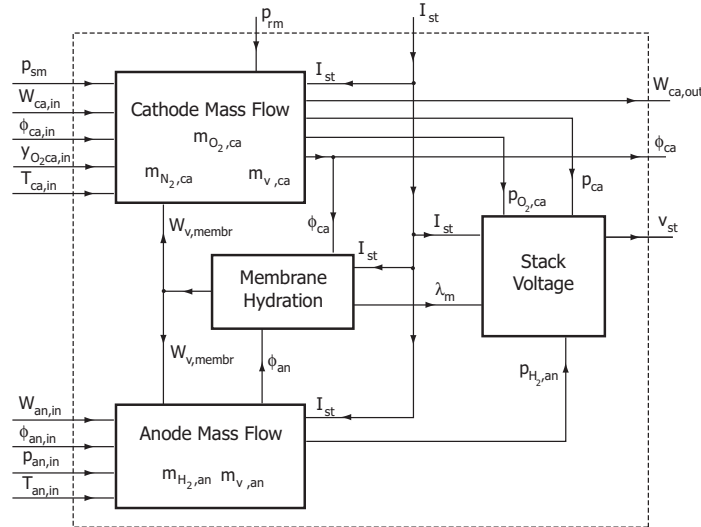
Figure 3.1: Fuel cell stack block diagram

is used to calculate stack voltage for a set of operating conditions: pressure, temperature, reactant gas partial pressure, and membrane humidity. The fast dynamic effect of the electrode RC system is also explained but is not included in the model. The cathode and anode flow models use mass conservation along with thermodynamic properties to calculate the pressure and the relative humidity of the reactant gas flow inside the stack flow channels. The main flows associated with the fuel cell stack are shown in Figure 3.2 where MEA is the membrane electrode assembly that was explained in Chapter 1. The process of water transfer across the membrane is represented by the membrane hydration model.

Figure 3.2: Stack mass flow

3.1 Stack Voltage Model

In this section, the modeling of the fuel cell voltage is discussed. The open circuit voltage of the fuel cell is calculated from the energy balance between chemical energy in the reactants and electrical energy. Three main types of losses in the fuel cell are explained. The dynamic electrical behavior of fuel cell is also briefly discussed.

3.1.1 Fuel Cell Open Circuit Voltage

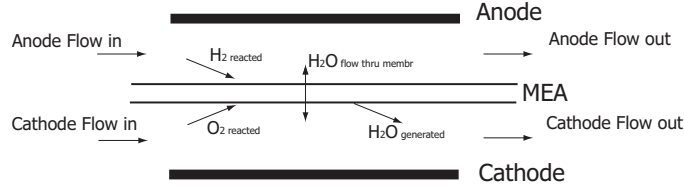The fuel cell directly converts chemical energy into electrical energy. The chemical energy released from the fuel cell can be calculated from the change in Gibbs free energy (Δg_f) which is the difference between the Gibbs free energy of the product and the Gibbs free energy of the reactants. The Gibbs free energy is used to represent the available energy to do external work. For the hydrogen/oxygen fuel cell, the basic chemical reaction is

$$H_2 + \frac{1}{2}O_2 \rightarrow H_2O \tag{3.1}$$

and the change in the Gibbs free energy Δg_f is

$$\Delta g_f = g_f \text{ of products } - g_f \text{ of reactants } = (g_f)_{H_2O} - (g_f)_{H_2} - (g_f)_{O_2} \tag{3.2}$$

The change in Gibbs free energy varies with both temperature and pressure. It can be shown that [69]

$$\Delta g_f = \Delta g_f^0 - \bar{R}T_{fc} \ln \left[\frac{p_{H_2} p_{O_2}^{\frac{1}{2}}}{p_{H_2O}} \right] \tag{3.3}$$

where Δg_f^0 is the change in Gibbs free energy at standard pressure (1 Bar) which varies with the temperature, T_{fc}, of the fuel cell, in Kelvin. The partial pressure, p_{H_2}, p_{O_2}, and p_{H_2O} of the hydrogen, oxygen, and vapor, respectively are expressed in Bar. $\bar{R}$ is the universal gas constant 8.31451 J/(kg·K). The change in Gibbs free energy of the reaction in (3.1) at standard pressure Δg_f^0 is given in Table 3.1 for various reaction temperatures. The value of Δg_f^0 is negative which means that the energy is released from the reaction.

If the fuel cell process were "reversible," all of the Gibbs free energy would be converted to electrical energy, which is the electrical work used to move electrical charge around a circuit. For each mole of hydrogen, two moles of electrons pass around the external circuit and the electrical work done (charge × voltage) is

$$\text{Electrical work done } = -2FE \qquad \text{Joules} \tag{3.4}$$

where F is the Faraday Constant (=96485 Coulombs) which represents the electric charge of one mole of electrons and E is the voltage of the fuel cell. This electrical work done would be equal to the change in Gibbs free energy if the system were considered reversible:

$$\Delta g_f = -2FE \tag{3.5}$$

Table 3.1: Change in Gibbs free energy of hydrogen fuel cell at various temperatures [69]

Form of water product	Temperature $°C$	Δg_f^0 (kJ/mole)
Liquid	25	-237.2
Liquid	80	-228.2
Gas	80	-226.1
Gas	100	-225.2
Gas	200	-220.4
Gas	400	-210.3
Gas	600	-199.6
Gas	800	-188.6
Gas	1000	-177.4

Thus, using Equation (3.3), the reversible voltage of the fuel cell can be written as

$$E = \frac{-\Delta g_f}{2F} = \frac{-\Delta g_f^0}{2F} + \frac{RT_{fc}}{2F} \ln \left[\frac{p_{H_2} p_{O_2}^{\frac{1}{2}}}{p_{H_2O}} \right] \tag{3.6}$$

In practice, the fuel cell process is not reversible, some of the chemical energy is converted to heat, and the fuel cell voltage, V_{fc}, is less than that in Equation (3.6). Voltage E in Equation (3.6) is called the reversible open circuit voltage or "Nernst" voltage of a hydrogen fuel cell. The term $-\Delta g_f^0/2F$ varies from standard state ($25°C$ and 1 atm) reference potential (1.229 V) in accordance with the temperature in the form [4]

$$-\frac{\Delta g_f^0}{2F} = 1.229 + (T_{fc} - T_0) \left(\frac{\Delta S^0}{2F} \right) \tag{3.7}$$

where T_0 is the standard state temperature (298.15 K) and ΔS^0 is the entropy change. Since the variation in specific heat with the expected changes in temperature is minimal, the entropy change of a given reaction is approximately constant and can be set to the standard value [4], thus,

$$-\frac{\Delta g_f^0}{2F} = 1.229 - \frac{298.15 \cdot \Delta S_0^0}{2F} + \left(\frac{\Delta S_0^0}{2F} \right) T_{fc} \tag{3.8}$$

Using thermodynamic values of the standard state entropy change, Equation (3.8) is further expanded and yields [4]

$$E = 1.229 - 0.85 \times 10^{-3}(T_{fc} - 298.15) + 4.3085 \times 10^{-5} T_{fc} \left[\ln(p_{H_2}) + \frac{1}{2} \ln(p_{O_2}) \right] \quad \text{volts} \tag{3.9}$$

In Equation (3.9), T_{fc} is expressed in Kelvin, and p_{H_2} and p_{O_2} are expressed in atm. When the fuel cell operates, the actual voltage of the cell is less than the value calculated by Equation (3.9), as shown in a typical fuel cell performance plot in Figure 3.3. The differences are a result of losses or irreversibilities. In Figure 3.3, cell voltage is the actual voltage of the fuel cell, v_{cell}, and the current density, i, is defined as cell current, which equals stack current I_{st} (A), per cell active area, A_{fc} (cm^2).

$$i = \frac{I_{st}}{A_{fc}} \tag{3.10}$$

The cell current is equal to the stack current, I_{st}, because the stack is formed by connecting the fuel cells in series.

The fuel cell losses are attributed to three categories: the activation loss, the ohmic loss, and the concentration loss. Plots of voltage drops caused by each of the losses are shown in Figure 3.4. Each of these losses is considered and modeled separately in the following sections.
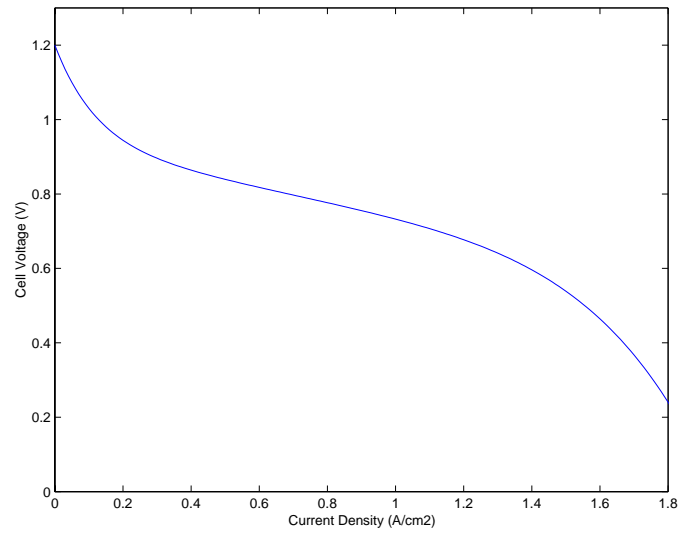
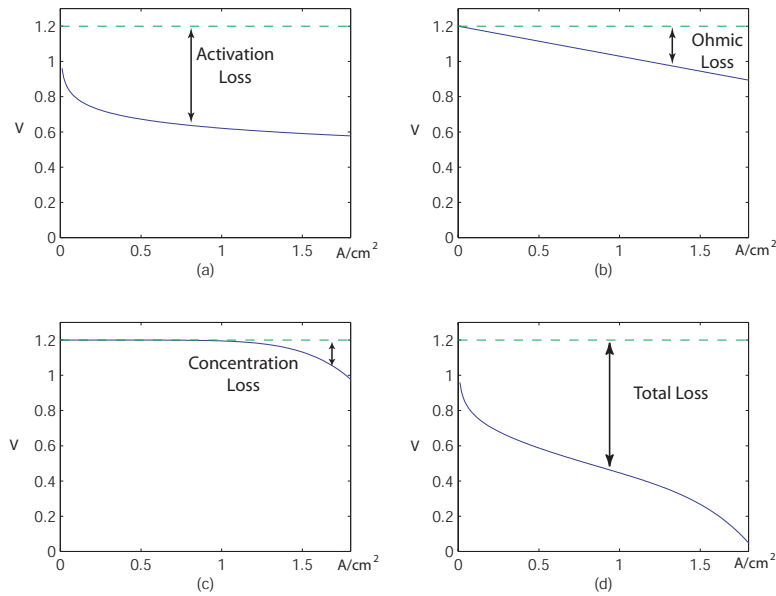Figure 3.3: Typical Fuel Cell Polarization Curve

Figure 3.4: Voltage drops caused by different types of losses in fuel cell: (a) Activation losses only (b) Ohmic losses only (c) Concentration losses only (d) Total losses

3.1.2   Activation Loss

The activation loss or activation overvoltage is a result of the need to cause electron transfer and to break and form chemical bonds in the anode and cathode [73]. Part of the available energy is lost in driving the chemical reaction that transfers the electrons to and from the electrodes [69]. Activation overvoltage occurs at both fuel cell electrodes: anode and cathode. However, the reaction of hydrogen oxidation at the anode is very rapid while the reaction of oxygen reduction at the cathode is considerably slower [8]. Therefore, the voltage drop due to the activation loss is dominated by the cathode reaction conditions. The relation between the activation overvoltage and the current density is described by the Tafel equation [69]

$$v_{act} = a \ln\left(\frac{i}{i_0}\right) \tag{3.11}$$

where a is a constant and i_0, the exchange current density, is also a constant. Both constants can be determined empirically.
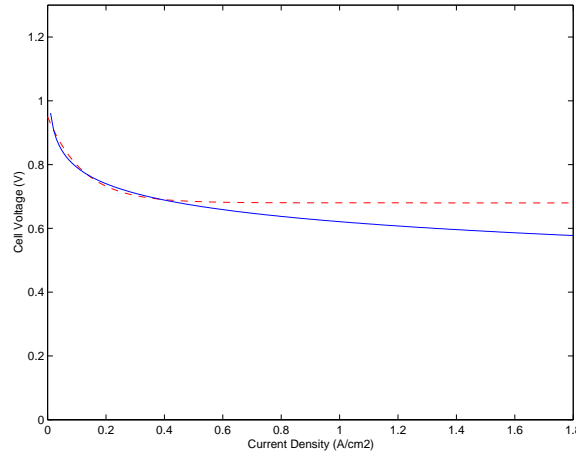

Figure 3.5: Voltage drop caused by activation loss: solid line for (3.11), dashed line for (3.12)

The Tafel equation is however valid only for $i > i_0$. For low temperature PEM fuel cells, the typical value of i_0 is about 0.1 mA/cm^2 [69]. A plot of fuel cell voltage when considering only activation loss is shown as a solid line in Figure 3.5. Since Equation (3.11) is valid only for $i > i_0$, another similar function that is valid for the entire range of i is preferred in the fuel cell simulation. Therefore, the function in Equation (3.11) is approximated by

$$v_{act} = v_0 + v_a(1 - e^{-c_1 i}) \tag{3.12}$$

where v_0 (volts) is the voltage drop at zero current density, and v_a (volts) and c_1 are constants. The activation overvoltage depends strongly on the temperature [67] and the oxygen partial pressure [4]. The values of v_0, v_a, and c_1 and their dependency on oxygen partial pressure and temperature can be determined from a nonlinear regression of experimental data using the basis function in Equation (3.12). The voltage drop calculated using Equation (3.12) is shown as a dashed line in Figure 3.5.

3.1.3   Ohmic Loss

The ohmic loss is due to the resistance of the polymer membrane to the transfer of protons and the resistance of the electrode and the collector plate to the transfer of electrons. The voltage drop that corresponds to the ohmic loss is proportional to the current density

$$v_{ohm} = i \cdot R_{ohm} \tag{3.13}$$

where R_{ohm} is the internal electrical resistance which has units of $\Omega \cdot cm^2$. The resistance depends strongly on the membrane humidity [70] and the cell temperature [5]. Several studies [82, 100] showed that the ohmic resistance is a function of the membrane conductivity $(\Omega \cdot cm)^{-1}$, σ_m, in the form

$$R_{ohm} = \frac{t_m}{\sigma_m} \tag{3.14}$$

where t_m is the thickness of the membrane and the membrane conductivity, σ_m, is a function of membrane water content, λ_m, and fuel cell temperature. The value of λ_m varies between 0 and 14 [100], which is equivalent to the relative humidity of 0% and 100%, respectively. The variation of the membrane conductivity with different membrane humidity and temperature is in the form [100]

$$\sigma_m = b_1 \exp\left(b_2 \left(\frac{1}{303} - \frac{1}{T_{fc}} \right) \right) \tag{3.15}$$

where b_1 is a function of membrane water content, λ_m,

$$b_1 = (b_{11}\lambda_m - b_{12}) \tag{3.16}$$

and b_2 is a constant. Constants b_{11}, b_{12} and b_2 are usually determined empirically. The empirical values of b_{11} and b_{12} for Nafion 117 membrane are given in [100].

3.1.4   Concentration Loss

Concentration loss or concentration overvoltage results from the change in concentration of the reactants as they are consumed in the reaction. These losses are the reason for rapid voltage drop at high current density. An equation that approximates the voltage drop resulting from concentration losses is given by [57]

$$v_{conc} = i\left(c_2 \frac{i}{i_{max}} \right)^{c_3} \tag{3.17}$$

where c_2, c_3, and i_{max} are constants that depend on the temperature and the reactant partial pressure and can be determined empirically. The parameter i_{max} is the current density that causes precipitous voltage drop.

3.1.5   Cell Terminal Voltage

By combining all voltage drops associated with all the losses in the previous sections, the fuel cell operating voltage can be written as

$$\begin{aligned} v_{fc} &= E - v_{act} - v_{ohm} - v_{conc} \\ &= E - \left[v_0 + v_a(1 - e^{-c_1 i}) \right] - [iR_{ohm}] - \left[i\left(c_2 \frac{i}{i_{max}} \right)^{c_3} \right] \end{aligned} \tag{3.18}$$

where the open circuit voltage, E, is given in Equation (3.9). The voltage calculated, v_{fc}, represents the voltage of a single fuel cell. Since individual cells are stacked up in series to form a fuel cell stack, the total voltage of the stack is calculated by multiplying the single cell voltage and the total number of cells, n, in the stack:

$$v_{st} = n \times v_{fc} \tag{3.19}$$

The parameters in the expression (3.18) are determined using nonlinear regression with fuel cell polarization data, plotted in Figure 3.6, which is for an automotive propulsion-sized PEM fuel cell stack. The function 'lsqcurvefit,' which solves nonlinear curve-fitting problems in Matlab optimization toolbox, is used.

The form of R_{ohm} in Equation (3.14) is used in the regression. Since the data plotted in Figure 3.6 is obtained from a fuel cell operated at steady state and at designed operating conditions, it shows
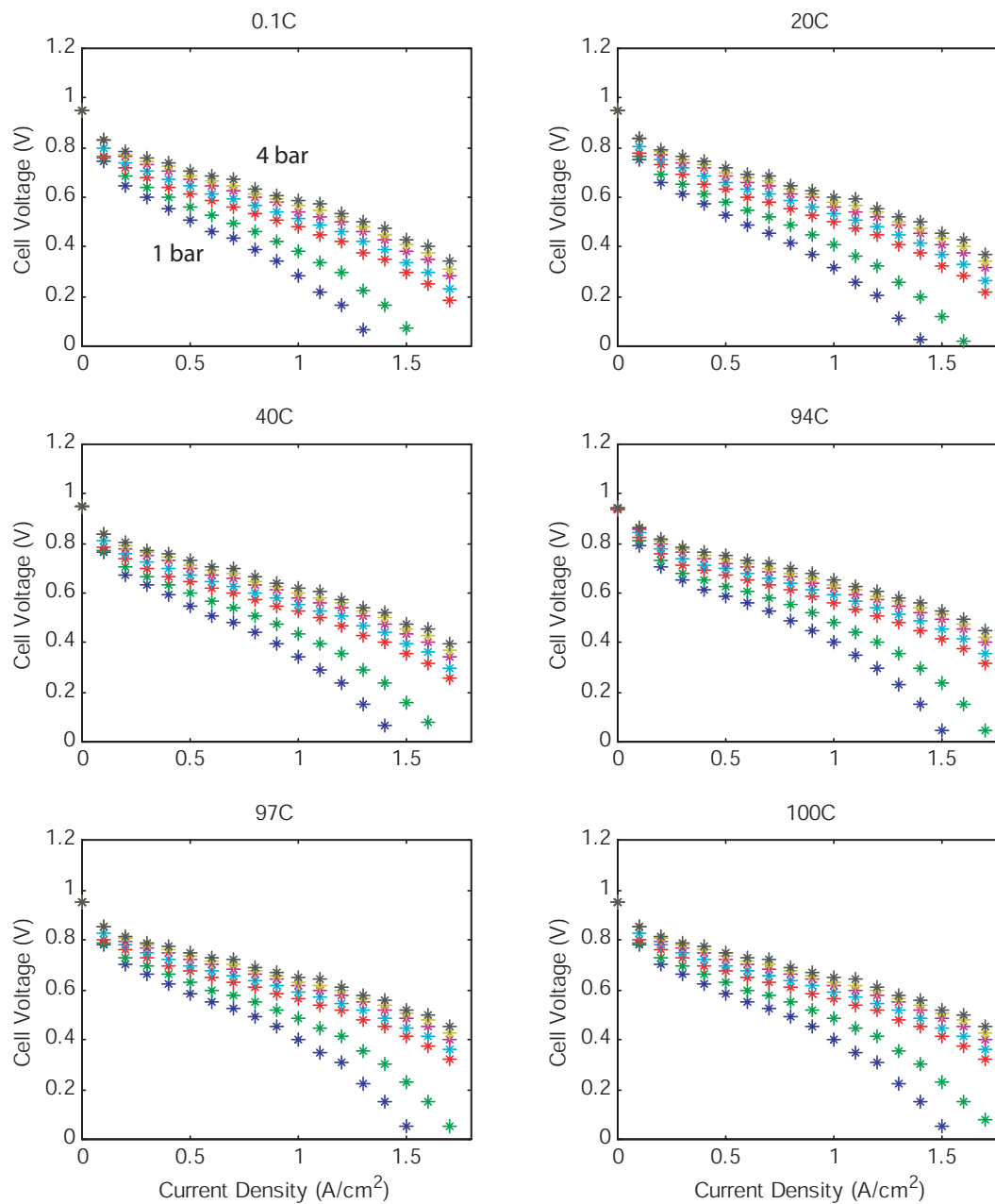
Figure 3.6: Polarization data for temperatures 0.1, 20, 40, 94, 97, 100 Celsius and pressure 1, 1.5, 2, 2.5, 3, 3.5, 4 bar

only the effect of different pressure and temperature on the fuel cell voltage. The effects of reactant partial pressure and membrane humidity are not included. To take into account the fact that the data is obtained when the membrane is fully humidified, the value of b_1 at the maximum membrane humidity is used in Equation (3.15), i.e.

$$b_1 = b_{11}(14) - b_{12} = 0.005139(14) - 0.00326 = 0.068686 \tag{3.20}$$

where $b_{11} = 0.005139$ and $b_{12} = 0.00326$ given in [100] are used. The value of $b_2 = 350$ is, however, modified from the one given in [100] to match the data. First, the function of other parameters in Equation (3.18) with respect to the pressure is determined. The coefficients in the function are then curve fitted with the temperature. By assuming that the data correspond to the ideal operating condition, where the oxygen excess ratio is 2, the pressure terms in the regression of the activation and concentration overvoltage are converted to oxygen partial pressure. This represents the effect of partial pressure on the fuel cell voltage in Equation (3.18). The regression results are

$$E = 1.229 - 8.5 \times 10^{-4}(T_{fc} - 298.15) + 4.308 \times 10^{-5}T_{fc}\left[\ln\frac{p_{H_2}}{1.01325} + \frac{1}{2}\ln\frac{p_{O_2}}{1.01325}\right]$$

$$v_0 = 0.279 - 8.5 \times 10^{-4}(T_{fc} - 298.15)$$
$$+ 4.308 \times 10^{-5}T_{fc}\left[\ln\left(\frac{p_{ca} - p_{sat}}{1.01325}\right) + \frac{1}{2}\ln\left(\frac{0.1173(p_{ca} - p_{sat})}{1.01325}\right)\right]$$

$$v_a = (-1.618 \times 10^{-5}T_{fc} + 1.618 \times 10^{-2})(\frac{p_{O_2}}{0.1173} + p_{sat})^2$$
$$+ (1.8 \times 10^{-4}T_{fc} - 0.166)(\frac{p_{O_2}}{0.1173} + p_{sat}) + (-5.8 \times 10^{-4}T_{fc} + 0.5736)$$

$$c_1 = 10$$
$$t_m = 0.0125$$
$$b_1 = 0.005139\lambda_m - 0.00326$$
$$b_2 = 350$$
$$\sigma_m = b_1 \exp\left(b_2\left(\frac{1}{303} - \frac{1}{T_{fc}}\right)\right)$$
$$R_{ohm} = \frac{t_m}{\sigma_m}$$

$$c_2 = \begin{cases} (7.16 \times 10^{-4}T_{fc} - 0.622)(\frac{p_{O_2}}{0.1173} + p_{sat}) \\ \qquad + (-1.45 \times 10^{-3}T_{fc} + 1.68) \quad \text{for } (\frac{p_{O_2}}{0.1173} + p_{sat}) < 2 \text{ atm} \\ \\ (8.66 \times 10^{-5}T_{fc} - 0.068)(\frac{p_{O_2}}{0.1173} + p_{sat}) \\ \qquad + (-1.6 \times 10^{-4}T_{fc} + 0.54) \quad \text{for } (\frac{p_{O_2}}{0.1173} + p_{sat}) \geq 2 \text{ atm} \end{cases}$$

$$i_{max} = 2.2$$
$$c_3 = 2 \tag{3.21}$$

where T_{fc} (K) is the temperature of the fuel cell, p_{ca} (bar) is the cathode pressure, p_{sat} (bar) is water saturation pressure, which is a function of temperature, and p_{H_2} and p_{O_2} (bar) are the partial pressure of oxygen in the cathode and hydrogen in the anode, respectively. Examples of polarization curves created by these equations are shown in Figure 3.7. The curves of activation, ohmic, and concentration overvoltage at different pressures for $80°C$ are shown in Figures 3.8, 3.9 and 3.10, respectively. The variation of the losses with temperature at the pressure of 2.5 bar are shown in Figures 3.11 - 3.13. An example of the effect of membrane water content on the cell voltage is illustrated in Figure 3.14 which shows the fuel cell polarization curve for membrane water content of 14 (100%) and 7 (50%).
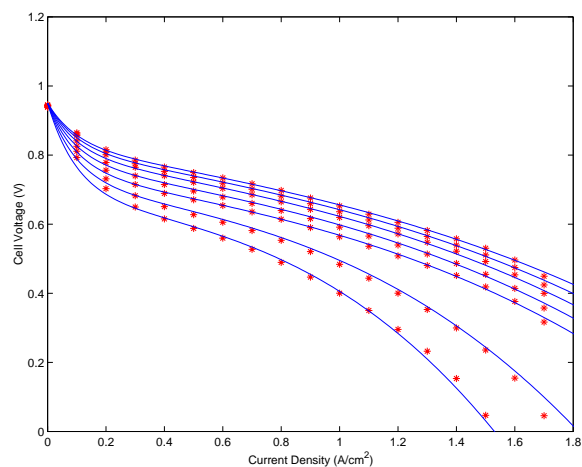
Figure 3.7: Fuel cell polarization curve for $94°C$ and varying pressure from 1 to 4 bar
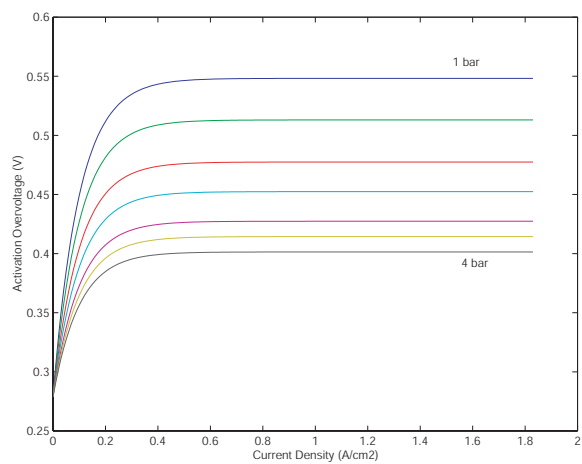
Figure 3.8: Activation overvoltage for $80°C$ and pressures from 1 to 4 bar
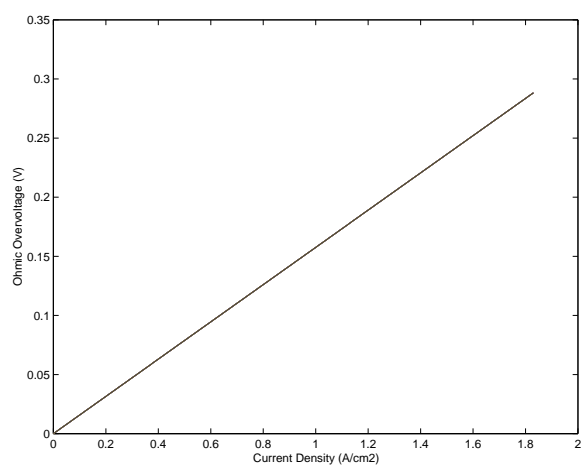
Figure 3.9: Ohmic overvoltage for $80°C$ and pressures from 1 to 4 bar

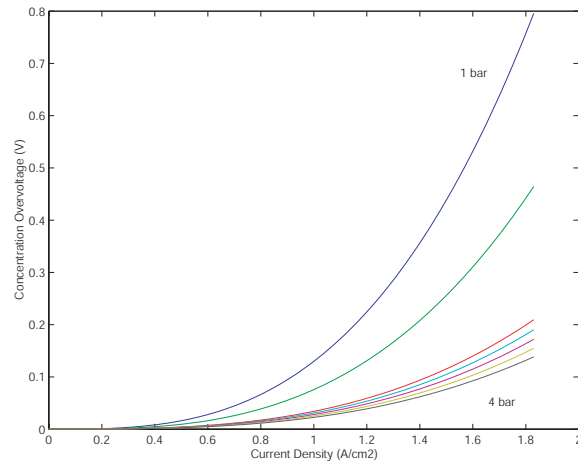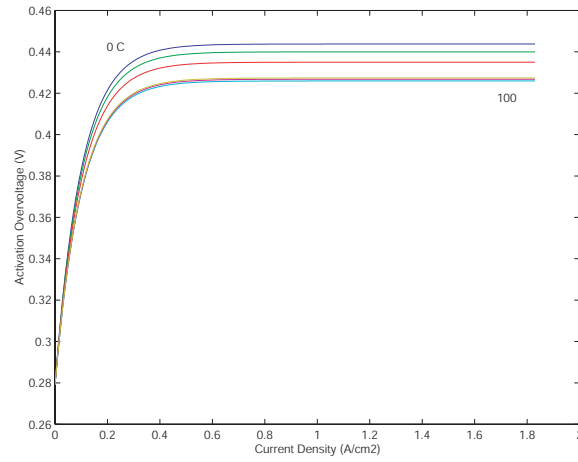Figure 3.10: Concentration overvoltage for $80°C$ and pressures from 1 to 4 bar

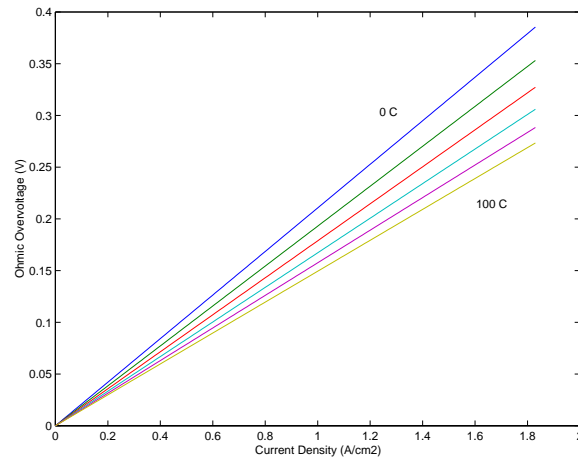Figure 3.11: Activation overvoltage for 2.5 bar and temperatures from 0 to $100°C$

Figure 3.12: Ohmic overvoltage for 2.5 bar and temperature from 0 to $100°C$
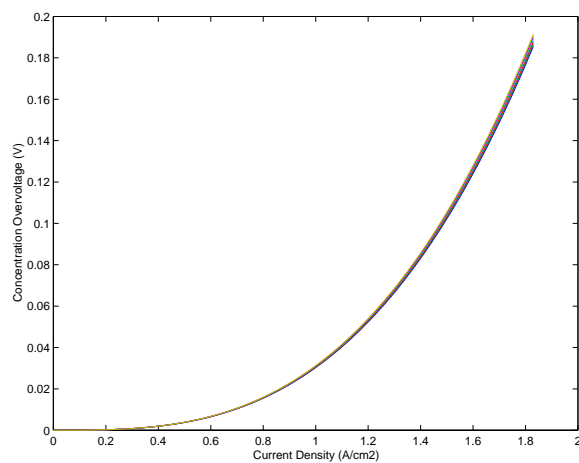
Figure 3.13: Concentration overvoltage for 2.5 bar and temperature from 0 to $100°C$
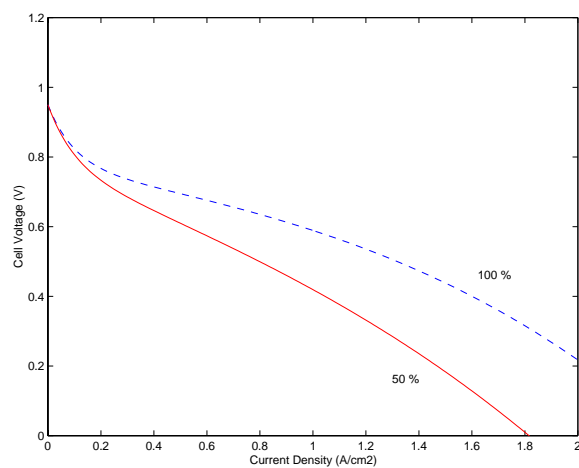
Figure 3.14: Polarization curves for $100°C$ at 2.5 bar and different membrane water content

The calculation of parameters in Equation (3.21) requires the knowledge of cathode pressure (representing total pressure), p_{ca}, oxygen partial pressure, p_{O_2}, and fuel cell temperature, T_{fc} (Figure 3.15). The pressures are calculated from the cathode model discussed in Section 3.2. The temperature can be determined based on the stack heat transfer modeling. For the current study, fixed stack temperature is assumed. The membrane conductivity that is needed in (3.14) is calculated in the membrane hydration model discussed in Section 3.4.
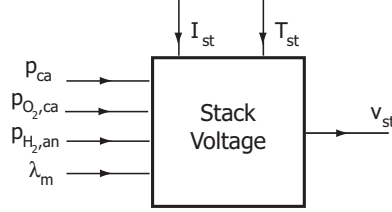
Figure 3.15: Stack voltage model block

3.1.6 Fuel Cell Dynamic Electrical Effect

The fuel cell exhibits a fast dynamic behavior known as "charge double layer" phenomenon. Specifically, near the electrode/electrolyte interface, there is a layer of charge, called "charge double layer," that stores electrical charge and, thus, energy. This layer behaves like an electrical capacitor. The collection of charges generates an electrical voltage which corresponds to the combination of activation overvoltage and concentration overvoltage considered previously [69]. Therefore, when the current suddenly changes, it takes some time before the activation overvoltage and concentration overvoltage follow the change in the current. The ohmic voltage drop, on the other hand, responds instantaneously to a change in the current. Thus, the equivalent circuit in Figure 3.16 can be used to model the dynamic behavior of the fuel cell. Using Equations (3.12) and (3.17), we define activation resistance, R_{act}, and concentration resistance, R_{conc}, as
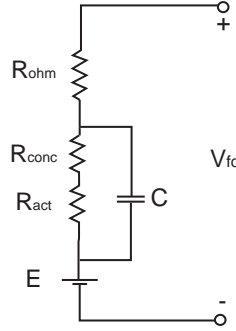
Figure 3.16: Fuel cell equivalent circuits

$$R_{act} = \frac{1}{i}\left[v_0 + v_a(1 - e^{-c_1 i})\right] \tag{3.22a}$$

$$R_{conc} = \left(c_2 \frac{i}{i_{max}}\right)^{c_3} \tag{3.22b}$$

The dynamic fuel cell voltage behavior can be described by

$$C\frac{dv_c}{dt} + \frac{v_c - v_0}{R_{act} + R_{conc}} = i \tag{3.23a}$$

$$v_{fc} = E - v_c - iR_{ohm} \tag{3.23b}$$

The time constant of the fuel cell RC elements is not well established in the literature. The author in [57] reported the time constant of 10^{-19} seconds, which indicates extremely fast dynamics. This value is believed to be for a single fuel cell. The transient response of RC elements of the automobile-sized fuel cell stack can be slower. However, it is expected that the dynamics are still faster than that of the manifolds or other dynamics considered in this study. Therefore, this RC dynamic effect is not included in our model.

3.2   Cathode Flow Model

The cathode mass flow model represents the air flow behavior inside the cathode of the fuel cell stack. The model is developed using the mass conservation principle and thermodynamic and psychometric properties of air. The thermodynamic properties of gas mixtures reviewed in Section 2.3 are used extensively in the model.

Mass continuity is used to balance the mass of three elements, namely oxygen, nitrogen, and water, inside the cathode volume, illustrated in Figure 3.17. The states of the model are oxygen mass, $m_{O_2,ca}$,
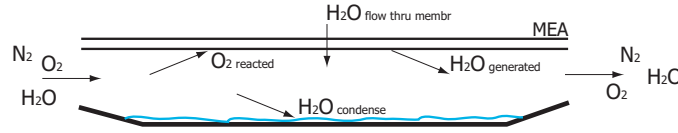

Figure 3.17: Cathode mass flow

nitrogen mass, $m_{N_2,ca}$, and water mass, $m_{w,ca}$. The subscript 'ca' represents the fuel cell cathode. The input to the model consists of stack current, I_{st}, stack temperature, T_{st}, water flow rate across the membrane, $W_{v,membr}$, downstream pressure, which is the return manifold pressure, p_{rm}, and inlet flow properties including inlet flow temperature, $T_{ca,in}$, pressure, $p_{ca,in}$, mass flow rate, $W_{ca,in}$, humidity, $\phi_{ca,in}$, and oxygen mole fraction, $y_{O_2,ca,in}$, which equals 0.21 if atmospheric air is supplied to the fuel cell. The stack temperature can be calculated using a model of stack heat transfer but it is presently assumed constant in this study. The water flow rate across the membrane is calculated by the membrane hydration model, Section 3.4, and the inlet flow properties are found in the humidifier model, Section 2.5. Figure 3.18 illustrates the calculation process in the cathode model.

Several assumptions are used. First, all gases are assumed to behave like an ideal gas. Second, the temperature of the fuel cell stack is perfectly controlled by the cooling system such that its temperature is maintained constant at $80°C$ and uniformly over the whole stack. Furthermore, the temperature of the flow inside the cathode flow channel is assumed to be equal to the stack temperature. Third, the variables of the flow exiting the cathode, namely temperature, $T_{ca,out}$, pressure, $p_{ca,out}$, humidity, $\phi_{ca,out}$, and oxygen mole fraction, $y_{O_2,ca,out}$, are assumed to be the same as the variables inside the cathode flow channel, T_{ca}, p_{ca}, ϕ_{ca}, and $y_{O_2,ca}$. Therefore, following the assumptions

$$T_{ca,out} = T_{ca} = T_{st} \tag{3.24a}$$

$$p_{ca,out} = p_{ca} \tag{3.24b}$$

$$\phi_{ca,out} = \phi_{ca} \tag{3.24c}$$

$$y_{O_2,ca,out} = y_{O_2,ca} \tag{3.24d}$$

Moreover, when the relative humidity of the cathode gas exceeds 100%, vapor condenses into a liquid form. This liquid water does not leave the stack and will either evaporate into the cathode gas if the gas humidity drops below 100% or it will accumulate in the cathode. Lastly, the flow channel and cathode backing layer are lumped into one volume, i.e. the spatial variations are ignored.

Three state equations are developed by continuity of the mass flow of oxygen, nitrogen and water.

$$\frac{dm_{O_2,ca}}{dt} = W_{O_2,ca,in} - W_{O_2,ca,out} - W_{O_2,reacted} \tag{3.25}$$
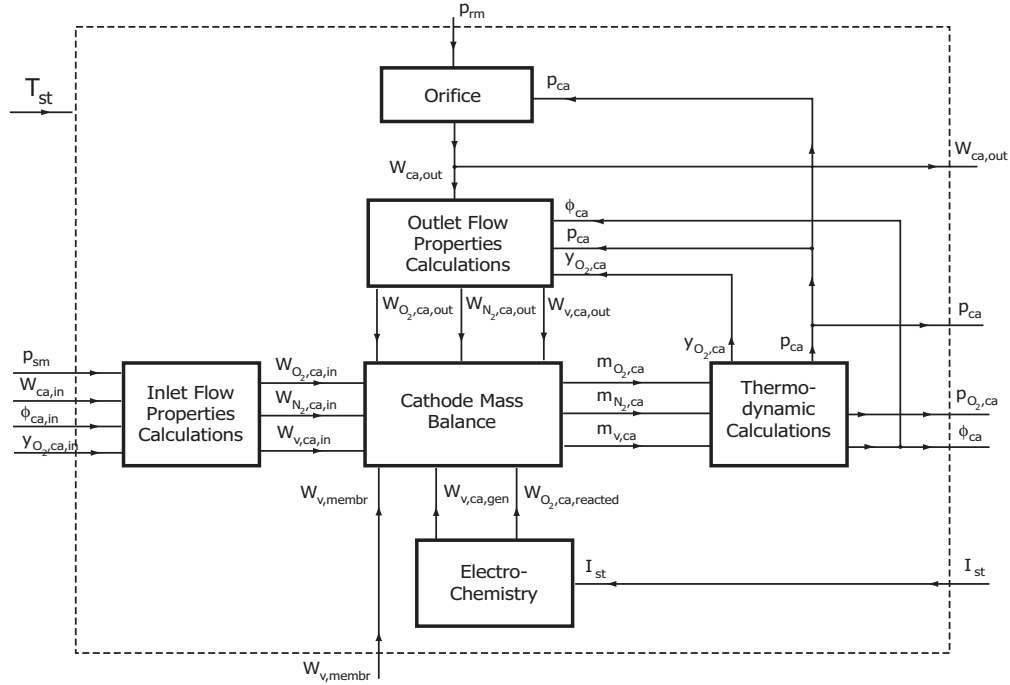
Figure 3.18: Cathode flow model

$$\frac{dm_{N_2,ca}}{dt} = W_{N_2,ca,in} - W_{N_2,ca,out} \tag{3.26}$$

$$\frac{dm_{w,ca}}{dt} = W_{v,ca,in} - W_{v,ca,out} + W_{v,ca,gen} + W_{v,membr} - W_{l,ca,out} \tag{3.27}$$

where $W_{O_2,ca,in}$ is the mass flow rate of oxygen gas entering the cathode

$W_{O_2,ca,out}$ is the mass flow rate of oxygen gas leaving the cathode

$W_{O_2,reacted}$ is the rate of oxygen reacted

$W_{N_2,ca,in}$ is the mass flow rate of nitrogen gas entering the cathode

$W_{N_2,ca,out}$ is the mass flow rate of nitrogen gas leaving the cathode

$W_{v,ca,in}$ is the mass flow rate of vapor entering the cathode

$W_{v,ca,out}$ is the mass flow rate of vapor leaving the cathode

$W_{v,ca,gen}$ is the rate of vapor generated in fuel cell reaction

$W_{v,membr}$ is the mass flow rate of water transfer across fuel cell membrane

$W_{l,ca,out}$ is the rate of liquid water leaving the cathode

All flows denoted with W terms have units of kg/sec. The inlet flow terms (subscript '*in*') are calculated from the inlet flow condition (model input). The cathode outlet mass flow rate, which calculation is shown below, together with the cathode outlet gas condition are used to calculate the '*out*' terms. The amount of oxygen reacted and vapor produced in the reaction is calculated from the stack current using electrochemical principles. The water flow across the membrane is determined from the membrane hydration model. The flow rate of liquid water leaving the cathode is zero, $W_{l,ca,out} = 0$, according to our assumptions. The calculation of the mass flow terms in the state equations (3.25)-(3.27) is explained in detail below.

The water inside the cathode volume can be in two forms, vapor and liquid, depending on the saturation state of the cathode gas. The maximum mass of vapor that the gas can hold is calculated from the vapor saturation pressure:

$$m_{v,max,ca} = \frac{p_{sat}V_{ca}}{R_v T_{st}} \tag{3.28}$$

where R_v is the gas constant of vapor. If the mass of water calculated in Equation (3.27) is more than that of the saturated state, the extra amount is assumed to condense into a liquid form instantaneously. Thus, the mass of vapor and liquid water is calculated by

$$\text{if } m_{w,ca} \leq m_{v,max,ca} \rightarrow \quad m_{v,ca} = m_{w,ca}, \quad m_{l,ca} = 0 \tag{3.29}$$

$$\text{if } m_{w,ca} > m_{v,max,ca} \quad \rightarrow m_{v,ca} = m_{v,max,ca}, \quad m_{l,ca} = m_{w,ca} - m_{v,max,ca} \tag{3.30}$$

Using the mass of oxygen, nitrogen, and vapor and the stack temperature, the pressure and the relative humidity of the gas inside the cathode channel can be calculated. First, using the ideal gas law, the partial pressures of oxygen, nitrogen and vapor inside the cathode flow channel can be calculated.

Oxygen Partial Pressure:

$$p_{O_2,ca} = \frac{m_{O_2,ca}R_{O_2}T_{st}}{V_{ca}} \tag{3.31}$$

Nitrogen Partial Pressure:

$$p_{N_2,ca} = \frac{m_{N_2,ca}R_{N_2}T_{st}}{V_{ca}} \tag{3.32}$$

Vapor Partial Pressure:

$$p_{v,ca} = \frac{m_{v,ca}R_vT_{st}}{V_{ca}} \tag{3.33}$$

where R_{O_2}, R_{N_2}, and R_v are gas constants of oxygen, nitrogen and vapor, respectively. The partial pressure of dry air is the sum of oxygen and nitrogen partial pressure

$$p_{a,ca} = p_{O_2,ca} + p_{N_2,ca} \tag{3.34}$$

The total cathode pressure, p_{ca}, is the sum of air and vapor partial pressure

$$p_{ca} = p_{a,ca} + p_{v,ca} \tag{3.35}$$

The oxygen mole fraction is determined from oxygen partial pressure and dry air partial pressure.

$$y_{O_2,ca} = \frac{p_{O_2,ca}}{p_{a,ca}} \tag{3.36}$$

The relative humidity of the cathode gas can be calculated from

$$\phi_{ca} = \frac{p_{v,ca}}{p_{sat}(T_{st})} \tag{3.37}$$

where p_{sat} is vapor saturation pressure, a function of temperature.

The inlet mass flow rate of oxygen ($W_{O_2,ca,in}$), nitrogen ($W_{N_2,ca,in}$), and vapor ($W_{v,ca,in}$) can be calculated from the inlet cathode flow condition using the thermodynamic properties discussed in Section 2.3. The saturation pressure is calculated using Equation (2.31). Then, the vapor pressure is determined using Equation (2.30):

$$p_{v,ca,in} = \phi_{ca,in}p_{sat}(T_{ca,in}) \tag{3.38}$$

Since humid air is the mixture of dry air and vapor, dry air partial pressure is therefore the difference between the total pressure and the vapor pressure

$$p_{a,ca,in} = p_{ca,in} - p_{v,ca,in} \tag{3.39}$$

The humidity ratio is then

$$\omega_{ca,in} = \frac{M_v}{M_{a,ca,in}} \frac{p_{v,ca,in}}{p_{a,ca,in}} \tag{3.40}$$

The air molar mass, M_a, is calculated by

$$M_{a,ca,in} = y_{O_2,ca,in} \times M_{O_2} + (1 - y_{O_2,ca,in}) \times M_{N_2} \tag{3.41}$$

where M_{O_2} and M_{N_2} are the molar mass of oxygen and nitrogen, respectively, and $y_{O_2,ca,in}$ is 0.21 for inlet air. The mass flow rate of dry air and vapor entering the cathode is

$$W_{a,ca,in} = \frac{1}{1 + \omega_{ca,in}} W_{ca,in} \tag{3.42}$$

$$W_{v,ca,in} = W_{ca,in} - W_{a,ca,in} \tag{3.43}$$

and the oxygen and nitrogen mass flow rate can be calculated by

$$W_{O_2,ca,in} = x_{O_2,ca,in} W_{a,ca,in} \tag{3.44}$$

$$W_{N_2,ca,in} = (1 - x_{O_2,ca,in}) W_{a,ca,in} \tag{3.45}$$

where $x_{O_2,ca,in}$, defined by $x_{O_2} = m_{O_2}/m_{dryair}$, is the oxygen mass fraction, which is a function of oxygen mole fraction

$$x_{O_2,ca,in} = \frac{y_{O_2,ca,in} \times M_{O_2}}{y_{O_2,ca,in} \times M_{O_2} + (1 - y_{O_2,ca,in}) \times M_{N_2}} \tag{3.46}$$

The mass flow rate in Equations (3.43), (3.44), and (3.45) are used in the state equations (3.25)-(3.27).

With the knowledge of the total flow rate at cathode exit, the mass flow rate of oxygen ($W_{O_2,ca,out}$), nitrogen ($W_{N_2,ca,out}$), and vapor ($W_{v,ca,out}$) at the exit are calculated in a similar manner as the inlet flow. The total flow rate is determined using the simplified orifice equation discussed in Section 2.2:

$$W_{ca,out} = k_{ca,out}(p_{ca} - p_{rm}) \tag{3.47}$$

where p_{ca} is the cathode total pressure, p_{rm} is the return manifold pressure (one of the model inputs), and $k_{ca,out}$ is the orifice constant. Using the mass flow rate in Equation (3.47) with conditions based on assumption (3.24), equations similar to (3.38)-(3.46) can be applied to the cathode exit flow in order to calculate $W_{O_2,ca,out}$, $W_{N_2,ca,out}$, and $W_{v,ca,out}$. The calculations are shown below in Equation (3.48). Note however that, unlike the inlet flow, the oxygen mole fraction of the cathode outlet flow, which equals $y_{O_2,ca}$, is not constant since oxygen is used in the reaction. It is calculated in Equation (3.36). The calculation of $W_{O_2,ca,out}$, $W_{N_2,ca,out}$, and $W_{v,ca,out}$ is as follows:

$$M_{a,ca} = y_{O_2,ca} \times M_{O_2} + (1 - y_{O_2,ca}) \times M_{N_2} \tag{3.48a}$$

$$\omega_{ca,out} = \frac{M_v}{M_{a,ca}} \frac{p_{v,ca}}{p_{a,ca}} \tag{3.48b}$$

$$W_{a,ca,out} = \frac{1}{1 + \omega_{ca,out}} W_{ca,out} \tag{3.48c}$$

$$W_{v,ca,out} = W_{ca,out} - W_{a,ca,out} \tag{3.48d}$$

$$x_{O_2,ca} = \frac{y_{O_2,ca} \times M_{O_2}}{y_{O_2,ca} \times M_{O_2} + (1 - y_{O_2,ca}) \times M_{N_2}} \tag{3.48e}$$

$$W_{O_2,ca,out} = x_{O_2,ca} W_{a,ca,out} \tag{3.48f}$$

$$W_{N_2,ca,out} = (1 - x_{O_2,ca}) W_{a,ca,out} \tag{3.48g}$$

Electrochemistry principles are used to calculate the rate of oxygen consumption and water production in the fuel cell reaction. The flow rate is a function of the stack current, I_{st}:

$$W_{O_2,reacted} = M_{O_2} \times \frac{nI_{st}}{4F} \tag{3.49}$$

$$W_{v,ca,gen} = M_v \times \frac{nI_{st}}{2F} \tag{3.50}$$

where n is the number of cells in the stack and F is the Faraday number = 96485 coulombs.

3.3   Anode Flow Model

In our model, hydrogen is supplied to the anode of the fuel cell stack by a hydrogen tank. It is assumed that the anode inlet flow rate can be instantaneously adjusted by a valve to maintain the minimum pressure difference between the cathode and the anode. Here, we assume that the the anode channel flow resistance is small as compared to the cathode flow resistance such that maintaining the pressure difference ensures sufficient flow of hydrogen (for the fuel cell reaction). Other assumptions similar to the cathode flow model are also used. The temperature of the flow is assumed to be equal to the stack temperature. It is assumed that the condition, namely pressure, temperature and humidity, of the anode outlet flow is the same as the condition of the gas in the anode flow channel. Additionally, the flow channel and the backing layer of all cells are lumped into one volume.

Similar to the cathode flow model, hydrogen partial pressure and anode flow humidity are determined by balancing the mass flow of hydrogen and water in the anode. Figure 3.19 illustrates mass flow in the anode. The inputs to the model, shown in Figure 3.20, consist of anode inlet (total) mass
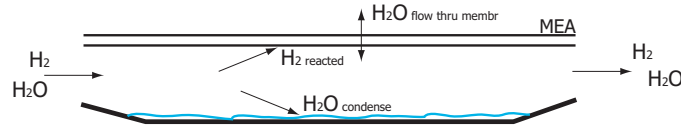
Figure 3.19: Anode mass flow

flow, $W_{an,in}$, inlet flow humidity, $\phi_{an,in}$, inlet flow pressure, $p_{an,in}$, inlet flow temperature, $T_{an,in}$, stack current, I_{st}, stack temperature, T_{st}, and vapor flow rate across the membrane, $W_{v,membr}$. The
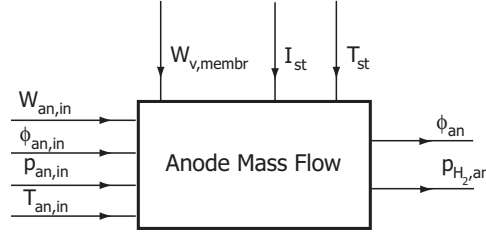
Figure 3.20: Anode block diagram

states are hydrogen mass, $m_{H_2,an}$, and water mass, $m_{w,an}$, inside the anode volume.

$$\frac{dm_{H_2,an}}{dt} = W_{H_2,an,in} - W_{H_2,an,out} - W_{H_2,reacted} \tag{3.51}$$

$$\frac{dm_{w,an}}{dt} = W_{v,an,in} - W_{v,an,out} - W_{v,membr} - W_{l,an,out} \tag{3.52}$$

where $W_{H_2,an,in}$ is the mass flow rate of hydrogen gas entering the anode
   $W_{H_2,an,out}$ is the mass flow rate of hydrogen gas leaving the anode
   $W_{H_2,reacted}$ is the rate of hydrogen reacted
   $W_{v,an,in}$ is the mass flow rate of vapor entering the anode
   $W_{v,an,out}$ is the mass flow rate of vapor leaving the anode
   $W_{v,membr}$ is the mass flow rate of water transfer across fuel cell membrane
   $W_{l,an,out}$ is the rate of liquid water leaving the anode

All flows denoted with W terms have units of kg/sec. If the mass of the water calculated in Equation (3.52) is more than the maximum that the anode gas can hold, the liquid water will form inside the anode volume:

$$\text{if } m_{w,an} \leq m_{v,max,an} \quad \rightarrow \quad m_{v,an} = m_{w,an} \quad, \quad m_{l,an} = 0 \tag{3.53}$$

$$\text{if } m_{w,an} > m_{v,max,an} \quad \rightarrow \quad m_{v,an} = m_{v,max,an} \quad , \quad m_{l,an} = m_{w,an} - m_{v,max,an} \tag{3.54}$$

where the maximum vapor mass is calculated from

$$m_{v,max} = \frac{p_{sat}V_{an}}{R_v T_{st}} \tag{3.55}$$

The mass of the hydrogen and vapor calculated is used to determine anode pressure, p_{an}, hydrogen partial pressure, p_{H_2}, and the relative humidity of the gas inside the anode, ϕ_{an}. The pressure is calculated using the ideal gas law.

Hydrogen Partial Pressure:

$$p_{H_2,an} = \frac{m_{H_2,an}R_{H_2}T_{st}}{V_{an}} \tag{3.56}$$

Vapor Partial Pressure:

$$p_{v,an} = \frac{m_{v,an}R_v T_{st}}{V_{an}} \tag{3.57}$$

Anode Pressure:

$$p_{an} = p_{H_2,an} + p_{v,an} \tag{3.58}$$

and the relative humidity of the gas inside the anode is

$$\phi_{an} = \frac{p_{v,an}}{p_{sat}(T_{st})} \tag{3.59}$$

where p_{sat} is calculated using Equation (2.31).

The inlet hydrogen mass flow, $W_{H_2,an}$, and vapor mass flow, $W_{v,an}$, are calculated using the anode inlet gas mass flow rate, $W_{an,in}$, and humidity, $\phi_{an,in}$. First, the vapor pressure is the function of the humidity:

$$p_{v,an,in} = \phi_{an,in} \cdot p_{sat}(T_{an,in}) \tag{3.60}$$

The hydrogen partial pressure of the inlet flow is

$$p_{H_2,an,in} = p_{an,in} - p_{v,an,in} \tag{3.61}$$

and the anode humidity ratio is

$$\omega_{an,in} = \frac{M_v}{M_{H_2}} \frac{p_{v,an,in}}{p_{an,in}} \tag{3.62}$$

where M_{H_2} and M_v are the molar masses of hydrogen and vapor, respectively. The mass flow rates of hydrogen and vapor entering the anode are

$$W_{H_2,an,in} = \frac{1}{1 + \omega_{an,in}}W_{an,in} \tag{3.63}$$

$$W_{v,an,in} = W_{an,in} - W_{H_2,an,in} \tag{3.64}$$

and are used in mass balance Equations (3.51) and (3.52). The rate of hydrogen consumed in the reaction is a function of the stack current

$$W_{H_2,reacted} = M_{H_2} \times \frac{nI}{2F} \tag{3.65}$$

The anode exit flow rate, $W_{an,out}$, represents the purge of anode gas to remove both liquid water and other gases accumulated in the anode (if reformed hydrogen is used). For the current system, it is assumed that the purge is zero. However, if the purge rate is known, the outlet hydrogen and vapor mass flow rate is calculated by the following equations

$$\omega_{an,out} = \frac{M_v}{M_{H_2,an}} \frac{p_{v,an}}{p_{H_2,ca}} \tag{3.66a}$$

$$W_{H_2,an,out} = \frac{1}{1 + \omega_{an,out}}W_{an,out} \tag{3.66b}$$

$$W_{v,an,out} = W_{an,out} - W_{H_2,an,out} \tag{3.66c}$$

It is assumed that the liquid water is stored in the anode and there is no passage available for it to leave the stack. Thus, the rate of liquid water leaving the anode, $W_{l,an,out}$, is set to zero. The rate of water flow across the membrane, $W_{v,membr}$, is determined in the membrane hydration model which is explained in the next section.

3.4   Membrane Hydration Model

The membrane hydration model represents the water content in the membrane and the rate of mass flow of water across the membrane. Both water content and mass flow are assumed to be uniform over the surface area of the membrane. The membrane water content and the rate of mass flow across the membrane are functions of the stack current and the relative humidity of the flow inside the anode and the cathode flow channels (Figure 3.21). The relative humidity of the cathode and anode flow are the output of the cathode flow model and anode flow model, respectively.
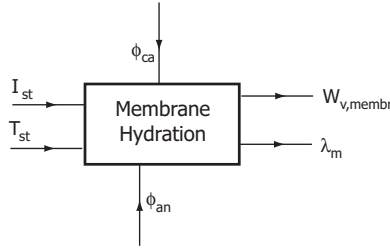
Figure 3.21: Membrane hydration model block

The water transport across membrane is achieved through two distinct phenomena [82, 100]:

- Water molecules are dragged across the membrane from anode to cathode by the hydrogen proton. This phenomenon is called electro-osmotic drag. The amount of water transported is represented by the electro-osmotic drag coefficient, n_d, which is defined as the number of water molecules carried by each proton

$$N_{v,osmotic} = n_d \frac{i}{F} \tag{3.67}$$

where $N_{v,osmetic}$ (mol/(sec $\cdot$ cm^2)) is the net water flow from anode to cathode
of one cell caused by electro-osmotic drag
i (A/cm^2) is the stack current density defined in (3.10)
F is the Faraday's number

- In a detailed spatially distributed system, there is a gradient of water concentration across the membrane that is caused by the difference in humidity in anode and cathode flows. This water concentration gradient, in turn, causes "back-diffusion" of water from cathode to anode.

$$N_{v,diff} = D_w \frac{dc_v}{dy} \tag{3.68}$$

where $N_{v,diff}$ (mol/(sec $\cdot$ cm^2)) is the net water flow from cathode to anode
of one cell caused by back-diffusion
c_v (mol/cm^3) is the water concentration defined below in Equation (3.77)
y (cm) is the distance in the direction normal to the membrane
D_w (cm^2/sec) is the diffusion coefficient of water in the membrane.

Combining the two water transports and approximating the water concentration gradient in the membrane to be linear over the membrane thickness, the water flow across the membrane can be

written as (assuming positive values in the direction from anode to cathode)

$$N_{v,membr} = n_d \frac{i}{F} - D_w \frac{(c_{v,ca} - c_{v,an})}{t_m} \tag{3.69}$$

where t_m (cm) is the thickness of the membrane. For a particular membrane, the electro-osmotic coefficient, n_d, and the diffusion coefficient, D_w, varies with water content in the membrane, which depends on the water content in the gas next to the membrane. Since Equation (3.69) gives the flow rate of water per unit area in (mol/(sec · cm^2)) in one fuel cell, the total stack mass flow rate across the membrane, $W_{v,membr}$, can be calculated from

$$W_{v,membr} = N_{v,membr} \times M_v \times A_{fc} \times n \tag{3.70}$$

where M_v is the vapor molar mass, A_{fc} (cm^2) is the fuel cell active area, and n is the number of fuel cells in the stack.

The average between the water contents in the anode flow and the cathode flow can be used to represent the membrane water content. However, using the water content in the anode flow presents a more conservative approach, as discussed in [82], since the membrane water content tends to be lower on the anode side. This is because at high current density, water transport from anode to cathode by electro-osmotic drag exceeds the water back-diffusion from cathode to anode. The membrane water content, and thus the electro-osmotic and diffusion coefficients, can be calculated using the activities of the gas in the anode and the cathode:

$$a_i = \frac{y_{v,i} p_i}{p_{sat,i}} = \frac{p_{v,i}}{p_{sat,i}} \tag{3.71}$$

which, in the case of gas, is equivalent to relative humidity, ϕ_i. The index i is either anode (an) or cathode (ca), $y_{v,i}$ is the mole fraction of vapor, p_i is the total flow pressure, $p_{sat,i}$ is the vapor saturation pressure, and $p_{v,i}$ is the vapor partial pressure. The water concentration in the anode flow, $c_{v,an}$, and the cathode flow, $c_{v,ca}$, are also functions of the activation of water in the anode flow, a_{an}, and in the cathode flow, a_{ca}, respectively.

A summary of equations used in calculating the electro-osmotic drag coefficient, membrane water diffusion coefficient, and membrane water concentration is presented in [39]. The equations are developed based on experimental results measured for Nafion 117 membrane in [100]. The water content in the membrane, λ_i, defined as the ratio of water molecules to the number of charge sites [100], is calculated from water activities a_i (subscript i is either an-anode, ca-cathode, or m-membrane).

$$\lambda_i = \begin{cases} 0.043 + 17.81a_i - 39.85a_i^2 + 36.0a_i^3 & , 0 < a_i \leq 1 \\ 14 + 1.4(a_i - 1) & , 1 < a_i \leq 3 \end{cases} \tag{3.72}$$

where

$$a_m = \frac{a_{an} + a_{ca}}{2} \tag{3.73}$$

The membrane average water content, λ_m, is calculated by Equation (3.72) using the average water activity, a_m, between the anode and cathode water activities. The value of λ_m is used to represent the water content in the membrane. The electro-osmotic drag coefficient, n_d, and the water diffusion coefficient, D_w, are then calculated from the membrane water content[1], λ_m [39].

$$n_d = 0.0029\lambda_m^2 + 0.05\lambda_m - 3.4 \times 10^{-19} \tag{3.74}$$

and

$$D_w = D_\lambda \exp\left(2416\left(\frac{1}{303} - \frac{1}{T_{fc}}\right)\right) \tag{3.75}$$

---

[1]Membrane water content on the anode side is used in [39] since membrane dehydration is of more concern. However, we will consider both membrane dehydration and membrane water flooding cases.

where

$$D_\lambda = \begin{cases} 10^{-6} & , \lambda_m < 2 \\ 10^{-6}(1 + 2(\lambda_m - 2)) & , 2 \leq \lambda_m \leq 3 \\ 10^{-6}(3 - 1.67(\lambda_m - 3)) & , 3 < \lambda_m < 4.5 \\ 1.25 \times 10^{-6} & , \lambda_m \geq 4.5 \end{cases} \tag{3.76}$$

and T_{fc} (equals T_{st} in our model) is the temperature of the fuel cell in Kelvin. The water concentration at the membrane surfaces on anode and cathode sides, used in Equation (3.69), is a function of membrane water content.

$$c_{v,an} = \frac{\rho_{m,dry}}{M_{m,dry}}\lambda_{an} \tag{3.77}$$

$$c_{v,ca} = \frac{\rho_{m,dry}}{M_{m,dry}}\lambda_{ca} \tag{3.78}$$

where $\rho_{m,dry}$ (kg/cm^3) is the membrane dry density and $M_{m,dry}$ (kg/mol) is the membrane dry equivalent weight.

Table 3.2: Thermodynamic constants used in the model

Symbol	Variable	Value
p_{atm}	atmospheric pressure	101.325 kPa
T_{atm}	atmospheric temperature	298.15 K
γ	ratio of specific heat of air	1.4
C_p	constant pressure specific heat of air	1004 J/(mol·K)
ρ_a	air density	1.23 kg/m^3
$\bar{R}$	universal gas constant	8.3145 J/(mol·K)
R_a	air gas constant	286.9 J/(kg·K)
R_{O_2}	oxygen gas constant	259.8 J/(kg·K)
R_{N_2}	nitrogen gas constant	296.8 J/(kg·K)
R_v	vapor gas constant	461.5 J/(kg·K)
R_{H_2}	hydrogen gas constant	4124.3 J/(kg·K)
M_{O_2}	oxygen molar mass	32×10^{-3} kg/mol
M_{N_2}	nitrogen molar mass	28×10^{-3} kg/mol
M_v	vapor molar mass	18.02×10^{-3} kg/mol
M_{H_2}	hydrogen molar mass	2.016×10^{-3} kg/mol
F	Faraday number	96485 coulombs

To form the fuel cell stack model, the membrane hydration model is integrated with the stack voltage, the cathode flow, and the anode flow models developed in Sections 3.1, 3.2, and 3.3, respectively. Combining the fuel cell stack model described in this chapter with the auxiliary models described in Chapter 2 forms the dynamics of the fuel cell reactant supply system. In the next chapter, simulation results of the system model are presented and the dynamic effects of the air supply subsystem during transient operation of the fuel cell system are demonstrated.

Chapter 4

Fuel Cell System Model: Analysis and Simulation

The system model development in Chapters 2 and 3 focuses on the reactant supply systems which include the air flow control, hydrogen feed from a high-pressure tank, and the humidification of the reactant feeds. In a direct H_2 system, the PEM fuel cell becomes the main heat source. Due to the low operating temperature in PEMFCs, the dynamics of the stack temperature are considered to be relatively slow and, thus, can be viewed as a separate subsystem. As a result, the stack temperature is considered as a setpoint to the reactant systems. The control inputs are the compressor motor voltage, the hydrogen valve, and the humidifier water injection commands. In this chapter, we integrate into the model a static controller for the humidifier and a proportional controller for the hydrogen tank valve. Note here that when a fuel cell system runs based on compressed H_2 that is stored in cylinders, the air flow dynamics and the humidity management dominate the fuel cell system response. By assuming a perfect controller for the humidification, we decouple the phenomena of the air flow from the humidity. This enables us to focus on the air supply dynamics behavior and its control design. A steady-state analysis of the model presented in Section 4.2 is performed to determine the optimal air flow setpoints in terms of maximum net system power. The result corresponds with the value given in the literature as fuel cell specifications. In addition to the steady-state simulation, the dynamic model developed is also able to simulate the transient behavior of the system. The results from transient simulation are shown in Section 4.3. The transient behaviors agree with experimental data published in the literature.

The parameters used in the model are given in Table 4.1. The fuel cell stack is based on the 75 kW stacks used in the FORD P2000 fuel cell prototype vehicle [1]. The active area of the fuel cell is calculated from the peak power of the stack. The compressor model represents the Allied Signal compressor given in [30]. The membrane properties of Nafion 117 membrane are obtained from [82]. The values of volumes are approximated from the dimensions of the P2000 fuel cell system.

4.1 Humidifier and Hydrogen Flow Controls

In order to concentrate on the air supply dynamics, it is necessary to develop controls for the anode hydrogen valve and the humidifier. A static control of water injection in the humidifier is developed using thermodynamic calculations. The objective is to maintain the desired humidity of the air flow entering the stack. It is assumed here that all necessary signals are available. The proportional control is used to control the hydrogen flow, with the objective of minimizing the pressure difference across the membrane.

Table 4.1: Parameters used in the simulations

Symbol	Variable	Value
$\rho_{m,dry}$	membrane dry density	0.002 kg/cm^3
$M_{m,dry}$	membrane dry equivalent weight	1.1 kg/mol
t_m	membrane thickness	0.01275 cm
n	number of cell in fuel cell stack	381
A_{fc}	fuel cell active area	280 cm^2
d_c	compressor diameter	0.2286 m
J_{cp}	compressor and motor inertia	5×10^{-5} kg·m^2
V_{an}	anode volume	0.005 m^3
V_{ca}	cathode volume	0.01 m^3
V_{sm}	supply manifold volume	0.02 m^3
V_{rm}	return manifold volume	0.005 m^3
$C_{D,rm}$	return manifold throttle discharge coefficient	0.0124
$A_{T,rm}$	return manifold throttle area	0.002 m^2
$k_{sm,out}$	supply manifold outlet orifice constant	0.3629×10^{-5} kg/(s·Pa)
$k_{ca,out}$	cathode outlet orifice constant	0.2177×10^{-5} kg/(s·Pa)

4.1.1   Humidifier Control

Due to the lack of publicly available fuel cell data, the model developed in this study has not been validated with a real fuel cell experimental system. Several parameters are out-dated, especially the parameters used in the calculation of water flow rate across the membrane (membrane hydration model), and those that are used to represent the effect of membrane humidity to the cell voltage (stack voltage model). As will be shown in Section 4.3, the model always predicts dehydration in the anode which results in considerable drops in fuel cell voltage. Simulations under these conditions are not considered as meaningful. Therefore, until extensive experimental data becomes available, it is more appropriate to assume that the membrane is always fully humidified by other passive means, thus $\lambda_m = 14$ in (3.21). These assumptions are applicable since there are great efforts in the fuel cell industry to develop a self-humidifying stack by re-designing stack components such as flow fields and backing layers [101, 112]. The goal of the reactant humidity control then becomes the regulation of the humidity of the stack inlet flow.

In the humidifier, the amount of water injected into the air flow, $W_{v,inj}$, is assumed to be the exact amount that is required to maintain the desired stack inlet humidity, ϕ^{des}. This amount can be calculated with the knowledge of the conditions of the humidifier inlet flow, which corresponds to the cooler exit flow (Figure 2.1). The inlet condition includes flow rate, W_{cl}, temperature, T_{cl}, humidity, ϕ_{cl}, and pressure, p_{cl}. Using equations (2.35) to (2.39), we can calculate the dry air mass flow rate, $W_{a,cl}$, the vapor mass flow rate, $W_{v,cl}$, and the dry air pressure, $p_{a,cl}$. Then, the flow rate of vapor injected is calculated by

$$W_{v,inj} = \frac{M_v}{M_a} \frac{\phi^{des} P_{sat}(T_{cl})}{p_{a,cl}} W_{a,cl} - W_{v,cl} \tag{4.1}$$

where M_v and M_a are the molar mass of vapor and dry air, respectively. With this assumption of perfect humidifier control, the calculation of the humidifier static model is simplified. The cathode inlet flow rate and pressure are

$$W_{ca,in} = W_{cl} + W_{v,inj} = W_{sm,out} + W_{v,inj} \tag{4.2}$$

and

$$p_{ca,in} = p_{a,cl} + \phi^{des} p_{sat}(T_{cl}) \tag{4.3}$$

respectively.

4.1.2 Hydrogen valve control

In the system considered in this study, hydrogen is supplied by a high-pressure tank and the flow rate is controlled by a valve. Since the high-pressured storage acts as a high-energy source, the hydrogen flow rate can be adjusted rapidly. With the fast actuator and fast dynamics of the anode volume, the anode hydrogen flow control can have high loop bandwidth. The goal of the hydrogen flow control is to minimize the pressure difference across the membrane, i.e., the difference between anode and cathode pressures. Using simple proportional control based on the pressure difference, the pressure in the anode can quickly follow the changes in the cathode pressure. Since the valve is fast, it is assumed that the flow rate of hydrogen can be directly controlled based on the feedback of the pressure difference. However, the actual cathode and anode pressures cannot be directly measured. Thus, on the cathode side, the supply manifold pressure is used in the controller. On the anode side, since we assume that the anode supply manifold is small and its volume is lumped together with the anode volume, i.e. they have the same pressure, the anode pressure is used in the controller. The controller is in the form

$$W_{an,in} = K_1(K_2 p_{sm} - p_{an}) \tag{4.4}$$

where $K_1 = 2.1 \ (\frac{\text{kg/s}}{\text{kPa}})$ is the proportional gain and $K_2 = 0.94$ takes into account a nominal pressure drop between the supply manifold and the cathode. The anode and cathode pressure responses for a series of current load changes in Figure 4.1 shows the performance of the hydrogen flow proportional control. The anode pressure tracks the cathode pressure very well.
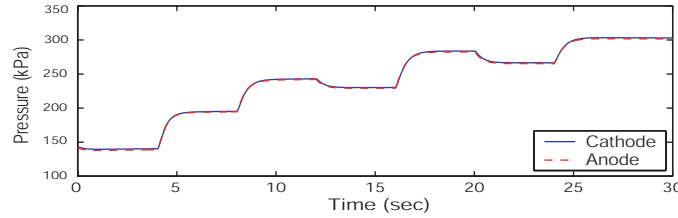

Figure 4.1: Cathode and anode pressures in nonlinear simulation

Typically, there is also a purge valve at the end of the anode, which presents an additional control actuator. The purpose of the purge valve is to remove the liquid water accumulation in the anode to prevent flooding. Our model, however, does not incorporate water flooding effects. Therefore, the purge valve is not needed and, as a result, the anode is assumed to be dead-end.

4.2 Steady-State Analysis

By applying the humidifier static control and the hydrogen valve proportional control explained in the previous section, the dynamics of the fuel cell system are governed mainly by the air supply system dynamics. The air supply system has a compressor motor command as the only control actuator. Two variables considered for the control performance are the concentration of the oxygen in the cathode and the fuel cell system net power.

The net power, P_{net}, of the fuel cell system is the difference between the power produced by the stack, P_{st}, and the parasitic power required to run the auxiliary components. The majority of the parasitic power is caused by the air compressor. Therefore, it is the only parasitic loss considered in this study. For certain stack currents, the stack voltage increases with increasing air flow rate to the stack since the cathode oxygen partial pressure increases. The excess amount of air flow provided to the stack is normally indicated by the term oxygen excess ratio, λ_{O_2}, defined as the ratio of oxygen supplied to oxygen used in the cathode, i.e.,

$$\lambda_{O_2} = \frac{W_{O_2,in}}{W_{O_2,react}} \tag{4.5}$$

High oxygen excess ratio, and thus high oxygen partial pressure, improves P_{st} and P_{net}. However, after an optimum value of λ_{O_2} is reached, further increase will cause an excessive increase in compressor power and thus deteriorate the system net power. To study the optimal value of λ_{O_2}, we plot steady-state values of λ_{O_2} and P_{net}, obtained from the simulation, for different I_{st}, as shown in Figure 4.2. For the current fuel cell system, the highest net power is achieved at an oxygen excess ratio between 2 and 2.4 depending on the stack current. For simplicity, it is therefore desired to control the air flow to $\lambda_{O_2} = 2$.
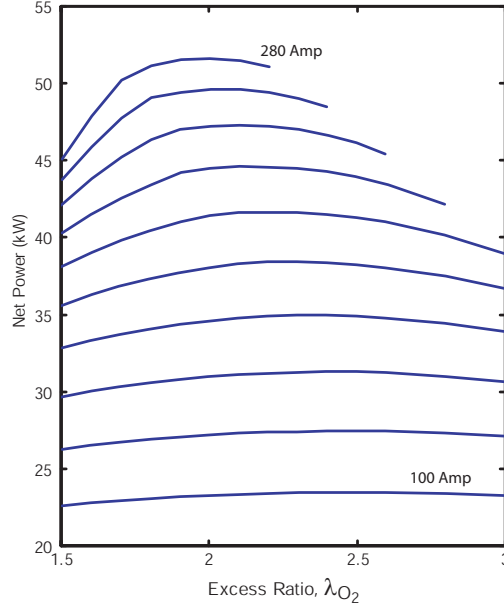

Figure 4.2: System net power at different stack currents and oxygen excess ratios

4.3   Dynamic Simulation

A series of step changes in stack current is applied as input, as shown in Figure 4.3(a). A series of compressor motor input voltage, Figure 4.3(b), which gives different levels of steady-state oxygen excess ratios, shown in Figures 4.3(e), is also applied. This represents the simple static feedforward controller of the compressor motor based on the measurement of the current load, as shown in Figure 4.4.

During a positive current step, the oxygen excess ratio drops, as shown in Figure 4.3(e), due to the depletion of oxygen. This, in turn, causes a significant drop in the stack voltage, as shown in Figure 4.3(c). If the compressor voltage responds instantaneously during the current step (at 2, 6, 10 and 14 seconds), there is still a transient effect in the stack voltage, and consequently in the stack power and the net power (Figure 4.3(c)), as a result of the transient behavior in oxygen partial pressure (Figure 4.3(f)). The step at $t = 18$ seconds shows the response of giving a step increase in the compressor input while keeping constant stack current. An opposite case is shown at $t = 22$ seconds.

The steady-state response at 16 and 20 seconds shows the effect of running the system at λ_{O_2} higher than the optimum value. It can be seen in Figure 4.3(c) that even though the stack power increases, the net power decreases due to the high power drawn from the compressor motor.

Figure 4.5 shows the fuel cell response on the polarization map at $80°C$. Similar results were obtained in the experiment of fuel cell load switching presented in [70]. The compressor transient response is shown in Figure 4.6. Figure 4.7 shows the voltage response when considering the humidity of the membrane.

The fuel cell system model is capable of capturing the effects of transient oxygen and hydrogen
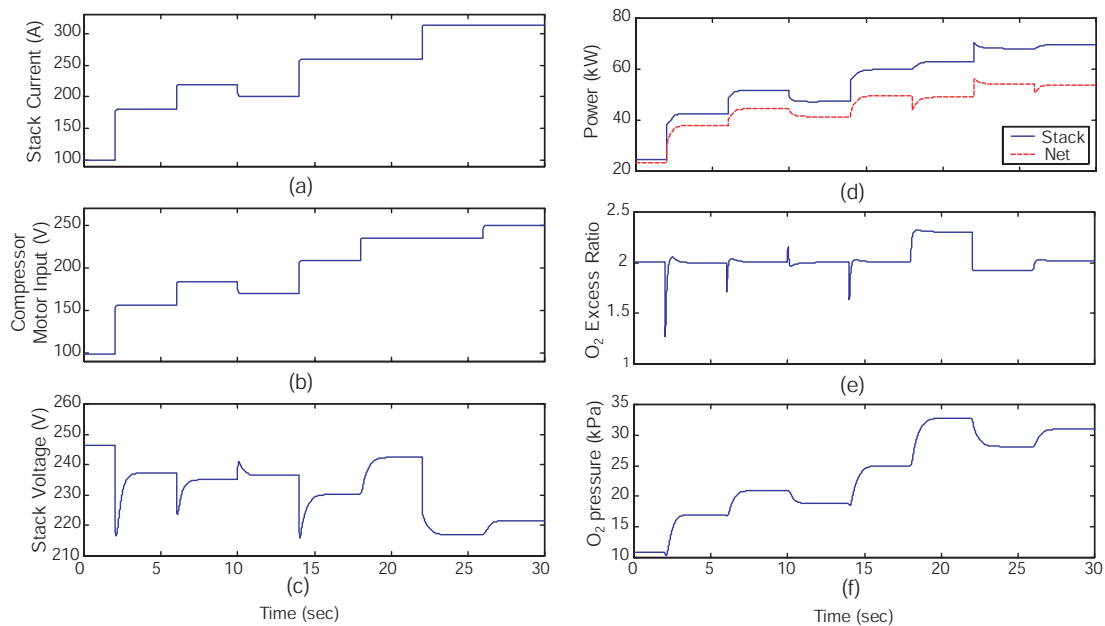
Figure 4.3: Simulation results of the fuel cell system model for a series of input step changes
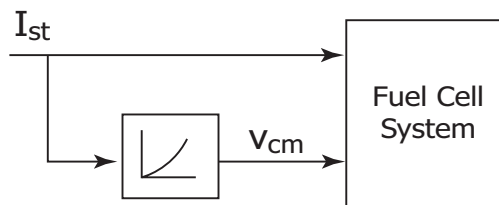
Figure 4.4: Static feedforward using steady-state map
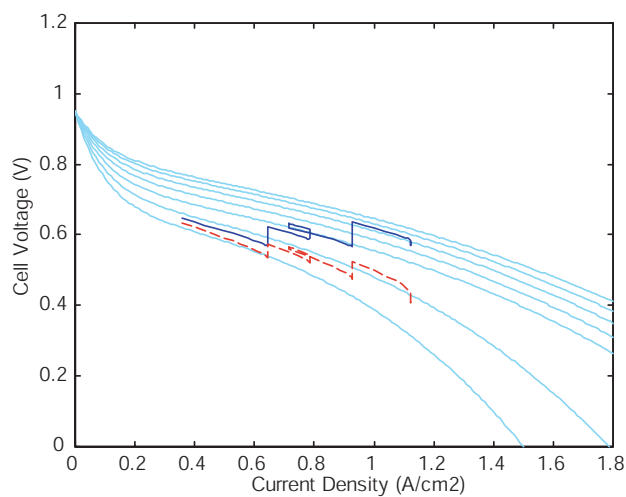
Figure 4.5: Fuel cell response on polarization curve. Solid line assumes fully humidified membrane; dashed line represents drying membrane.
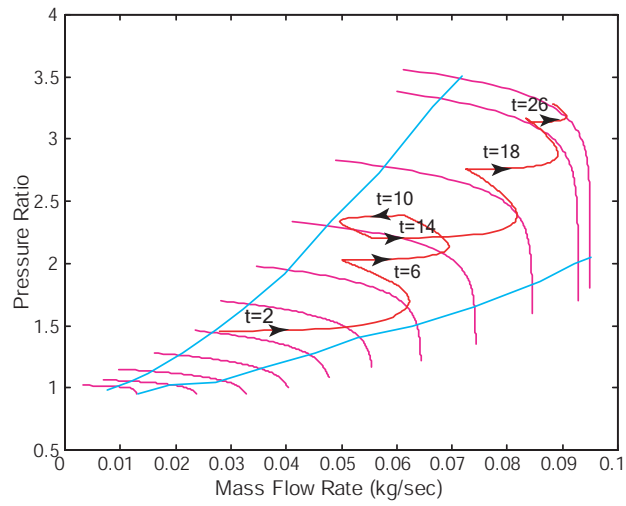
Figure 4.6: Compressor transient response on compressor map
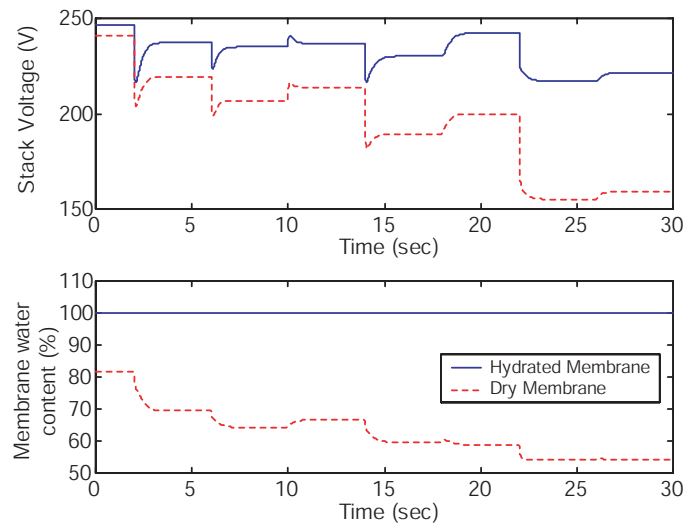
Figure 4.7: Voltage response comparing fully humidified membrane and drying membrane

partial pressures and the membrane humidity on the fuel cell voltage. Even though the model has not been validated with an actual experimental system, the model predicts transient behavior similar to that reported in the literature [70, 87]. It can be seen that the drops in fuel cell voltage are significant during fast load changes if the compressor motor is controlled with static feedforward based on the steady-state map. In the next chapter, a controller that gives better dynamic responses is developed using the model-based approach. Several control configurations are also considered.

Chapter 5

Air Flow Control for Fuel Cell Cathode Oxygen Reactant

There are three major control subsystem loops in the fuel cell system (FCS) that regulate the air/fuel supply, the water management, and the heat management [1]. We assume here a perfect air/fuel flow humidifier, and incoming air and stack cooler. These perfect conditions are implemented in the simulation model by either fixing some variables or by employing simple static controllers described in the previous Chapter. Moreover, the fast proportional feedback controller on the fuel flow ensures that the anode pressure is equal to the cathode pressure following almost instantaneously any pressure variation in the cathode side. All these controllers and assumptions that are by no means trivial to implement on a real system, allow us to focus on controlling the cathode oxygen supply.

In this Chapter we concentrate on the air supply subsystem of the fuel cell (FC) in order to regulate (and replenish) the oxygen depleted from the FC cathode during power generation, and in particular, current demands from the vehicle power management system. This task needs to be achieved fast and efficiently to avoid oxygen starvation and extend the life of the stack [111]. Oxygen starvation is a complicated phenomenon that occurs when the partial pressure of oxygen falls below a critical level at any possible location within the meander of the air stream in the cathode [99]. It can be observed by a rapid decrease in cell voltage that in severe cases can cause a short circuit and a hot spot on the surface of a membrane cell. Before this catastrophic event happens, the stack diagnostic system that monitors individual cell voltage removes the current from the stack or triggers "shut-down."

Although the phenomenon is spatially variant, it is largely believed that it can be avoided by regulating the excess oxygen ratio in the cathode, λ_{O_2}, which is a lumped (spatially invariant) variable. This can be achieved by controlling the compressor motor to provide the air and hence the oxygen that is depleted due to the current drawn from the fuel cell. As shown in the previous chapter, there is an excess oxygen ratio that maximizes the net power from the FC system (generated FC power minus consumed compressor motor power) for each current drawn, $\lambda_{O_2}^{des} = \lambda_{O_2}^{des}(I_{st})$.

For simplification we assume for now a fixed $\lambda_{O_2}^{des} = 2$. In the future, extremum seeking or other maximum-finding techniques can be used to search on-line for the optimum excess oxygen ratio levels. Note here that in a low pressure air supply system, e.g., using a blower, where there are no pressure variations, regulation of λ_{O_2} corresponds to regulation of the oxygen partial pressure.

The control problem is challenging because of actuator and sensor limitations. The variables manipulated via the actuator are upstream of where the disturbance affects the performance variable (see Figure 5.1) limiting the realistic disturbance rejection capabilities of the system. Given that the exogenous input (stack current) is measured, a feedforward controller that cancels the effect of current to oxygen excess ratio is theoretically feasible. The design of such an ideal controller, called from now on the "cancellation" controller, is based on inverting the linearized plant model in Section 5.4. The performance and the limitations of the cancellation feedforward controller are also presented.

In Section 5.5, a two Degrees Of Freedom (2DOF) controller is designed based on a static pre-
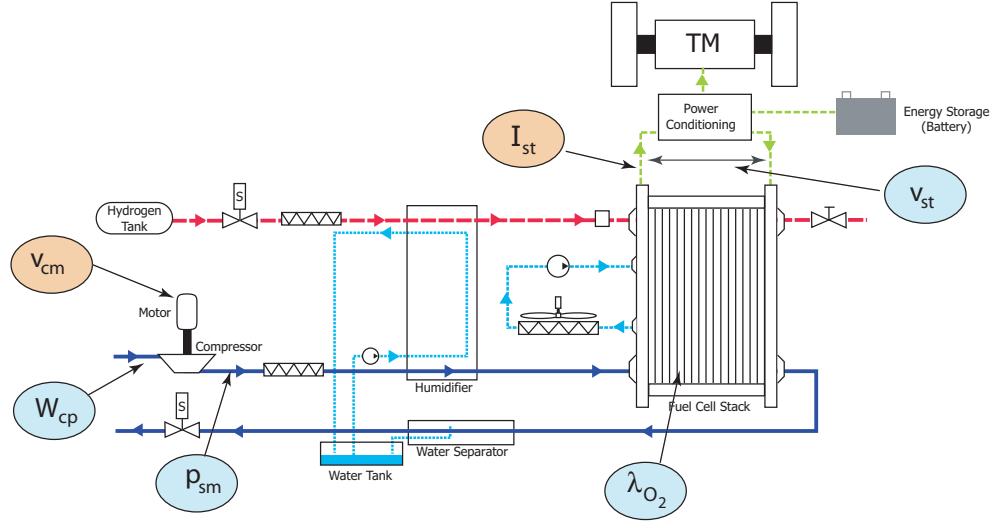
Figure 5.1: Fuel cell system showing control inputs and outputs

compensator and an integral observer-based output feedback controller. The challenge here arises from the fact that not all the states, nor the performance variable, λ_{O_2}, are measured. Moreover, the traditionally used measurements for λ_{O_2} regulation are upstream of the performance variable due to difficulties in sensing within a vapor saturated flow stream. In Section 5.6 we demonstrate that the FCS voltage increases the system observability and thus enables a higher gain controller that improves transient λ_{O_2} regulation and robustness significantly. Currently, voltage is used in diagnostic and emergency shut-down procedures due to its fast reaction to oxygen starvation, but we clearly define its usefulness and use in a feedback design.

The FCS voltage is a natural feedback measurement for the FCS air controller and in hindsight of our results, one can view it as one of the FCS performance variables. Fast regulation of the FCS voltage to its desired value can be an indirect measure of a good level of oxygen concentration in the FC cathode. Regulating FC voltage during current demands, however, can create infeasible power set-points and lead to instability.

Apart from an indication of oxygen starvation, the FCS voltage is an important FC performance variable. In particular, the FCS is viewed as a power source from the DC/DC converter or other power electronics connected to it as shown in Figure 5.1. Its Current-to-Voltage transfer function defines the "power quality" of the FC as a power source [74]. The air controller designed in this section affects the closed loop Current-to-Voltage FC transfer function. We show in this chapter that the observer-based feedback controller with Voltage measurement resembles a passive resistive power source, i.e., for all current steps up 0.3 rad/sec, the FCS voltage behaves as $V_{st} = R_{st}I_{st}$ with a small $R_{st} = 0.05$ Ω. This result can now be used by researchers who design the power electronics for the connection of the FCS with a DC or an AC motor/generator unit for power transfer. There is also ample interest from the power generation community for the dynamics of the FCS system when connected to a grid of heterogeneous power sources [93, 74]. Many studies thus far [107] have used a static polarization curve for the Current-to-Voltage relation, which assumes a perfect or a non-existent FC reactant flow controller.

In Section 5.9 we analyze the tradeoff between the oxygen excess ratio and the FCS system parasitic losses during transient conditions. Namely, the power utilized by the supercharger is a parasitic loss for the FC stack. We show that minimizing these parasitic losses and providing fast air flow regulation are conflicting objectives. The conflict arises from the fact that the supercharger is using part of the stack power to accelerate. One way to resolve this conflict is to augment the FC system with an auxiliary battery or an ultracapacitor that can drive the auxiliary devices or can potentially buffer the FC from transient current demands. These additional components, however, will introduce complexity

and additional weight that might not be necessary [91]. To judiciously decide about the system architecture and the component sizing we analyze the tradeoff between the two objectives using linear control techniques. We then show that a compromise needs to be made between oxygen starvation and FC net power for transients faster than 0.7 rad/sec (see Figure 5.33). In other words, if net power response that is faster than 1.4 second time constant is required, our analysis suggests the use of an auxiliary power source such as a battery or capacitor. Although this answer is specific to our system, our analysis procedure is general and can be applied to other fuel cell systems.

5.1 Control Problem Formulation

As discussed in the previous chapter, the combined control design objective is to define the compressor motor input voltage, v_{cm}, in order to maintain $\lambda_{O_2} = 2$ and achieve the desired fuel cell system net power, P_{net}^{ref}. The desired net power can be translated into required stack current $I_{st} = f_{I_{st}P_{net}^{ref}}(P_{net}^{ref})$ assuming that the system is operated at the desired condition. The current is then considered as an external input or disturbance to the system. The resulting control problem is defined as follows (Figure 5.2):

$$\dot{x} = f(x, u, w) \qquad \text{State Equations} \qquad (5.1)$$

$$x = \begin{bmatrix} m_{O_2} & m_{H_2} & m_{N_2} & \omega_{cp} & p_{sm} & m_{sm} & m_{w,an} & m_{w,ca} & p_{rm} \end{bmatrix}^T$$

$$u = v_{cm}$$

$$w = I_{st}$$

The potential measurements include air flow rate through the compressor, W_{cp}, supply manifold pressure, p_{sm}, and stack voltage, v_{st}.

$$y = [W_{cp}\, p_{sm}\, v_{st}]^T = h_y(x, u, w) \qquad \text{Measurements} \qquad (5.2)$$

$$z = [e_{P_{net}}\, \lambda_{O_2}]^T = h_z(x, u, w) \qquad \text{Performance Variables} \qquad (5.3)$$

where $e_{P_{net}}$ is defined as the difference between the desired and the actual system net power, i.e., $e_{P_{net}} = P_{net}^{ref} - P_{net}$. Figure 5.1 illustrates the location of the variables in (5.2).
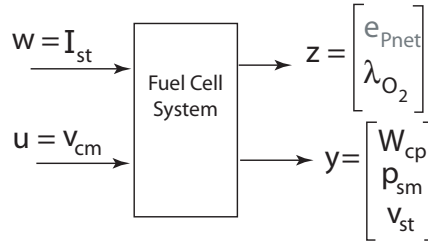
Figure 5.2: Control problem formulation

We define the two control objectives $e_{P_{net}} = 0$ and $\lambda_{O_2} = 2$, but focus on the problem of using the compressor motor voltage, v_{st}, to regulate the oxygen excess ratio for the first sections of this Chapter. Note that the two objectives are both achievable at steady-state, but their transients are considerably different, and thus, cannot be achieved simultaneously by a single control actuator. The objective of achieving the desired transient system net power is ignored in the first part of the chapter, which represents the case where the power management system can rely on a secondary power source such as a battery. The tradeoff between the two performance variables, i.e., $e_{P_{net}}$ and λ_{O_2}, is discussed in the last section of this chapter.

5.2   Control Configurations

The different control schemes for the fuel cell stack system are illustrated in Figure 5.3. Because the current that acts as a disturbance to λ_{O_2} can be measured, a static function that correlates the steady-state value between the control input, v_{cm}, and the disturbance, I_{st}, could be used in the feedforward path. This static feedforward is easily implemented with a look-up table (shown in Figure 5.3(a)).

    The calculation of the static feedforward is based on finding the compressor voltage command, v_{cm}^*, that achieves the air flow that replenishes the oxygen flow that, in turn, is depleted by the reaction of hydrogen protons with oxygen molecules during a current command, I_{st}. For specific ambient conditions (pressure, temperature, and humidity), the required air flow can be calculated analytically from the stack current, $W_{cp}^* = f_{cp}(I_{st})$, based on electrochemical and thermodynamic principles. The inversion of compressor and compressor motor maps to find $v_{cm}^* = f_{cm}(I_{st})$ that gives the desired air flow, W_{cp}^*, is not trivial. Nonlinear simulations or testing in an experimental facility can determine the static feedforward controller from "w to u" that cancels the effect "w to z_2" at steady-state (zero frequency).

Open Loop/ Static Feedforward

(a)

Dynamic Feedforward/ Cancellation

(b)

Feedback + Static Feedforward

(c)
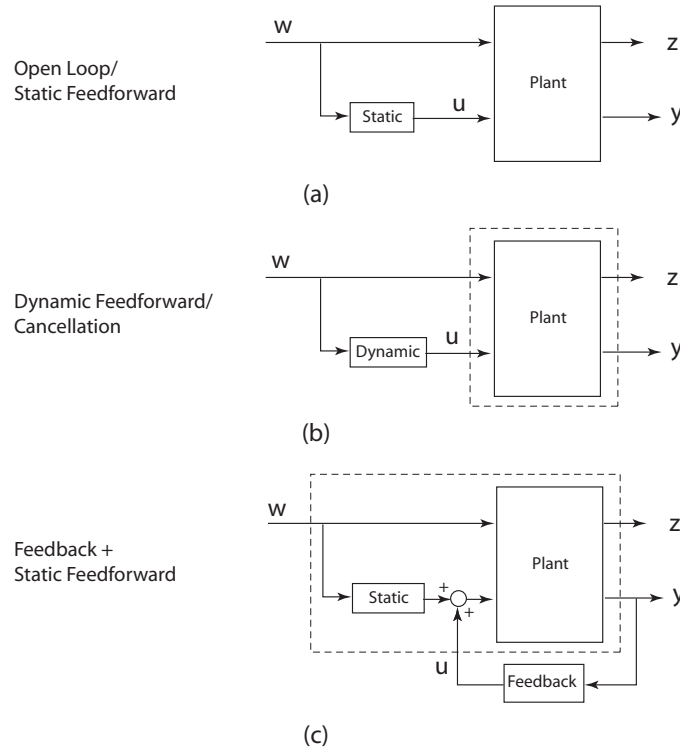
Figure 5.3: Different control configurations

    The unit step disturbance response of the system with feedforward control as compared to the system with no control is shown in Figure 5.4. The variables plotted are the deviation from nominal point $(e_{P_{net}}^d, \lambda_{O_2}^d)$ of the performance variables. Since we do not have specific requirements for the $z_2 = \lambda_{O_2}$ we search for the best possible disturbance rejection that can be achieved by a controller "w to u" that cancels the disturbance from "w to z_2" at all frequencies. This cancellation controller can be implemented as a dynamic feedforward, as shown in Figure 5.3(b). The design of the dynamic feedforward controller is presented in Section 5.4. It is based on inversion of the linear plant with the input and output around the dashed area in Figure 5.3(b).

    Both static and dynamic feedforward controllers suffer from sensitivity to modelling error, device aging, and variations in ambient conditions. This degrades the system robustness, i.e., performance under uncertainty. To improve the system robustness, feedback control is added. Figure 5.3(c) shows

the feedback control configuration. Only measurable variables, y, are fed back to the controller. The static feedforward is considered part of the plant. Thus, for the feedback control design, linearization is done for the inputs and outputs around the dashed box in Figure 5.3(c), which cover the static feedforward map. Note that static feedforward is used instead of dynamic feedforward. If dynamic feedforward is used, the linearization will give a higher order plant since there are additional dynamics contributed by the dynamic feedforward.

The simplicity of the static feedforward (open loop control) with a slow proportional integral (PI) controller is very desirable, and thus establishes the basis for comparison between the performances of different controllers in the following sections. Due to the slow PI controller, the static feedforward alone defines the closed loop system behavior. Hence the response of the system with the static feedforward (open loop control) shown in Figure 5.4 is considered as the baseline controller from now on. Note here that the overshoot in z_2 is unfavorable since redundant power is used to produce this unnecessary overshoot. Moreover, the overshoot on the O_2 excess ratio is equivalent to O_2 starvation when the system is subjected to a step down disturbance.
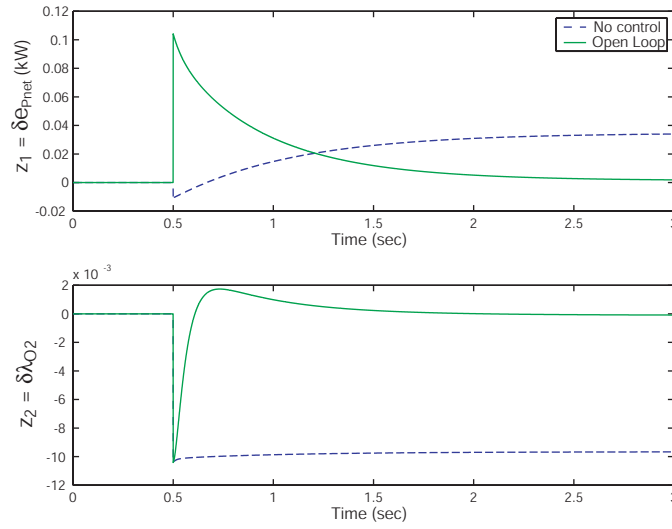
Figure 5.4: Comparison between system with no control and system with static feedforward

5.3 Linearization

The LTI system analysis in MATLAB/Simulink control system toolbox is used to linearize the non-linear system that is developed in Chapters 2 and 3. The nominal operating point is chosen where the system net power is $z_1^o = 40$ kW and oxygen excess ratio is $z_2^o = 2$. The inputs that correspond to this operating point are stack current at $w^o = 191$ A and compressor motor voltage at $u^o = f_{cm}(191) = 164$ V based on the static feedforward controller design discussed in the previous section. We denote also the nominal states at the equilibrium of the system for nominal inputs w^o and u^o. The linear model is

$$
\begin{aligned}
\delta\dot{x} &= A\delta x + B_u\delta u + B_w\delta w \\
\delta z &= C_z\delta x + D_{zu}\delta u + D_{zw}\delta w \\
\delta y &= C_y\delta x + D_{yu}\delta u + D_{yw}\delta w
\end{aligned}
\tag{5.4}
$$

where $\delta(\cdot) = (\cdot) - (\cdot)^o$ represents the variation from the nominal value. The state, x, measurements, y, performance variables, z, input, u, and disturbance, w, are

$$
x = \begin{bmatrix} m_{O_2} & m_{H_2} & m_{N_2} & \omega_{cp} & p_{sm} & m_{sm} & m_{w,an} & p_{rm} \end{bmatrix}^T
\tag{5.5}
$$

$$y = [W_{cp}, p_{sm}, v_{st}]^T$$
$$z = [e_{P_{net}}, \lambda_{O_2}]^T$$
$$u = v_{cm}$$
$$w = I_{st}$$

Here, the units of states and outputs are scaled such that each variable has a comparable magnitude. The units are as follows: mass in grams, pressure in bar, rotational speed in kRPM, mass flow rate in g/sec, power in kW, voltage in V, and current in A.

Note that the resulting linear model has eight states while the nonlinear model has nine states. The state that is removed, because it is unobservable during linearization, is the mass of water in the cathode. The reason is that, with the parameters of the membrane water flow that we used, there is always excessive water flow from anode to cathode that for all nominal conditions results in fully humidified (vapor saturated) cathode gas. Thus, for constant temperature, the vapor pressure is constant and equal to the saturated vapor pressure. Our nonlinear model does not include the effects of liquid condensation, also known as "flooding," on the FCS voltage response. As a result, the cathode water mass is not observable from the linearization point of view. On the other hand, the anode vapor pressure is observable and it is included in the linearization because variations in the FCS current affect the partial pressure of vapor in the anode that is always less than its saturated value. The change in vapor pressure affects the hydrogen partial pressure due to the fast P controller that regulates the anode pressure to be equal to the cathode pressure. The hydrogen pressure in turn affects the FCS voltage and makes the $m_{w,an}$ observable.

There are two linearization cases. The first is the regular input/output linearization of the plant shown in Figure 5.3(b) with $(A, B_u, B_w, \ldots, D_{zw})$ as in (5.4). This is used in the sequel Section for the design of the dynamic feedforward. The exact system matrices are given in Table A.1 of Appendix A.1. The second case is linearization with static feedforward $f_{cp}(w)$ in addition to feedback control u_{fb} shown in Figure 5.3(c) $u = u_{fb} + u^* = u_{fb} + f_{cp}(w)$. The exact matrices $(A, B_u, B_w^o, \ldots, D_{zw}^o)$ are given in Table A.2 in Appendix A and are used in Section 5.5 where the feedback controller is designed. As our notation indicates, the matrices of the two systems are the same, except $B_w^o = \left(\frac{\partial f}{\partial w} + \frac{\partial f}{\partial u}\frac{\partial f_{cp}}{\partial w}\right)|_{x^o,u^o,w^o} = B_w + B_u\frac{\partial f_{cp}}{\partial w}|_{w^o}$ and $D_{z_1w}^o = D_{z_1w} + D_{z_1u}\frac{\partial f_{cp}}{\partial w}|_{w^o}$ matrices. Note that D_{z_2w} is the same for both cases because $D_{z_2u} = 0$.

For both linear systems, the anode flow control (proportional) is included in the linearization. The comparison between the step responses of nonlinear and linear models is shown in Figure A.1.

5.4   Dynamic Feedforward

Let us begin the design of the dynamic feedforward controller by stating a well known fact: "*a feedforward controller cannot change the open loop system dynamics unless it cancels them.*" Due to the topology of the control variable, $u = v_{cm}$, and the disturbance, $w = I_{st}$, with respect to the performance variable, $z_2 = \lambda_{O_2}$, the disturbance rejection capabilities of the open loop system are moderate. For example, the output response of the static feedforward controller, $u = f_{cm}(I_{st})$, depends on the dynamics of the compressor inertia, supply manifold filling, and eventually, cathode manifold filling dynamics. It is clear that in order to achieve good disturbance rejection the control variable, u, needs to be a lead filter of the measured disturbance, w (see [42]). The lead filter is based on the inversion of the open loop dynamics from "u to z_2."

Using the linear model given in Table A.1, the system can be arranged in the transfer function form

$$\Delta Z_2 = G_{z2u}\Delta U + G_{z2w}\Delta W \tag{5.6}$$

where $G_{z2u} = C_{z_2}(sI - A)^{-1}B_u$ and $G_{z2w}w = C_{z_2}(sI - A)^{-1}B_w + D_{z_2w}$, and all variables in capital are in the Laplace domain. For simplicity, the Laplace variable "s" is not explicitly shown. Let a dynamic feedforward controller be $\Delta U = K_{uw}\Delta W$ as shown in Figure 5.5. The transfer function from
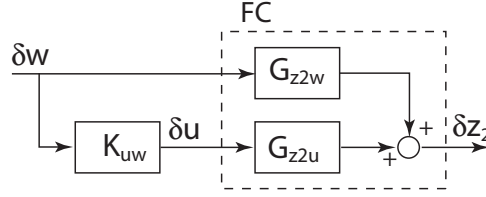
Figure 5.5: Dynamic feedforward control

W to Z_2 can be written as

$$T_{z_2 w} = \frac{\Delta Z_2(s)}{\Delta W(s)} = (G_{z2w} + G_{z2u}K_{uw}) \tag{5.7}$$

For complete disturbance rejection $T_{z_2 w} = 0$ and K_{uw}^{ideal} cancels the response of z_2 due to w:

$$K_{uw}^{ideal} = -G_{z2u}^{-1}G_{z2w}. \tag{5.8}$$

The open loop plant dynamics, G_{z2u}, is minimum phase and thus K_{uw}^{ideal} is a stable controller. Direct modification of the current disturbance or techniques from [14] and [35] are needed in the case of a delay or non-minimum phase system dynamics. The inversion of the G_{z2u} transfer function calculated in Equation (5.8) is not proper and thus is not realizable (anti-causal filter). Moreover, K_{uw}^{ideal} corresponds to large amplitude of control input at high frequencies. To obtain a strictly proper feedforward controller, high-frequency components of K_{uw}^{ideal} are removed using a low pass filter, i.e.

$$K_{uw} = -\frac{1}{(1 + \frac{s}{\alpha_1})(1 + \frac{s}{\alpha_2})(1 + \frac{s}{\alpha_3})} \cdot G_{z2u}^{-1}G_{z2w} \tag{5.9}$$

The values of α_1, α_2, and α_3 used are, 80, 120, and 120, respectively. Figure 5.6 shows a comparison between K_{uw}^{ideal} and the strictly proper K_{uw}.

The response of the linear system subjected to unit step in disturbance, w, is shown in Figure 5.7. The response of z_2 is zero except at high frequencies, i.e., at the initial transient. By increasing the value of α's, the response of z_2 can be made faster at the expense of large control action that is reflected in z_1 due to the compressor power expended.
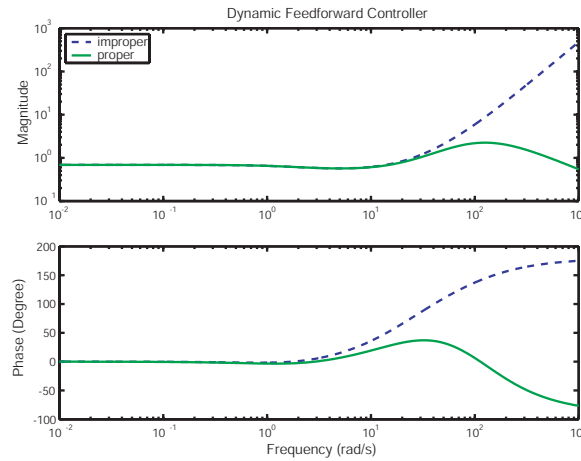
Figure 5.6: Frequency plot of dynamic feedforward controller

Even though the dynamic feedforward cancels the effect of w to z_2 at a wide range of frequencies, the model-based inversion can adversely affect the disturbance rejection capability in the presence
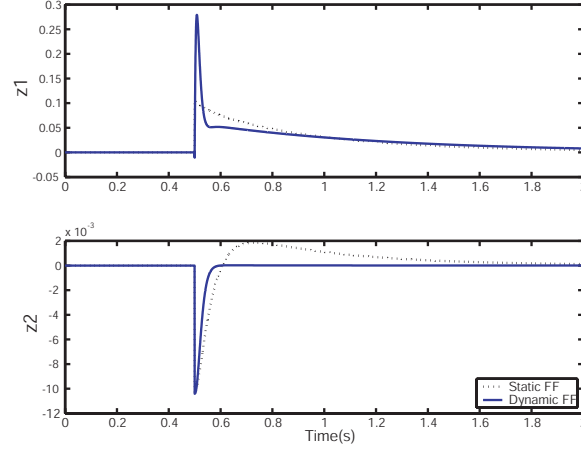
Figure 5.7: Step response of system with dynamic feedforward in linear simulation

of unknown disturbance, modelling error, and parameter variation. Because there is no feedback, the sensitivity function of the system with respect to unknown disturbance is equal to unity at all frequencies. The frequency domain modifications in [34] can be used to reduce the cancellation controller sensitivity if one can find bounds on the size of the plant uncertainties. The response of the nonlinear system with the dynamic feedforward subjected to a series of current steps (Figure 5.8), presented in Figure 5.9, shows one of the effects of modeling error, which is the steady-state error.
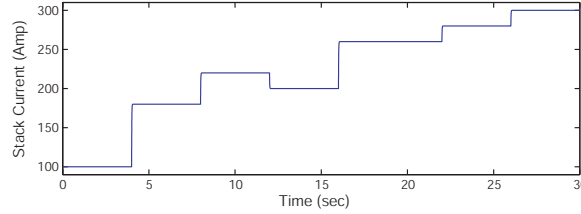
Figure 5.8: Current input used in nonlinear simulation

5.5 Feedback Control Design

Well-designed feedback controllers have advantages over feedforward control in term of robustness in the presence of unknown disturbance and plant parameter variations. For the control problem considered here, the performance objective can not be measured so there are inherent robustness limitations. The feedback controller is based on linear quadratic techniques decomposing the problem to a state feedback and an observer design using the separation principle. The linear model obtained from linearization with static feedforward (Table A.2) is used in designing the feedback controller.

5.5.1 State Feedback

Linear Quadratic Regulator (LQR) optimal control is used to design the state feedback controller. Since the control goal is to minimize the response of δz_2 without using excessive control input, the appropriate cost function is in the form

$$J = \int_0^\infty \delta z_2^T Q_z \delta z_2 + \delta u^T R \delta u \, dt \tag{5.10}$$
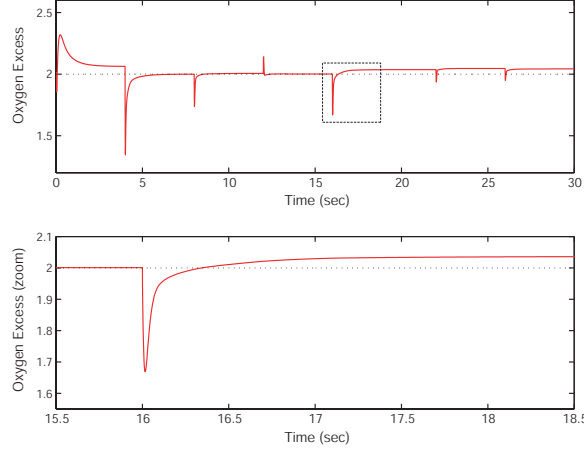
Figure 5.9: Response of system with dynamic feedforward in nonlinear simulation

However, there is a disturbance feedthrough term on the performance variables, δz_2:

$$\delta z_2 = C_{z2}\delta x + D_{z2w}\delta w \tag{5.11}$$

This prevents the proper formulation of the cost function in terms of the states and control signals, which is required in solving the LQR problem. In order to formulate as an LQR problem, we first define

$$\delta z_2' = C_{z2}\delta x \tag{5.12}$$

and use $\delta z_2'$ in the cost function as follows

$$J = \int_0^\infty \delta z_2'^T Q_z \delta z_2' + \delta u^T R \delta u \, dt = \int_0^\infty \delta x^T C_{z2}^T Q_z C_{z2}\delta x + \delta u^T R\delta u \, dt \tag{5.13}$$

Then, the optimal control that minimizes (5.10) is given by

$$\delta u = -K(\delta\hat{x} - \delta x_d), \qquad K := R^{-1}B^T\bar{P} \tag{5.14}$$

where $\bar{P}$ is the solution to the Algebraic Riccati Equation (ARE):

$$\bar{P}A + A^T\bar{P} + Q_x - \bar{P}BR^{-1}B^T\bar{P} = 0 \tag{5.15}$$

where $Q_x = C_{z2}^T Q_z C_{z2}$. The optimal control law in (5.14) assumes perfect measurements or estimation of all the states, i.e., $\delta\hat{x} = \delta x$. Variable δx_d in (5.14) is the desired value of the states, as a function of δw, that results in the desired value of $\delta z_2 = 0$ (see page 310 of [43]). The value of δx_d can be obtained by either determining the steady-state value from linear simulation or solving

$$0 = A\delta x_d + B_u\delta u_d + B_w\delta w \tag{5.16}$$
$$0 = C_{z2}\delta x_d + D_{z2w}\delta w \tag{5.17}$$

or in matrix form

$$0 = \begin{bmatrix} A & B_u \\ C_{z2} & 0 \end{bmatrix}\begin{bmatrix} \delta x_d \\ \delta u_d \end{bmatrix} + \begin{bmatrix} B_w \\ D_{z2w} \end{bmatrix}\delta w \tag{5.18}$$

Figure 5.10 shows the difference between δx_d determined from nonlinear and linear simulations. It can be seen that the discrepancy is larger at low power levels. For precise control, nonlinear maps are preferable.
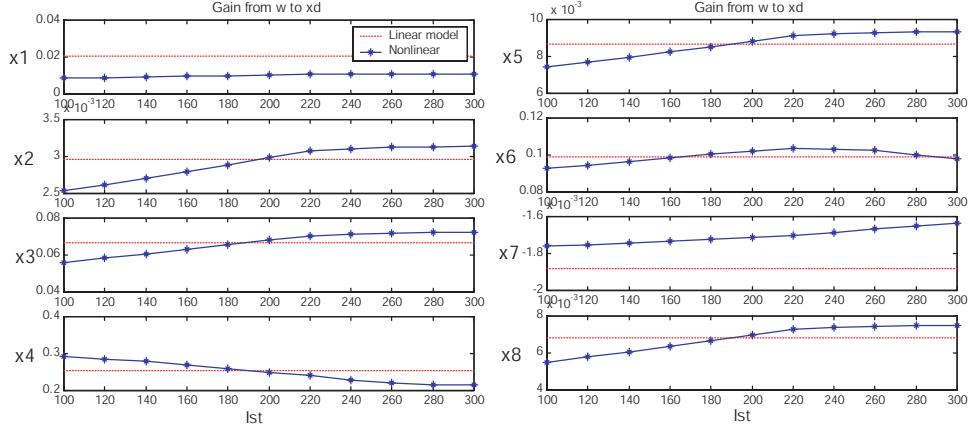
Figure 5.10: Comparison between x_d calculated from linear and nonlinear models

For simplicity, a fixed value for δx_d based on the linear plant approximations is used. The effect of the fixed δx_d is equivalent to another feedforward term, u_p, typically called a precompensator in [44], that modifies the existing feedforward term u^*:

$$u = u^* + u_p - k\delta x \tag{5.19}$$

$$u_p = \left[C_{z_2}(A - B_u K)^{-1} B_u \right]^{-1} \left[D_{z_2 w} - C_{z_2}(A - B_u K)^{-1} B_w^o \right] \delta w \tag{5.20}$$

The linear response of the system with full state feedback controller and static feedforward is shown in Figure 5.11. The response achieved with dynamic feedforward is practically identical to the one achieved with the state feedback controller so it is not shown. The response of closed loop λ_{O_2} to I_{st} is faster than the open loop with the static feedforward. After the initial excursion that cannot be avoided as long as a causal controller is implemented, the closed loop λ_{O_2} recovers to a 0.2% band of the nominal λ_{O_2} within 0.04 sec, whereas the open loop λ_{O_2} recovers within 0.075 sec. This shows that the closed loop system is approximately two times faster than the open loop system.

The closed loop transfer function from the disturbance w to the performance variables z is shown in Figure 5.12. It can be seen that both dynamic feedforward and closed loop controllers reduce the magnitude of z_2 at frequencies between 0.2 and 40 rad/sec.
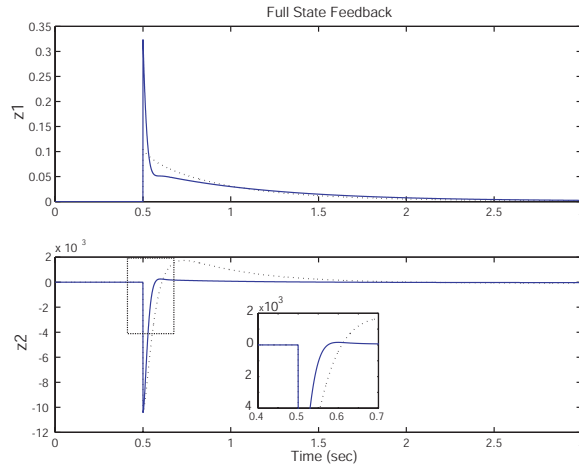
Figure 5.11: Step response of system with full state feedback in linear simulation
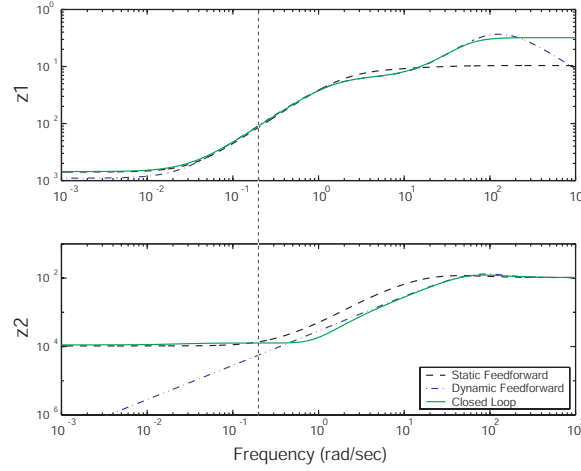
Figure 5.12: Frequency response of closed-loop system from w to z

In practice, to prevent stack starvation, the stack current signal is filtered by a low pass filter in order to allow enough time for the air supply system to increase air flow to the cathode. This solution, however, slows down the fuel cell power response because the power is a direct function of the current. Therefore, it is desirable to use the highest possible cutoff frequency in the low pass filter such that fast current can be drawn without starving the stack. As can be seen from Figure 5.12, to reduce the magnitude of the excess ratio, the current filter used for the controlled system can have higher cutoff frequency, which means that the controlled system can handle faster current drawn without starving the stack, and thus, faster power is produced from the fuel cell system.

This result is easier to see in the time domain. If a current limiter were used whenever λ_{O_2} deviates, say 0.2% of the nominal value, it would have been active for 0.075 sec for the open loop system. Whereas, in the closed loop system the current limiter becomes active for only 0.04 sec as seen in the zoom-in of the plot in Figure 5.11. Figure 5.13 shows that the improvements in the closed loop performance persist in nonlinear simulations.
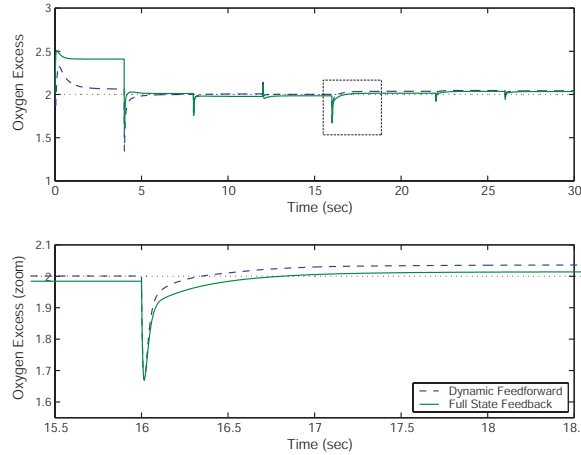
Figure 5.13: Response of system with full state feedback in nonlinear simulation

The plot of the input sensitivity function in Figure 5.14 shows the benefit of the feedback over the feedforward configuration. In a single input single output (SISO) system, the sensitivity function can be viewed as transfer function from output disturbance to tracking error. Based on this interpretation, small sensitivity corresponds to good disturbance rejection. The sensitivity function is also inversely

proportional to the distance between the loop gain, L, and the -1 point in the s-domain, $S = 1/(1 + L)$ [96]. Based on this relationship, the sensitivity function offers a measure of distance to instability. The smaller S is, the more variation in the parameters is needed to cause instability [43]. In summary, small S indicates high robustness. Figure 5.14 shows that the feedback configuration reduces system sensitivity.

Sensitivity to steady-state error is not, however, totally eliminated, as can be seen from nonlinear simulation in Figure 5.13. The error is caused mainly by the error in the desired state, x_d, which is calculated in (5.16) from the linear model. Specifically, there is a large steady-state error at low power level (at time 3 second) due to the discrepancy in x_d shown in Figure 5.10. Integral control is
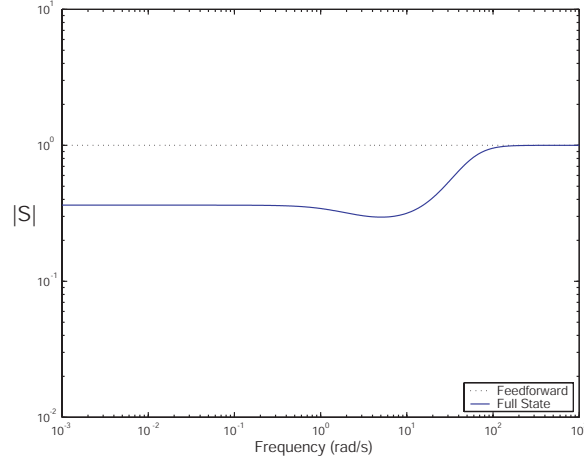
Figure 5.14: Magnitude of input sensitivity function of system with full state feedback

introduced to reduce the steady-state error. The next section discusses the design and limitations of the integral control.

5.5.2   Feedback with Integral Control

Integral control can be used together with state feedback to reduce the steady-state error of the control output. Since the performance variable, λ_{O_2}, cannot be measured, integral control must be applied to one of the available measurements. The most obvious choice is assigning an integrator on the compressor flow rate, $y_1 = W_{cp}$, for two reasons: First, it is easy to measure W_{cp}. Second, it is relatively easy to calculate the required compressor air flow rate, $W_{cp}^* = f_{cp}(I_{st})$, that satisfies the desired oxygen excess ratio. This calculation is based on electrochemical and thermodynamic calculations for known ambient conditions and is shown in detail in Appendix A.1. The state equation of the integrator is thus

$$\dot{q} = \delta W_{cp}^* - \delta W_{cp} \tag{5.21}$$

with $\delta W_{cp}^* = W_{cp}^* - W_{cp}^o$ where W_{cp}^o is the nominal compressor air flow rate as defined in the linearization section. The LQR optimal control design is used to determine the controller in the form

$$u = -K(\delta\hat{x} - \delta x_d) - K_I q \tag{5.22}$$

where K and K_I are controller gains. The gains are computed using the LQR method to minimize

$$J = \int_0^\infty \delta z_2^T Q_z \delta z_2 + q^T Q_I q + \delta u^T R \delta u \, dt \tag{5.23}$$

where Q_I is weighting on the integrator state. Since the integrator is not used on the performance variable, $\delta z_2 = \delta\lambda_{O_2}$, increasing the weighting Q_I on $q = \int(\delta W_{cp}^* - \delta W_{cp})d\tau$ causes slow performance

in term of $\delta\lambda_{O_2}$. Figure 5.15 shows that although the high integrator gain, Q_I, brings the compressor flow rate, $y_1 = W_{cp}$, to its steady-state value fast, the response of δz_2 becomes slower. This apparent tradeoff, is explained below. The fast integrator regulates (to steady-state) the compressor flow that is upstream of the supply manifold and the cathode manifold. For fast recovery of λ_{O_2}, the compressor flow, W_{cp}, needs to exhibit overshoot. Increasing the weighting Q_z helps only the initial part of the
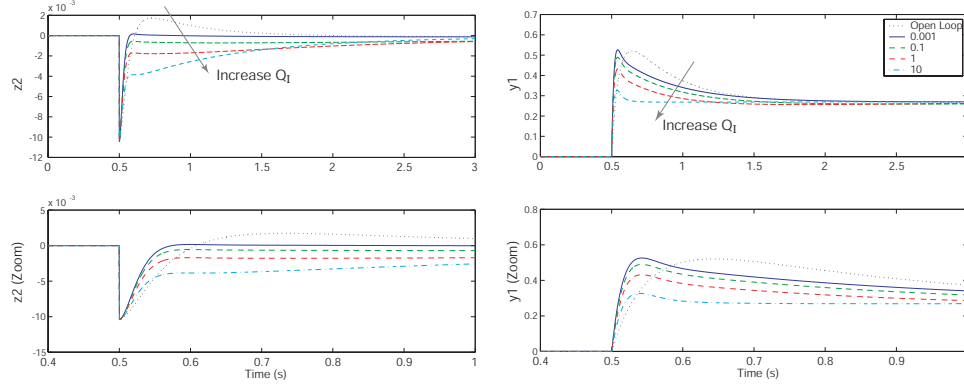
Figure 5.15: Linear step response showing effects of increasing weight on integrator

transient, as shown in Figure 5.16. As can be seen in Figure 5.15, the best z_2 response is obtained
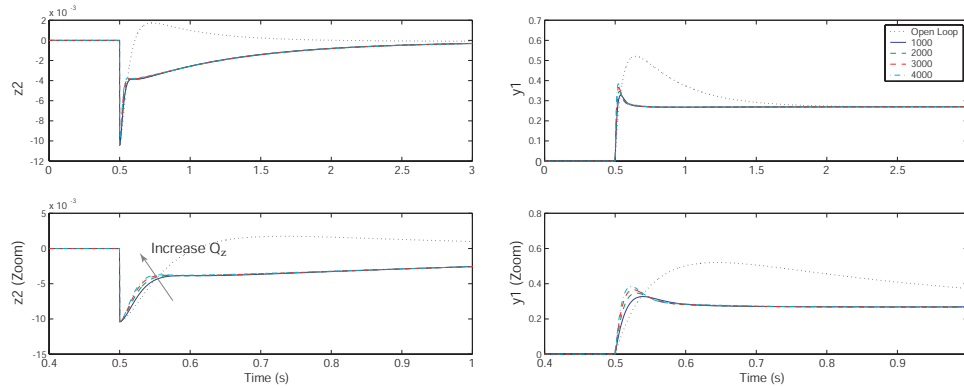
Figure 5.16: Linear step response showing effects of increasing weight on performance variables

with $Q_I = 0.001$, which gives the controller gains

$$K = \begin{bmatrix} -28.593 & -1.6\times10^{-13} & -60.571 & 7.572 & 579.74 & 2.55 & -3.6\times10^{-14} & -189.97 \end{bmatrix}$$

$$K_I = -0.18257 \tag{5.24}$$

This small integral gain can slowly bring the steady-state to zero. The step response of feedback plus integral control system is shown in Figure 5.17.

It can be observed that decreasing weighting on the integrator at low frequencies can improve the speed of z_2 response since y_1 is allowed to overshoot during the transient. The frequency shaping method discussed in [7] could be applied by adding a filter to the output and augmenting the filter state in the cost function. The downside is an increase in controller complexity due to additional dynamics contributed by the output filter. The frequency shaping technique and the selection of output filter are interesting topics for future study.

Notice also that the fundamental reason that increasing integral gain degrades the response of performance variable z_2 is because the integrator is applied to the air flow measurement y_1 far upstream
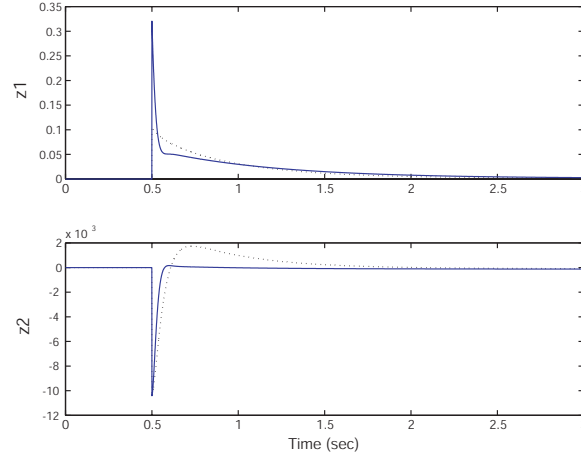
Figure 5.17: Linear step response of system with state feedback and integral control

from the position where z_2 is defined (see Figure 5.1). Thus, moving the flow measurement to the position closer to the fuel cell stack (either flow entering or exiting) seems to be more appropriate in terms of designing integral control. However, in practice, flow measurement near the stack can cause trouble due to a large variation in the humidity, pressure, and temperature of the flow [52]. Moreover, because this large change in the thermodynamic condition of the flow at this location, it is impossible to accurately calculate the required amount of air flow to be used as a reference value in the integral control.

The responses shown in this and the previous sections are based on the assumption that all system states are known $\delta\hat{x} = \delta x$. In practice, a state estimator (or observer) is needed to estimate the system states, $\delta\hat{x}$, from available measurements, y. The design of a state observer and the effects of different measurements are presented in the following section.

5.6   Observer Design

The estimate of the state, $\delta\hat{x}$, used in the calculation of the control input (Equation (5.22)) is determined using a state observer based on Kalman Filter design. Three measurements available are compressor air flow rate, $y_1 = W_{cp}$, supply manifold pressure, $y_2 = p_{sm}$, and fuel cell stack voltage, $y_3 = v_{st}$ (see Figure 5.1). These variables are relatively easy to measure. The compressor flow rate is typically measured as an internal feedback to the compressor local control. The stack voltage is normally monitored for diagnostics and fault detection procedures that shut-down the FCS by zeroing the current drawn from the FC. The observer state equations are

$$\delta\dot{\hat{x}} = A\delta\hat{x} + B_u\delta u + B_w\delta w + L(\delta y - \delta\hat{y}) \tag{5.25}$$
$$\delta\hat{y} = C_y\delta\hat{x} + D_{yu}\delta u + D_{yw}\delta w$$

Based on the Linear Quadratic Gaussian method, the optimal observer gain, L, is

$$L := SC_y^T W_y^{-1} \tag{5.26}$$

where S is the solution to

$$0 = SA^T + AS + V_x + SC_y^T W_y^{-1} C_y S \tag{5.27}$$

The positive definite matrices W_y and V_x represent the intensities of measurement noise and process disturbance, respectively [38].

Table 5.1: Eigenvalues, eigenvectors, and observability

Eigenvalues								
λ	-219.63	-89.485	-46.177	-22.404	-18.258	-2.915	-1.6473	-1.4038
Eigenvectors								
x1	1.06E-16	-0.17539	-0.091325	3.43E-16	0.050201	0.024367	0.86107	-0.25619
x2	0.29428	0.016479	0.012583	0.1289	0.0036888	0.016047	0.007579	-0.0074482
x3	-3.23E-16	-0.74707	-0.099392	-5.92E-16	0.13993	0.44336	-0.14727	-0.098068
x4	-1.21E-16	-0.12878	-0.45231	3.24E-15	-0.98678	0.62473	0.27811	-0.27037
x5	-9.58E-18	0.0479	0.067229	-5.98E-17	0.0046179	0.046501	0.022519	-0.022231
x6	-7.23E-17	0.61398	0.86233	-7.93E-16	0.057898	0.6389	0.3981	-0.92234
x7	0.95572	0.071474	0.11197	-0.99166	-0.016026	-0.0078755	-0.0026628	0.0024275
x8	-3.04E-17	0.099469	-0.12794	-2.05E-16	0.022705	0.043444	0.021407	-0.019503
measuring y1								
rank(λ_iI-A; C)	7	8	8	7	8	8	8	8
cond(λ_iI-A; C)	1.29E+16	171.17	157.79	9.52E+16	461.59	1130.3	9728.4	2449.9
measuring y1 y2								
rank(λ_iI-A; C)	7	8	8	7	8	8	8	8
cond(λ_iI-A; C)	1.32E+16	171.16	157.79	3.15E+17	461.59	1130.3	9728.4	2449.9
measuring y1 y2 y3								
rank(λ_iI-A; C)	8	8	8	8	8	8	8	8
cond(λ_iI-A; C)	226.69	154.99	143.86	943.77	402.8	938.86	1617	1886.2

First, the analysis on observability could be performed using Table 5.1, which shows the system eigenvalues, λ_i, the corresponding eigenvectors, and the corresponding rank and condition number of

$$\begin{bmatrix} \lambda_i I - A \\ C_y \end{bmatrix} \tag{5.28}$$

for three different cases: 1) measuring only y_1, 2) measuring y_1 and y_2, and 3) measuring all y_1, y_2, and y_3. The eigenvalue is unobservable if the corresponding matrix (5.28) loses rank (Section 2.4 of [63]). A large condition number of a matrix implies that the matrix is almost rank deficient. Thus, the large condition number of the matrix (5.28) indicates a weakly observable eigenvalue λ_i.

Comparing cases 1 and 2, Table 5.1 shows that adding y_2 measurement does not change the observability. This is because pressure and flow are related with only an integrator. The eigenvalues -219.63 and -22.404 are not observable with measurements y_1 and y_2. The eigenvectors associated with these eigenvalues reveal that the unobservable state is the mass of vapor in the anode, $m_{w,an}$. This agrees with the fact that the two measurements are in the air supply side and the only connection to the water in the anode is small membrane water flow. The hydrogen mass is however (more) observable through the anode flow control (which regulates anode pressure following cathode pressure). These two unobservable eigenvalues are however fast, and thus have small effect on observer performance. On the other hand, the slow eigenvalues at -1.6473 and -1.4038 can degrade observer performance because they are weakly observable, as indicated by large condition number at 9728.4 and 2449.9, respectively.

Adding the stack voltage measurement substantially improves the state observability, as can be seen from the rank and the condition number for case 3. However, the high condition number for slow eigenvalue (-1.4038) could degrade observer performance. Many design iterations confirm the degradation. As when this eigenvalue is moved, the resulting observer gain is large, and thus producing large overshoot in observer error. From the implementation view point, when combined with a controller, large observer gain can produce a compensator with undesirably high gain. To prevent high observer gain, we design a reduced order output estimator (closed-loop observer) for the observable part and an input estimator (open-loop observer) for the weakly observable part. Below, the design process for the case of three measurements is explained.

First, the system matrices are transformed to the modal canonical form $\delta x_2 = T \delta x$ [26] such that

the new system matrices are

$$A_2 = TAT^{-1} = \begin{bmatrix} \lambda_1 & & 0 \\ & \ddots & \\ 0 & & \lambda_8 \end{bmatrix} \tag{5.29}$$

$$C_2 = C_y T^{-1} \qquad B_2 = T \, [\, B_w \, B_u \,] \tag{5.30}$$

Note the special structure of matrix A_2 which has eigenvalues on the diagonal. The matrices are then partitioned into

$$\begin{bmatrix} A_{2o} & 0 \\ 0 & A_{2\bar{o}} \end{bmatrix}, \qquad \begin{bmatrix} B_{2o} \\ B_{2\bar{o}} \end{bmatrix}, \qquad \begin{bmatrix} C_{2o} & C_{2\bar{o}} \end{bmatrix} \tag{5.31}$$

where $A_{2\bar{o}} = \lambda_8 = -1.4038$. The reduced-order observer gain, L_2, is then designed for matrices A_{2o}, B_{2o}, and C_{2o}.

$$L_2 := SC_{2o}^T W_y^{-1} \tag{5.32}$$

$$0 = SA_{2o}^T + A_{2o}S + V_x + SC_{2o}^T W_y^{-1} C_{2o} S \tag{5.33}$$

The weighting matrices chosen are

$$V_x = \text{diag}[\, 0.01 \;\; 10 \;\; 10 \;\; 0.01 \;\; 10 \;\; 10 \;\; 10 \,] + \alpha \, B_{2o} B_{2o}^T \tag{5.34}$$

$$W_y = 1 \times 10^{-6} \, \text{diag} \begin{bmatrix} 10 & 100 & 1 \end{bmatrix} \tag{5.35}$$

which correspond to the process noise and to the measurement noise, respectively, in the stochastic Kalman estimator design [7]. The V_x is in the form used in the feedback loop recovery procedure [38]. Using this procedure, the full state feedback loop gain properties can be recovered by increasing the value of α. The value of α chosen in this design is 30. The reduced-order observer gain, L_2, is then transformed to the original coordinate

$$L = T^{-1} \begin{bmatrix} L_2 \\ 0 \end{bmatrix} \tag{5.36}$$

and its numerical values are shwon in Appendix A.1 (Equation (A.4)).

    Figure 5.18 shows the response of observer error, $\delta\tilde{x} = \delta x - \delta\hat{x}$, based on three measurements in linear simulation. The initial errors of all states are set at 1% of maximum deviation from nominal point. It can be seen that most of the state stabilizes within 0.4 seconds. There is one slow convergence which is caused by the weakly observable eigenvalue ($\lambda_8 = -1.4038$). Figure 5.19 shows the observer response when using one measurement, $y_1 = W_{cp}$. Large overshoot and slow convergence can be observed.
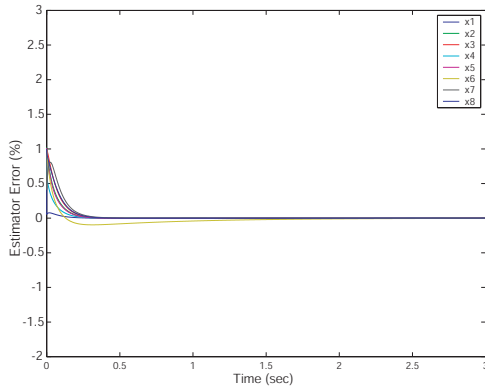
Figure 5.18: Observer state error using all measurements
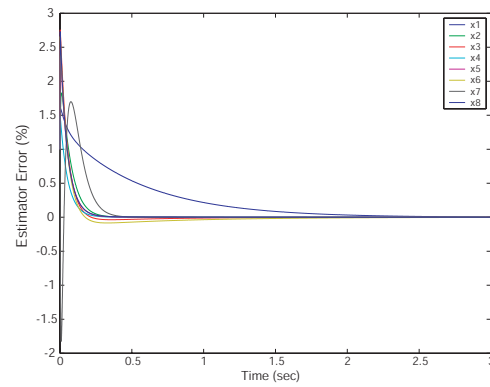
Figure 5.19: Observer state error using only the first measurement

As expected, the single measurement case results in poor system robustness as indicated by a large magnitude of sensitivity function in Figure 5.20. The loop transfer recovery method [38] could be used to bring this sensitivity closer to that of full state feedback. However, the sensitivity to errors in the initial state estimates or measurement errors increases.
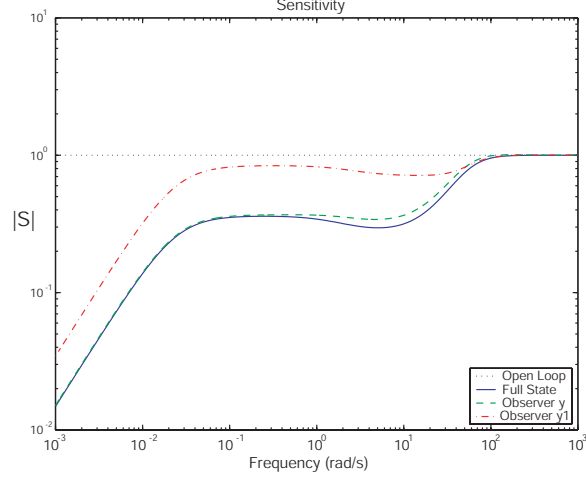
Figure 5.20: Sensitivity function for different observers

Simulations of the nonlinear system with different controllers are shown in Figure 5.21. Good transient response is achieved by both dynamic feedforward control and feedback control with three measurements. The feedback configuration is, however, superior in term of robustness. The analysis of the feedback controller performance and robustness indicates that the voltage measurement should be used as feedback to the controller and not only for safety monitoring.
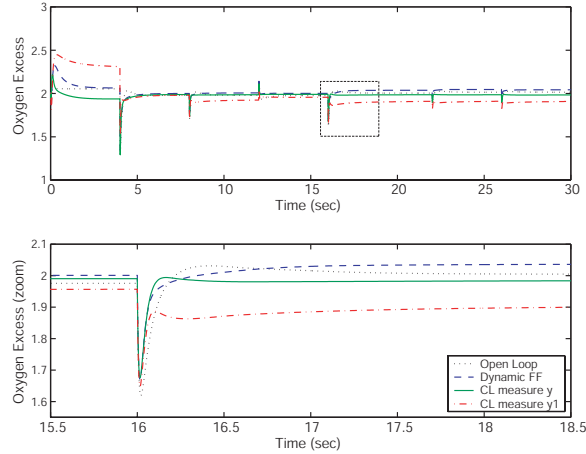
Figure 5.21: Nonlinear simulation of system with different controllers

5.7   Comparison with PI controller

As the control problem considered so far is single-input single-output (SISO) control problem where simple classical control techniques can apply, a question arises as to whether a simple PI controller with the dynamic feedforward shown in Figure 5.22 can compete with the observer-based feedback controller. A PI controller would be, after all, easier to implement and tune, thus more promising.

To this end, a PI controller is designed. A small integral gain is used that does not interfere with the transient performance of the dynamic feedforward control. The sensitivity of the dynamic feedforward to steady-state errors is reduced by the PI controller. But, the simplicity of this control configuration must be traded for system robustness (see Figure 5.23) as the control performance relies more on the feedforward path.
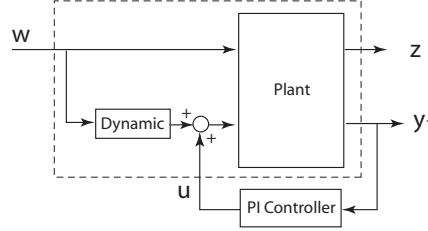
Figure 5.22: Dynamic feedforward with PI feedback
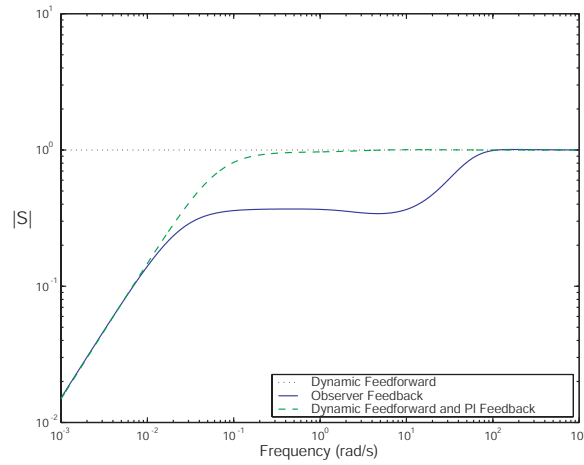
Figure 5.23: Sensitivity function comparing observer state feedback and dynamic feedforward with PI feedback

Different control configurations are considered in this chapter. The control design and discussion of the features and properties of each control design are presented. The advantages and disadvantages, such as simplicity and robustness, of each configuration are succinctly explained. Depending on the characteristics of the fuel cell system and the system model (for example, the source of unknown disturbance, the degree of parameter variations and/or model accuracy) a control engineer can select the most suitable control configuration. Because of its good performance and robustness, the observer-based feedback with the FCS voltage measurement is used from now on in this chapter.

5.8   Closed Loop Fuel Cell Impedance

The closed loop fuel cell system is comprised so far of (i) the air flow controller with the observer-based feedback described above, (ii) the simple PI anode pressure controller, and (iii) the perfect cathode humidification described in Chapter 4. Figure 5.24 shows a schematic of the closed loop configuration with emphasis on the air flow controller. The closed loop FC system is viewed as a voltage source from the power management system, as shown in Fig 5.25.

The controlled FCS (cFCS) has impedance $Z_{cFCS}(s) = V_{st}(s)/I_{st}(s)$, shown in Fig. 5.26. The plot indicates that the cFCS can be represented by a passive resistance of 0.05 Ω for current commands
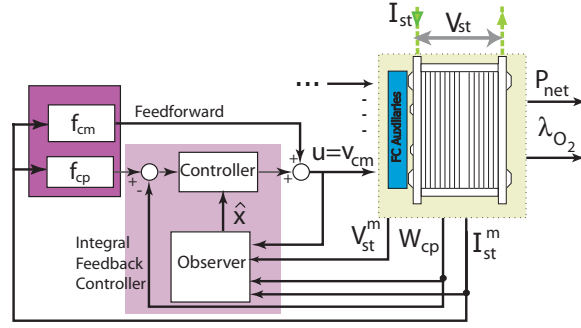
Figure 5.24: Controlled fuel cell stack as viewed from the power management system
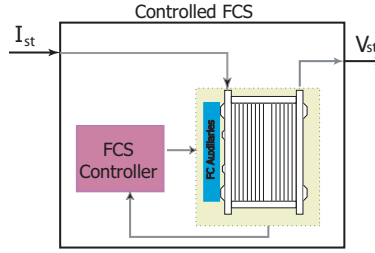
Figure 5.25: Controlled fuel cell stack modeled as impedance

slower than 0.1 rad/sec. A passive resistance of 0.3 Ω can also be used for current commands faster than 100 rad/sec. From the phase of impedance $Z_{cFCS}(s)$, one can clearly see that the voltage drops for increasing current.

A plot of current-voltage trajectories against non-controlled FCS polarization curves is shown in Figure 5.27. The controlled FCS has smaller phenomenological resistance than the non-controlled FCS. The increasing operating cathode pressure is dictated by the λ_{O_2} regulation. This phenomenon is associated with the high pressure air supply through a high speed compressor. A low pressure FCS will have similar controlled and uncontrolled impedances, primarily due to the approximately constant operating pressure. Figure 5.28 shows the compressor flow/pressure trajectories during the nonlinear simulation of Figure 5.21 plotted against the compressor map. This plot shows the actuator activity and indicates which current steps can bring the compressor close to surge or stall conditions.

5.9   Tradeoff Between Two Performance Objectives

In the case when there is no additional energy storage device such as a battery or supercapacitor, the power used to run the compressor motor needs to be taken from the fuel cell stack. A transient step change in stack current requires rapid increase in air flow to prevent depletion of cathode oxygen. This requires a large amount of power drawn by the compressor motor and thus increases parasitic loss, which affects the system net power.

The control problem that we have considered so far is the single-input single-output problem of controlling the compressor command, v_{cm}, to regulate the oxygen excess ratio λ_{O_2}. During steady-state, achieving the desired value of λ_{O_2} ensures that the desired net power is obtained. During transient, however, to produce fast λ_{O_2} responses, large v_{cm} is needed which introduces large power drawn from the fuel stack and thus a reduction of the system net power. This behavior results in a non-minimum phase property of G_{pu} in Figure 5.29. Note that $P_{net} = G_{pw} \cdot w + G_{pu} \cdot u$.

As can be seen from the step responses in Figure 5.30, I_{st} has a positive effect on the net power. On the other hand, the compressor command, v_{cm} , causes an initial drop in the net power. When
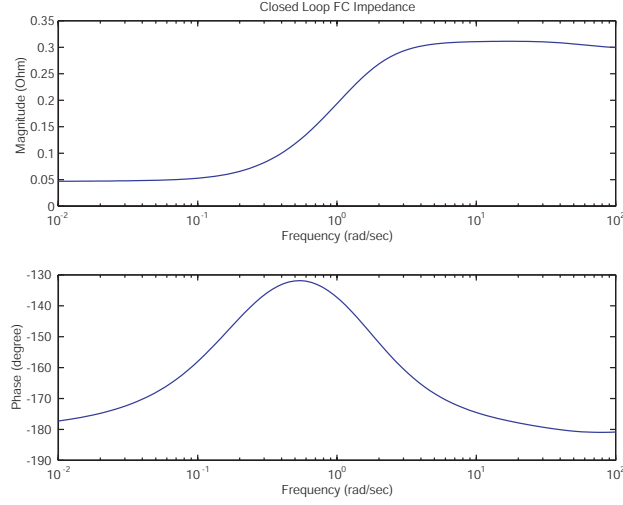
Figure 5.26: Impedance of the controlled fuel cell stack
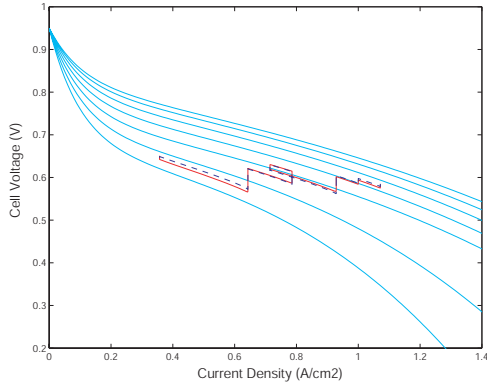
Figure 5.27: Current-voltage trajectories that correspond in the nonlinear simulation of Figure 5.21 plotted versus the open loop FCS polarization curves
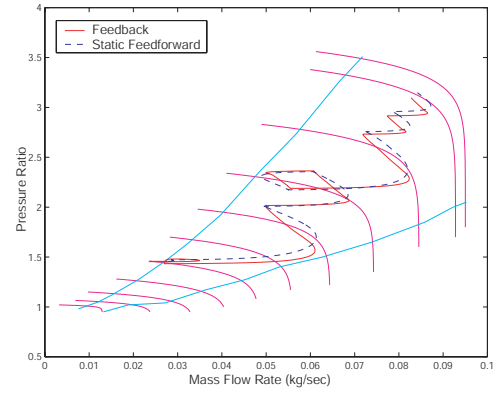
Figure 5.28: Compressor flow/pressure trajectories during the nonlinear simulation of Figure 5.21 plotted against the compressor map
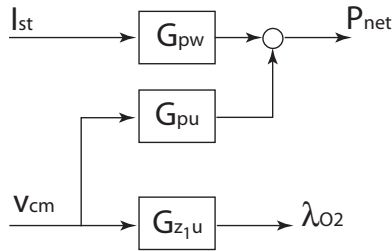
Figure 5.29: Diagram shows the effect of I_{st} and v_{cm} on P_{net}.

there is a change in I_{st}, a change in v_{cm} is always needed in order to regulate the cathode oxygen flow. We show, in Figure 5.30, the responses when v_{cm} is determined using the static feedforward controller. Figure 5.30(c) shows the P_{net} response for simultaneous step changes in both I_{st} and v_{cm}. It can be seen that the time that is needed for P_{net} to reach the desired value is approximately one second.
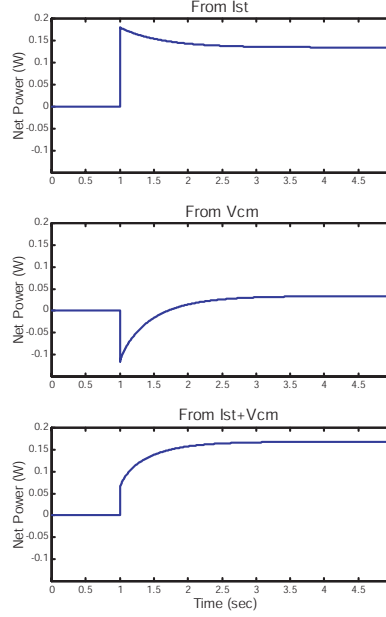
Figure 5.30: Responses of P_{net} to steps in I_{st} and v_{cm}

It is apparent that to speed up the P_{net} response, we need either larger magnitude of I_{st} (to increase stack power) or smaller value of v_{cm} (to decrease the parasitic losses). Either case will degrade the speed of λ_{O_2} response because larger I_{st} causes additional drops in λ_{O_2} while smaller v_{cm} slows down the recovery rate of λ_{O_2}. The tradeoff between P_{net} and λ_{O_2} responses cannot be eliminated because there is only one control actuator. The actuator has to compromise between the two conflicting performance variables.

We systematically explore the tradeoff by setting up the LQ control problem with the cost function in terms of z_1 $(e_{P_{net}})$, z_2 (λ_{O_2}), u (v_{cm}), and the integrator state q, i.e.,

$$J = \int_0^\infty Q_p z_1^2 + Q_\lambda z_2^2 + Ru^2 + Q_q q^2 \, dt \tag{5.37}$$

Different control gains are obtained by using different weighting in the cost function. Figure 5.31 shows responses of the linear model with the different control gain. The tradeoff between P_{net} and λ_{O_2} is evident during transient.

Figure 5.32 shows the root mean square of error during transient step response of the oxygen excess ratio λ_{O_2} and the error in the net power, $e_{P_{net}}$, for different controller gains (from different set of weighting in (5.37)). It can be easily seen the tradeoff between the two performance variables. To decide for the best compromise between the two performance objectives, we need to first establish a measure of how the low level of 5.31 affects the stack life. Without that, we present here a method to systematically determine the optimal controller that satisfies a given design objectives.

The frequency responses from the disturbance, I_{st}, to the two performance variables, $e_{P_{net}}$ and λ_{O_2}, of the closed-loop system with different controllers (Figure 5.31) are shown in Figure 5.33. It can be seen that there is severe tradeoff between the two variables in the frequency range between 0.7 rad/sec and 20 rad/sec. One option to overcome the tradeoff is to filter the current drawn from the
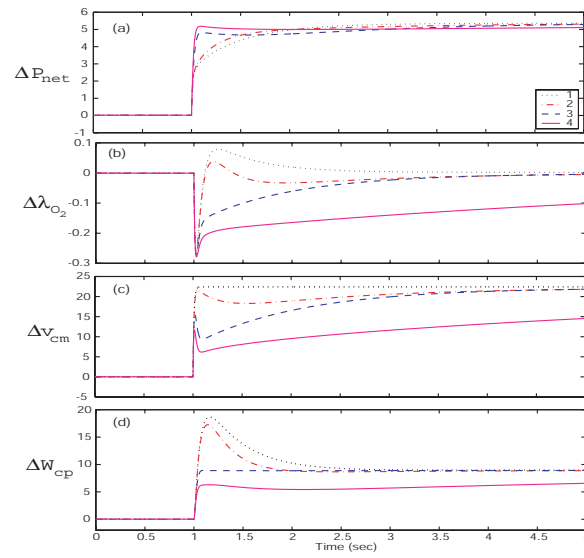
Figure 5.31: Linear system response: 1 - feedforward 2 3 4 feedback with different gains
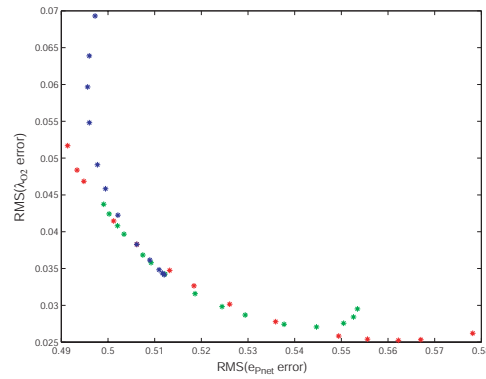
Figure 5.32: Root mean square of error in the performance variables
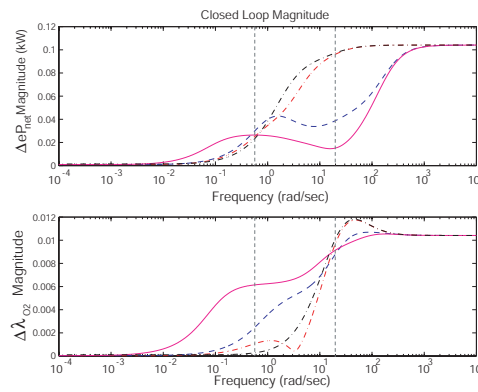
Figure 5.33: Closed-loop frequency responses for different control gains.

stack and to use an additional energy storage device (battery or ultra-capacitor) to supplement the system power during transient. Another option is to have an oxygen storage device placed near the entrance of the stack to provide an instant oxygen supply during rapid current changes. The required size of the energy or oxygen storage devices could be determined based on the frequencies associated with the tradeoff (Figures 5.12 and 5.33). The control analysis with the dynamics model of the fuel cell system provides an important tool to identify the required sizes of these storage devices. Without the analysis, it is very likely that unnecessary weight and volume are added to the fuel cell system by oversized devices.

Chapter 6

Natural Gas Fuel Processor System Model

A fuel cell system that is not fueled by pure hydrogen can use a fuel processor to convert its primary fuel into hydrogen. For residential applications, fueling the fuel cell system using natural gas is often preferred because of its wide availability and extended distribution system [36]. Common methods of converting natural gas to hydrogen include steam reforming and partial oxidation. The most common method, steam reforming, which is endothermic, is well suited for steady-state operation and can deliver a relatively high concentration of hydrogen [2], but it suffers from a poor transient operation [23]. On the other hand, the partial oxidation offers several other advantages such as compactness, rapid-startup, and responsiveness to load changes [36], but delivers lower conversion efficiency.

System level dynamic models of fuel cell power plants built from physics-based component models are extremely useful in understanding the system level interactions, implications for system performance and model-aided controller design. System level dynamic models also help in evaluating alternative system architectures in an integrated design and control paradigm. We illustrate the ideas using two control problems: 1) the coordination of fuel and air flows into the FPS for load tracking and reformer temperature control and 2) the implications of sensor selection for estimating critical FPS performance variables.

The partial oxidation-based natural gas fuel processing system (FPS) is composed of four main reactors, namely, hydro-desulfurizer (HDS), catalytic partial oxidation (CPOX), water gas shift (WGS), and preferential oxidation (PROX). Sulfur, which poisons the water gas shift catalyst [23], is first removed from the natural gas stream (mostly methane CH_4) in the HDS. Then the gas steam is mixed with atmospheric air and reacts in the CPOX to produce hydrogen-rich gas. The WGS and the PROX reactors are then used to clean up carbon monoxide that is created in the CPOX. At proper CPOX operating temperature, the amount of hydrogen created in the FPS depends on the supply rate of CH_4 and the CPOX air to fuel ratio, more specifically, the oxygen to carbon ratio. This oxygen to carbon ratio also influences the amount of heat generated in the CPOX, which then affects the CPOX catalyst bed temperature. During changes in the stack current, the fuel processor needs to quickly replenish the amount of hydrogen in the fuel cell stack (anode) while maintaining the desired temperature of the CPOX catalyst bed.

The FPS model is developed with a focus on the dynamic behaviors associated with the flows and pressure in the FPS and also the temperature of the CPOX. We assume that the distributed nature of the stack starvation and the catalyst temperature can be lumped into spatially averaged variables and can be described using ordinary differential equations. The model is parameterized and validated with the results from a high-order detailed fuel cell system model [40]. There is good agreement in most transient responses between the two models.

6.1   Fuel Processing System (FPS)
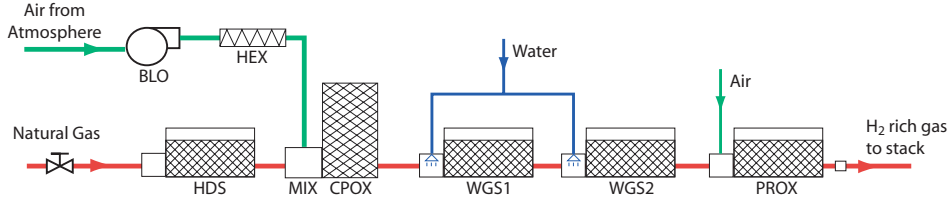
Figure 6.1: FPS components

Figure 6.1 illustrates the components in a natural gas fuel processing system (FPS) [105]. Natural gas (Methane CH_4) is supplied to the FPS from either a high-pressure tank or a high-pressure pipeline. The main air flow is supplied to the system by a blower (BLO) which draws air from the atmosphere. The air is then heated in the heat exchanger (HEX). The hydro-desulfurizer (HDS) is used to remove sulfur present in the natural gas stream [36, 49]. The de-sulfurized natural gas stream is then mixed with the heated air flow in the mixer (MIX). The mixture is then passed through the catalyst bed inside the catalytic partial oxidizer (CPOX) where CH_4 reacts with oxygen to produce H_2. There are two main chemical reactions taking place in the CPOX: partial oxidation (POX) and total oxidation (TOX) [113, 68]:

$$(POX) \qquad CH_4 + \frac{1}{2}O_2 \rightarrow CO + 2H_2 \qquad \Delta H^0_{pox} = -0.036 \times 10^6 \text{ J/mol} \tag{6.1}$$

$$(TOX) \qquad CH_4 + 2O_2 \rightarrow CO_2 + 2H_2O \quad \Delta H^0_{tox} = -0.8026 \times 10^6 \text{ J/mol} \tag{6.2}$$

Heat is released from both reactions. However, TOX reaction releases more heat than POX reaction. The difference in the rates of the two reactions depends on the selectivity, S, defined as

$$S = \frac{\text{rate of } CH_4 \text{ reacting in POX}}{\text{total rate of } CH_4 \text{ reacting}} \tag{6.3}$$

The selectivity depends strongly on the oxygen to carbon ratio (O_2 to CH_4) entering the CPOX [113]. Hydrogen is created only in POX reaction and, therefore, it is preferable to promote this reaction in the CPOX. However, the heat generated from POX reaction is not sufficient to maintain CPOX temperature. Thus, generation of TOX reaction is also required. Carbon monoxide (CO) is also created along with H_2 in the POX reaction as can be seen in (6.1). Since CO poisons the fuel cell catalyst, it is eliminated using both the water gas shift converter (WGS) and the preferential oxidizer (PROX). As illustrated in Figure 6.1, there are typically two WGS reactors operating at different temperatures [23, 71]. In the WGS, water is injected into the gas flow in order to promote a water gas shift reaction:

$$(WGS) \qquad\qquad CO + H_2O \rightarrow CO_2 + H_2 \tag{6.4}$$
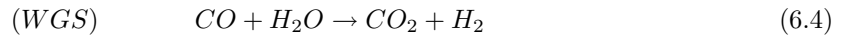
Note that even though the objective of WGS is to eliminate CO, hydrogen is also created from the WGS reaction. The level of CO in the gas stream after WGS is normally still high for fuel cell operation and thus oxygen is injected (in the form of air) into the PROX reactor to react with the remaining CO:

$$(PROX) \qquad\qquad 2CO + O_2 \rightarrow 2CO_2 \tag{6.5}$$

The amount of air injected into the PROX is typically twice the amount that is needed to maintain the stoichiometric reaction in (6.5) [23, 37].

There are two main control objectives. First, to prevent stack H_2 starvation or fuel starvation [111, 97], which can permanently damage the stack, the hydrogen flow exiting the FPS must respond fast and be robust to changes in stack power level, i.e., changes in stack current. Unfortunately, oversupply of H_2 by adjusting the FPS flow at a higher steady-state level is not an option because

this will cause wasted hydrogen from the anode exit [97]. Thus, hydrogen generation needs to follow the current load in a precise and fast manner.

Second, the temperature of the CPOX must be maintained at a certain level. Exposure to high temperature will permanently damage the CPOX catalyst bed while low CPOX temperature slows down the CH_4 reaction rate [113]. The optimization of these goals during transient operations can be achieved by coordinating the two main FPS system inputs, which are the fuel valve (natural gas valve) and the CPOX air blower command signal.

6.2 Control-Oriented FPS Model

The FPS model is developed with a focus on the dynamic behaviors associated with the flows and pressures in the FPS and also the temperature of the CPOX. The dynamic model is used to study the fuel and air flow control design that gives a reasonable tradeoff among (i) CPOX temperature regulation [113], (ii) prevention of stack H_2 starvation [97], and (iii) steady-state stack efficiency. The stack efficiency is interpreted as the H_2 utilization, which is the ratio between the hydrogen reacted in the fuel cell stack and the amount of hydrogen supplied to the stack.

Several assumptions are made in order to simplify the FPS model. Since the control of WGS and PROX reactants are not studied, the two components are lumped together as one volume and the combined volume is called WROX (WGS+PROX). It is also assumed that both components are perfectly controlled such that the desired values of the reactants are supplied to the reactors. Furthermore, because the amount of H_2 created in WGS is proportional to the amount of CO that reacts in WGS (reaction (6.4)), which in turn, is proportional to the amount of H_2 generated in CPOX (reaction (6.1)), it is assumed that the amount of H_2 generated in the WGS is always a fixed percentage of the amount of H_2 produced in the CPOX. The de-sulfurization process in the HDS is not modeled and thus the HDS is viewed as a storage volume. It is assumed that the composition of the air entering the blower is constant. Additionally, any temperature other than the CPOX temperature is assumed constant and the effect of temperature changes on the pressure dynamics is assumed negligible. The volume of CPOX is relatively small and is thus ignored. It is also assumed that the CPOX reaction is fast and reaches equilibrium before the flow exit the CPOX reactor. Finally, all gases obey the ideal gas law and all gas mixtures are perfect mixtures. Figure 6.2 illustrates the simplified system and state variables used in the model. The physical constants used throughout the model are given in Table 6.1 and the properties of the air entering the blower (approximately 40% relative humidity) are given in Table 6.2 .
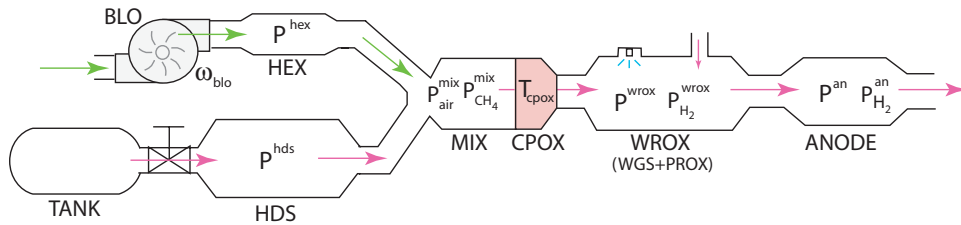
Figure 6.2: FPS dynamic model

The dynamic states in the model, shown also in Figure 6.2, are blower speed, ω_{blo}, heat exchanger pressure, p^{hex}, HDS pressure, p^{hds}, mixer CH_4 partial pressure, $p_{CH_4}^{mix}$, mixer air partial pressure, p_{air}^{mix}, CPOX temperature, T_{cpox}, WROX (combined WGS and PROX) volume pressure, p^{wrox}, WROX hydrogen partial pressure, $p_{H_2}^{wrox}$, anode pressure, p^{an}, and anode hydrogen partial pressure, $p_{H_2}^{an}$. Mass conservation with the ideal gas law through the isothermic assumption is used to model the filling dynamics of the gas in all volumes considered in the system. The orifice equation with a turbulent flow assumption is used to calculate flow rates between two volumes. The energy conservation principle is used to model the changes in CPOX temperature. The conversion of the gases in CPOX is based on

the reactions in (6.1) and (6.2) and the selectivity defined in (6.3).

6.3   Orifice

The orifice flow equation is used throughout the model to calculate the mass flow rate between two volumes as a function of upstream pressure, p_1, and downstream pressure, p_2. The flow is assumed turbulent and the rate is governed by

$$W = W_0 \sqrt{\frac{p_1 - p_2}{\Delta p_0}} \tag{6.6}$$

where W_0 and Δp_0 are the nominal air flow rate and the nominal pressure drop of the orifice, respectively.

6.4   Blower (BLO)

The speed of the blower is modeled as a first-order dynamic system with time constant τ_b. The governing equation is

$$\frac{d\omega_{blo}}{dt} = \frac{1}{\tau_b}\left(\frac{u_{blo}}{100}\omega_0 - \omega_{blo}\right) \tag{6.7}$$

where u_{blo} is the blower command signal (range between 0 and 100) and ω_0 is the nominal blower speed (3600rpm). The gas flow rate through the blower, W_{blo}, is determined using the blower map, which represents the relation between a scaled blower volumetric flow rate and a scaled pressure head [21]. The scaled pressure head is the actual pressure head scaled by a square of the speed ratio, i.e.

$$[\text{scaled pressure head}] = [\text{actual head}]\left(\frac{\omega}{\omega_0}\right)^2 \tag{6.8}$$

and the scaled volumetric flow rate is the actual flow rate scaled by the reciprocal of the speed ratio, i.e.,

$$[\text{scaled flow}] = \frac{[\text{actual flow}]}{\left(\frac{\omega}{\omega_0}\right)} \tag{6.9}$$

Note that the changes in gas density are ignored and thus only the blower speed is used in the scaling. The blower mass flow rate, W_{blo}, is calculated by multiplying the volumetric flow rate with constant air density (1.13 kg/m^3). The blower map is shown in Figure 6.3 and the blower time constant is 0.3 seconds.

Table 6.1: Physical constants

Parameter	Value
R	8.3145 J/mol·K
M_{N_2}	28×10^{-3} kg/mol
M_{CH_4}	16×10^{-3} kg/mol
M_{CO}	28×10^{-3} kg/mol
M_{CO_2}	44×10^{-3} kg/mol
M_{H_2}	2×10^{-3} kg/mol
M_{H_2O}	18×10^{-3} kg/mol
M_{O_2}	32×10^{-3} kg/mol
F	96485 Coulombs

Table 6.2: Conditions of the atmospheric air entering the blower

Parameter	Value
p_{amb}	1×10^5 Pa
$y_{N_2}^{atm}$	0.6873
$y_{H_2O}^{atm}$	0.13
$y_{O_2}^{atm}$	0.1827
M_{air}^{atm}	27.4×10^{-3} kg/mol
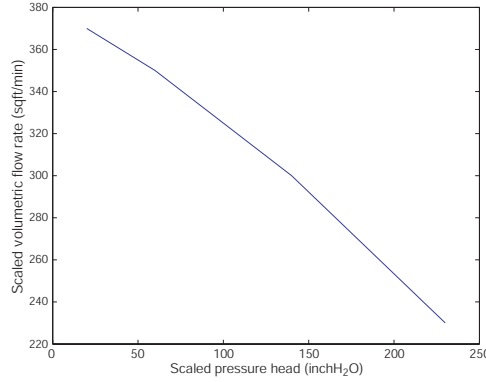
Figure 6.3: Blower map

6.5 Heat Exchanger Volume (HEX)

The only dynamics considered in the heat exchanger is the pressure dynamics. The changes in temperature of the gas are ignored and it is assumed that the effects of actual temperature changes on the pressure dynamics are negligible. The rate of change in air pressure of the HEX is described by

$$\frac{dp^{hex}}{dt} = \frac{RT_{hex}}{M_{air}^{atm}V_{hex}}(W^{blo} - W^{hex}) \tag{6.10}$$

where M_{air}^{atm} is the molecular weight of the air flow through the blower (given in Table 6.2). The orifice flow equation (Equation (6.6)) is used to calculate the outlet flow rate of the HEX, W^{hex}, as a function of HEX pressure, p^{hex}, and mixer pressure, p^{mix}.

6.6 Hydro-Desulfurizer Volume (HDS)

The pressure of the gas in the HDS is governed by the mass balance principle. It is assumed that the natural gas fed to the HDS is pure methane (CH_4) [23], and thus the desulfurization process is not modeled. The HDS is then considered as a gas volume and the pressure changes are modeled by

$$\frac{dp^{hds}}{dt} = \frac{RT_{hds}}{M_{CH_4}V_{hds}}(W_{fuel} - W^{hds}) \tag{6.11}$$

where W^{hds} is the rate of mass flow from HDS to the mixer (MIX), and is calculated as a function of p^{hds} and p^{mix} using the orifice equation (6.6). The temperature of the gas, T_{hds}, is assumed constant.

The flow rate of methane into the HDS, W_{fuel}, is controlled by a fuel valve. The orifice equation (6.6) with variable gain based on the valve input signal, u_{valve} (0 to 100), is used to model the flow through the valve.

$$W_{fuel} = \left(\frac{u_{valve}}{100}\right) W_{0,valve}\sqrt{\frac{p^{tank} - p^{hds}}{\Delta p_{0,valve}}} \tag{6.12}$$

where p^{tank} is the fuel tank or supply line pressure.

6.7 Mixer (MIX)

The natural gas flow from the HDS, W^{hds}, and the air flow from the blower, W^{hex}, are combined in the mixer (MIX). Two dynamic variables in the mixer model are the methane pressure, $p_{CH_4}^{mix}$, and the air pressure, p_{air}^{mix}. The state equations of the MIX model are

$$\frac{dp_{CH_4}^{mix}}{dt} = \frac{RT_{mix}}{M_{CH_4} V_{mix}} (W^{hds} - x_{CH_4}^{mix} W^{cpox}) \tag{6.13}$$

$$\frac{dp_{air}^{mix}}{dt} = \frac{RT_{mix}}{M_{air}^{atm} V_{mix}} (W^{hex} - x_{air}^{mix} W^{cpox}) \tag{6.14}$$

where W^{cpox} is the flow rate through the CPOX which is calculated in Section 6.8. The mixer total pressure is the sum of the CH$_4$ and the air pressures, $p^{mix} = p_{CH_4}^{mix} + p_{air}^{mix}$. Based on $p_{CH_4}^{mix}$ and p_{air}^{mix}, the mass fractions of CH$_4$ and the air in the mixer, $x_{CH_4}^{mix}$ and x_{air}^{mix}, are calculated by

$$x_{CH_4}^{mix} = \frac{1}{1 + \dfrac{M_{air}^{atm}}{M_{CH_4}} \dfrac{p_{air}^{mix}}{p_{CH_4}^{mix}}} \tag{6.15}$$

$$x_{air}^{mix} = \frac{1}{1 + \dfrac{M_{CH_4}}{M_{air}^{atm}} \dfrac{p_{CH_4}^{mix}}{p_{air}^{mix}}} \tag{6.16}$$

where M_{CH_4} and M_{air}^{atm} are the molar masses of methane and atmospheric air, respectively (see Table 6.2). Note that $x_{CH_4}^{mix} + x_{air}^{mix} = 1$ since the gas in MIX volume is composed of methane and atmospheric air. The temperature of the mixer gas, T_{mix}, is assumed constant.

The mass fractions of nitrogen, oxygen and vapor in the mixer needed for the calculation of the CPOX reactions are calculated by

$$x_{N_2}^{mix} = x_{N_2}^{atm} x_{air}^{mix} \tag{6.17}$$

$$x_{O_2}^{mix} = x_{O_2}^{atm} x_{air}^{mix} \tag{6.18}$$

$$x_{H_2O}^{mix} = x_{H_2O}^{atm} x_{air}^{mix} \tag{6.19}$$

where x_i^{atm} is the mass fraction of species i in atmospheric air, which is calculated from the mass fractions given in Table 6.2. Note that $x_{N_2}^{mix} + x_{O_2}^{mix} + x_{H_2O}^{mix} = x_{air}^{mix}$. The oxygen to carbon, i.e., O$_2$ to CH$_4$, (mole) ratio, λ_{O2C}, which influences the reaction rate in the CPOX, is calculated by

$$\lambda_{O2C} \equiv \frac{n_{O_2}}{n_{CH_4}} = y_{O_2}^{atm} \frac{p_{air}^{mix}}{p_{CH_4}^{mix}} \tag{6.20}$$

where n_i is the number of moles of species i, and $y_{O_2}^{atm}$ is the oxygen mole fraction of the atmospheric air.
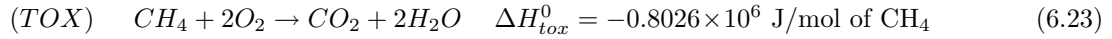
6.8 Catalytic Partial Oxidizer (CPOX)

Since the gas volume in the CPOX catalyst bed is relatively small, the pressure dynamics of the gas is ignored. The flow rate though the CPOX, W^{cpox}, is calculated using the orifice equation (6.6) as a function of mixer total pressure, p^{mix}, and the total pressure in WGS and PROX combined

volume, p^{wrox}. The only dynamics considered in the CPOX is the catalyst temperature, T_{cpox}. The temperature dynamics is modeled using energy balance equation

$$m_{bed}^{cpox} C_{P,bed}^{cpox} \frac{dT_{cpox}}{dt} = \begin{bmatrix} \text{inlet enthalpy} \\ \text{flow} \end{bmatrix} - \begin{bmatrix} \text{outlet enthalpy} \\ \text{flow} \end{bmatrix} + \begin{bmatrix} \text{heat from} \\ \text{reactions} \end{bmatrix} \qquad (6.21)$$

where m_{bed}^{cpox} (kg) and $C_{P,bed}^{cpox}$ (J/kg·K) are mass and specific heat capacity of the catalyst bed, respectively. The last two terms on the right hand side of (6.21) depend on the reaction taking place in the CPOX.

In the catalytic partial oxidation reactor, methane CH_4 is oxidized to produce hydrogen. There are two CH_4 oxidation reactions: partial oxidation (POX) and total oxidation (TOX).

$$(POX) \quad CH_4 + \frac{1}{2}O_2 \to CO + 2H_2 \quad \Delta H_{pox}^0 = -0.036 \times 10^6 \text{ J/mol of } CH_4 \qquad (6.22)$$

$$(TOX) \quad CH_4 + 2O_2 \to CO_2 + 2H_2O \quad \Delta H_{tox}^0 = -0.8026 \times 10^6 \text{ J/mol of } CH_4 \qquad (6.23)$$
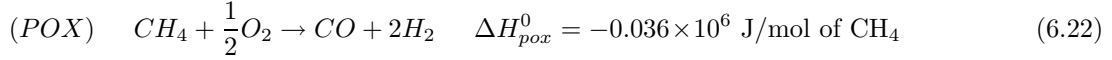
The other two secondary reactions considered here are water formation, or hydrogen oxidation (HOX), and carbon monoxide preferential oxidation (COX).

$$(HOX) \quad 2H_2 + O_2 \to 2H_2O \quad \Delta H_{hox}^0 = -0.4836 \times 10^6 \text{ J/mol of } O_2 \qquad (6.24)$$

$$(COX) \quad 2CO + O_2 \to 2CO_2 \quad \Delta H_{cox}^0 = -0.566 \times 10^6 \text{ J/mol of } O_2 \qquad (6.25)$$
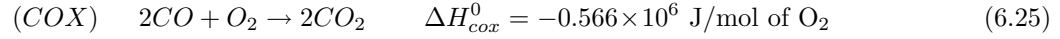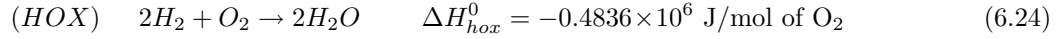
The species entering the CPOX include CH_4, O_2, H_2O, and N_2. Nitrogen does not react in the CPOX. The water may react with CH_4 through steam reforming reaction; however, this reaction is ignored in this study. Methane reacts with oxygen to create the final product, which contains H_2, H_2O, CO, CO_2, CH_4, and O_2 [113]. The amount of each species depends on the initial oxygen to carbon (O_2 to CH_4) ratio, λ_{O2C}, of the reactants and the temperature of the CPOX catalyst bed, T_{cpox}.

All reactions in the CPOX occur simultaneously. However, to simplify the model, we view the overall CPOX reaction as a consecutive process of reactions (6.22) to (6.25), as illustrated in Figure 6.4. The notations in the figure are: r = "react", nr = "not react" and f = "from". Following the diagram,
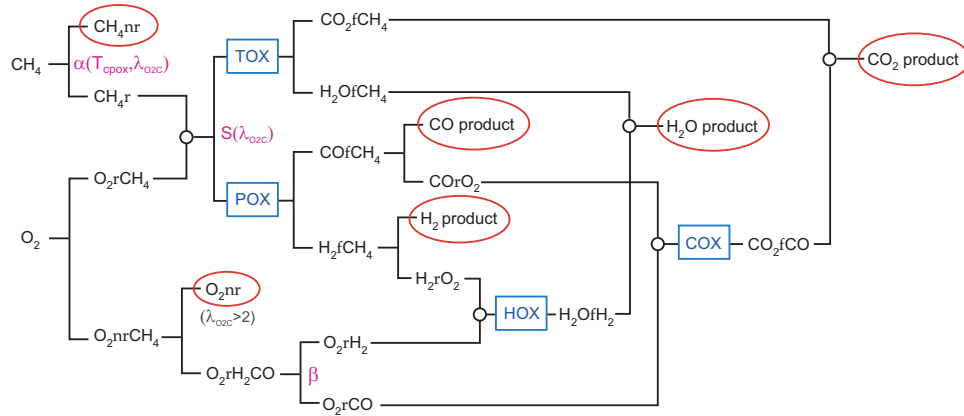
Figure 6.4: Illustration of calculation of CPOX reactions

first, consider the CH_4 and O_2 that enter the CPOX. The amount of CH_4 that reacts is a function of both O2C ratio and CPOX temperature. The relation is determined from the thermodynamic equilibrium analysis that was presented in [113]. Here, the relation is modeled using the variable α, defined as

$$\alpha := \frac{\text{rate of } CH_4 \text{ reacts}}{\text{rate of } CH_4 \text{ enters}} := \frac{N_{CH_4 r}}{N_{CH_4 in}} \qquad (6.26)$$

The expression of α is developed by curve fitting the result in [113].

$$\alpha = \begin{cases} \alpha_1 \lambda_{O2C} & \lambda_{O2C} < 0.5 \\ 1 - (1 - 0.5\alpha_1)(1 - \tanh(\alpha_2(\lambda_{O2C} - 0.5))) & \lambda_{O2C} \geq 0.5 \end{cases} \qquad (6.27)$$

where

$$\alpha_1 = \min\left(2\,,\, 0.0029T_{cpox} - 1.185\right) \tag{6.28}$$

$$\alpha_2 = 0.215e^{3.9\times10^{-8}(T_{cpox}-600)^3} \tag{6.29}$$

For illustration purposes, Figure 6.5 shows a plot of $(1-\alpha)$, which represents the amount of CH_4 that does not react, as a function of λ_{O2C} and temperature, T_{cpox}. For λ_{O2C} less than half, the oxygen supplied is not enough to react with all the CH_4 and thus there is un-reacted CH_4 left regardless of the CPOX temperature. For λ_{O2C} more than 0.5, all CH_4 reacts for CPOX temperature over 1073 K. For lower temperature, not all CH_4 reacts, which means that part of the fuel is wasted. Note that the curve fitting does not fit well for lower temperature ($T_{cpox} < 700$ K) when compared with the results in [113]. However, as will be seen in Section 6.11, the FPS model is operated at CPOX temperature around 900 K - 1000 K where the model fits very well.
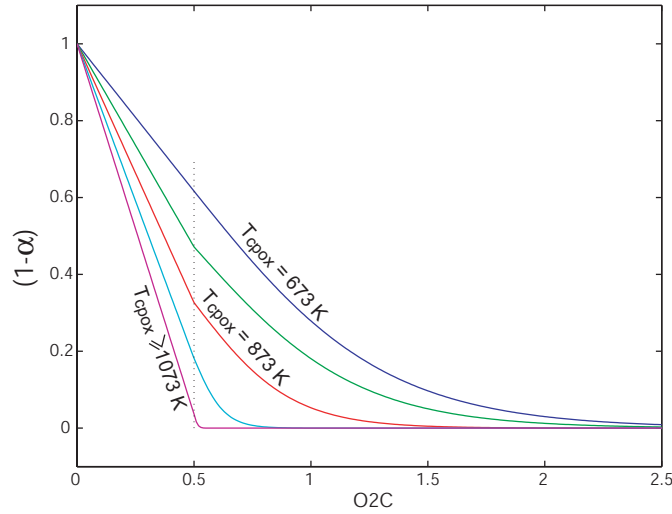
Figure 6.5: Amount of un-react CH_4 that leaves the CPOX

The amount of CH_4 reacts in POX or TOX reactions depends on the initial O2C ratio, which, in this model, is the O2C ratio in the MIX. The difference between the rate of POX and TOX reaction is described by the selectivity, S, defined in (6.3),

$$S := \frac{N_{CH_4rPOX}}{N_{CH_4r}} \tag{6.30}$$

which is a function of λ_{O2C}. Here we assume that the function is linear, as shown in Figure 6.6, which agrees with the results from the high-temperature thermodynamic equilibrium in [113]. The relation between the selectivity and the oxygen to carbon ratio in Figure 6.6 can be expressed as

$$S = \begin{cases} 1 & ,\lambda_{O2C} < \frac{1}{2} \\ \frac{2}{3}(2 - \lambda_{O2C}) & ,\frac{1}{2} \le \lambda_{O2C} \le 2 \\ 0 & ,\lambda_{O2C} > 2 \end{cases} \tag{6.31}$$

Values of S close to one indicate that more POX reaction takes place and thus more hydrogen is generated. The products from CH_4 oxidation (POX and TOX) are H_2, CO, H_2O, and CO_2, denoted in Figure 6.4 as H_2fCH_4, $COfCH_4$, H_2OfCH_4 and CO_2fCH_4, respectively.

As explained earlier, when $\lambda_{O2C} < \frac{1}{2}$, the supplied oxygen is not sufficient to oxidize all supplied fuel and the hydrogen production rate is limited by the amount of oxygen. At normal operation, λ_{O2C} is kept higher than $\frac{1}{2}$ in order to avoid wasting the fuel. A high value of λ_{O2C} (low S) indicates that
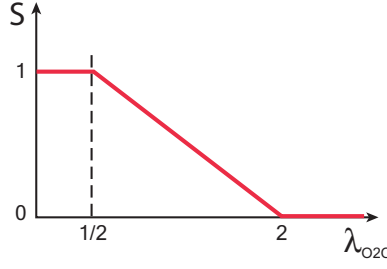
Figure 6.6: Selectivity between POX and TOX

there is more TOX reaction. Since more heat is released from TOX reaction, operating CPOX at high λ_{O2C} will overheat the CPOX and can permanently damage the catalyst bed. The desired value of λ_{O2C} in the literature varies from 0.4 to 0.6 [25, 89, 92]. In this study, the desired value is chosen at $\lambda_{O2C} = 0.6$ in order to allow some buffer for λ_{O2C} before it becomes lower than $\frac{1}{2}$ during transient deviations.

The amount of O_2 that does not react (nr) with CH_4 (O_2nrCH_4), reacts with H_2 and CO, created in the POX reaction, to form H_2O (HOX reaction) and CO_2 (COX reaction), respectively. If there is no H_2 and CO generated (no POX reaction), there will be un-reacted O_2 (O_2nr), which then leaves the CPOX. This corresponds to the situation where $\lambda_{O2C} \geq 2$. If $\lambda_{O2C} < 2$, all O_2 that does not react with CH_4 will react with H_2 and CO (O_2rH_2CO). In this model, the rate of HOX and COX reactions are described by the variable β, defined as

$$\beta := \frac{\text{rate of O}_2 \text{ reacts with H}_2}{\text{rate of O}_2 \text{ reacts with both H}_2 \text{ and CO}} := \frac{N_{O_2rH_2}}{N_{O_2rH_2CO}} \tag{6.32}$$

Since, in POX, two moles of H_2 are created for every mole of CO created, the concentration of H_2 is twice that of CO. Therefore, we use the ratio $\beta = \frac{2}{3}$. The water product of HOX reaction, denoted as H_2OfH_2 (water from H_2) is then added to the water that is produced in the TOX reaction. Similarly, the final product of CO_2 is the sum of CO_2 from TOX reaction (CO_2fCH_4) and CO_2 from COX reaction (CO_2fCO). The final products of H_2 and CO are the amount produced in POX reaction (H_2fCH_4 and $COfCH_4$) less the amount that reacts with O_2 (H_2rO_2 and $COrO_2$), which can be easily calculated using stoichiometry of HOX and COX reactions.

The calculation of the species in the CPOX model is calculated in mole basis. The molar flow rate of the gas entering the CPOX can be calculated from

$$N_{i,in} = \frac{x_i^{mix} W_{cpox}}{M_i} \tag{6.33}$$

where i represents CH_4, O_2, N_2, and H_2O; M_i is the molecular mass of gas i; and W_{cpox} and x_i^{mix} are the CPOX total flow rate and mole fraction of gas i in MIX, both are calculated in the MIX model. From the definition of α, the rate at which CH_4 reacts is

$$N_{CH_4r} = \alpha N_{CH_4in} \tag{6.34}$$

and the rate at which O_2 reacts with CH_4

$$N_{O_2rCH_4} = (2 - \frac{3}{2}S)N_{CH_4r} = (2 - \frac{3}{2}S)\alpha N_{CH_4in} \tag{6.35}$$

Thus, the rate of O_2 not reacting with CH_4 is

$$N_{O_2nrCH_4} = N_{O_2in} - (2 - \frac{3}{2}S)\alpha N_{CH_4in} = (\lambda_{O2C} - (2 - \frac{3}{2}S)\alpha)N_{CH_4in} \tag{6.36}$$

If there is POX reaction ($S \neq 0$), the oxygen that does not react with CH_4 will either react with H_2 or CO. If there is no POX reaction ($S = 0$), the oxygen will not react. The amount of O_2 that reacts either with H_2 or CO ($N_{O_2 r H_2 CO}$) and the amount of un-reacted O_2 ($N_{O_2 nr}$) are

$$N_{O_2 r H_2 CO} = N_{O_2 nr CH_4} \text{sign}(S) = (\lambda_{o2c} - (2 - \frac{3}{2}S)\alpha)\text{sign}(S)N_{CH_4 in} \tag{6.37}$$

$$N_{O_2 nr} = N_{O_2 nr CH_4}(1 - \text{sign}(S)) = (\lambda_{o2c} - (2 - \frac{3}{2}S)\alpha)(1 - \text{sign}(S))N_{CH_4 in} \tag{6.38}$$

The product of H_2, CO, CO_2, and H_2O from POX and TOX reactions can be calculated from

$$N_{H_2 f CH_4} = 2S \cdot N_{CH_4 r} = 2S \cdot \alpha N_{CH_4 in} \tag{6.39}$$

$$N_{CO f CH_4} = S \cdot N_{CH_4 r} = S \cdot \alpha N_{CH_4 in} \tag{6.40}$$

$$N_{CO_2 f CH_4} = (1 - S) \cdot N_{CH_4 r} = (1 - S) \cdot \alpha N_{CH_4 in} \tag{6.41}$$

$$N_{H_2 O f CH_4} = 2(1 - S) \cdot N_{CH_4 r} = 2(1 - S) \cdot \alpha N_{CH_4 in} \tag{6.42}$$

The rate of H_2 and CO reacted and the rate of H_2O and CO_2 created in HOX and COX reactions are

$$N_{H_2 r O_2} = 2\beta \cdot N_{O_2 r H_2 CO} \tag{6.43}$$

$$N_{CO r O_2} = 2(1 - \beta) \cdot N_{O_2 r H_2 CO} \tag{6.44}$$

$$N_{CO_2 f CO} = 2(1 - \beta) \cdot N_{O_2 r H_2 CO} \tag{6.45}$$

$$N_{H_2 O f H_2} = 2\beta \cdot N_{O_2 r H_2 CO} \tag{6.46}$$

Combining Equations (6.37), (6.42), and (6.46), a set of equations to calculate the total product of CPOX reaction can be written as

$$N_{H_2} = N_{H_2 f CH_4} - N_{H_2 r O_2}$$
$$= \left[2S\alpha - 2\beta(\lambda_{o2c} - (2 - \frac{3}{2}S)\alpha)\text{sign}(S) \right] N_{CH_4 in} \tag{6.47a}$$

$$N_{CO} = N_{CO f CH_4} - N_{CO r O_2}$$
$$= \left[S\alpha - 2(1 - \beta)(\lambda_{o2c} - (2 - \frac{3}{2}S)\alpha)\text{sign}(S) \right] N_{CH_4 in} \tag{6.47b}$$

$$N_{CO_2} = N_{CO_2 f CH_4} + N_{CO_2 f CO}$$
$$= \left[(1 - S)\alpha + 2(1 - \beta)(\lambda_{o2c} - (2 - \frac{3}{2}S)\alpha)\text{sign}(S) \right] N_{CH_4 in} \tag{6.47c}$$

$$N_{H_2 O} = N_{H_2 O f CH_4} + N_{H_2 O f H_2} + N_{H_2 O in}$$
$$= \left[2(1 - S)\alpha + 2\beta(\lambda_{o2c} - (2 - \frac{3}{2}S)\alpha)\text{sign}(S) \right] N_{CH_4 in} + N_{H_2 O in} \tag{6.47d}$$

$$N_{CH_4} = (1 - \alpha)N_{CH_4 in} \tag{6.47e}$$

$$N_{O_2} = N_{O_2 in} - N_{O_2 r} = \left(N_{O_2 in} - (2 - \frac{3}{2}S)\alpha N_{CH_4 in} \right)\text{sign}(S) \tag{6.47f}$$

$$N_{N_2} = N_{N_2 in} \tag{6.47g}$$

A plot of products calculated from Equations (6.47), assuming no inlet N_2 and H_2O, is shown in Figure 6.7, which matches with the theoretical results in [113]. The mass flow rate of each species leaving the CPOX is $W_i^{cpox} = M_i N_i$. The mass conservation property of chemical reactions ensures that the total mass flow across the CPOX is conserved, i.e., $\sum W_i^{cpox} = W^{cpox}$.

The temperature dynamic equation (6.21) can now be expanded. The enthalpy of the gas flow depends on the flow rate, the flow temperature, and the gas composition. Thus

$$\begin{bmatrix} \text{Enthalpy flow} \\ \text{in - out} \end{bmatrix} = W^{cpox} \left(C_P^{mix}(T_{mix} - T_{ref}) - C_P^{cpox}(T_{cpox} - T_{ref}) \right) \tag{6.48}$$
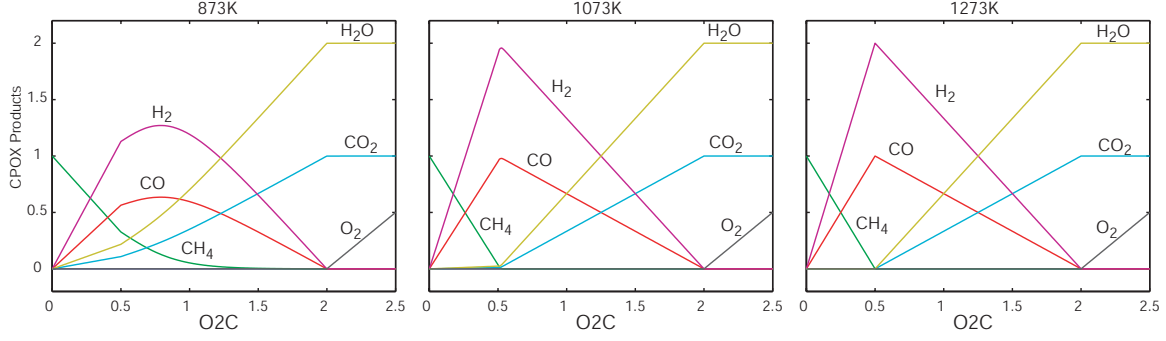
Figure 6.7: Products of CPOX reaction per unit of CH_4 entering CPOX

where T_{ref} is the reference temperature (298 K). The gas specific heat C_P^{mix} and C_P^{cpox} ($J/kg \cdot K$) are that of the gas in the mixer (gas before CPOX reaction) and the gas in the CPOX (after reaction), respectively. They are functions of gas composition and gas temperature.

$$C_P^{mix} = \sum x_i^{mix} C_{P_i}(T_{mix}) \tag{6.49}$$

$$C_P^{mix} = \sum x_i^{cpox} C_{P_i}(T_{cpox}) \tag{6.50}$$

where i represents four species in the MIX (Equation (6.33)) and seven species in the CPOX (Equation (6.47)). The heat released from the reaction depends on the amount of reaction taking place.

$$\begin{bmatrix} \text{Heat from} \\ \text{reaction} \end{bmatrix} = N_{CH_4 r} \left(S \cdot (-\Delta H_{pox}^0) + (1 - S) \cdot (-\Delta H_{tox}^0) \right)$$
$$+ N_{O_2 r H_2 CO} \left(\beta \cdot (-\Delta H_{hox}^0) + (1 - \beta) \cdot (-\Delta H_{cox}^0) \right) \tag{6.51}$$

where $-\Delta H_{pox}^0$, $-\Delta H_{tox}^0$, $-\Delta H_{hox}^0$, and $-\Delta H_{cox}^0$ (J/mol) are the heat released from POX, TOX, HOX, and COX reactions, respectively. Combining Equations (6.21), (6.48), and (6.51), the state equation of the CPOX temperature can be written as

$$\frac{dT_{cpox}}{dt} = \frac{1}{m_{bed}^{cpox} C_{P,bed}^{cpox}} \left[W^{cpox} \left(C_P^{mix}(T_{mix} - T_{ref}) - C_P^{cpox}(T_{cpox} - T_{ref}) \right) + \right.$$
$$N_{CH_4 r} \left(S \cdot (-\Delta H_{pox}^0) + (1 - S) \cdot (-\Delta H_{tox}^0) \right)$$
$$\left. + N_{O_2 r H_2 CO} \left(\beta \cdot (-\Delta H_{hox}^0) + (1 - \beta) \cdot (-\Delta H_{cox}^0) \right) \right] \tag{6.52}$$

The values of $-\Delta H_{pox}^0$, $-\Delta H_{tox}^0$, $-\Delta H_{hox}^0$, and $-\Delta H_{cox}^0$ are shown in Equations (6.22)-(6.25).

6.9 Water Gas Shift Converter and Preferential Oxidation Reactor (WROX)

The water gas shift converter and the preferential oxidation reactor are lumped together as one volume, denoted as WROX. Three flows entering the volume are H_2-rich gas flow from the CPOX, W^{cpox}, water injection needed for WGS reaction, $W_{H_2O}^{wgs}$, and air injection required for PROX reaction, W_{air}^{prox}. The flow rates of water injected into WGSs are equal to the amount that is needed to cool down the gas temperature to the desired WGS inlet temperatures [23, 37]. The amount of air supplied to the PROX reactor is normally twice that required to oxidize the rest of the CO in the gas stream based on the desired operating condition [23, 37]. The WROX model has two states: total pressure, p^{wrox}, and hydrogen pressure, $p_{H_2}^{wrox}$. Since the amount of CO created in CPOX is proportional to the rate of H_2 created (POX reaction), it is assumed, in the WROX model, that the rate of H_2 generated in

the WGS is a fixed percentage (η_{wrox}) of the rate of hydrogen generated in the CPOX. The state equations are

$$\frac{dp^{wrox}}{dt} = \frac{RT_{wrox}}{M_{wrox}V_{wrox}} \left(W^{cpox} - W^{wrox} + W^{wgs}_{H_2O} + W^{prox}_{air} \right) \tag{6.53}$$

$$\frac{dp^{wrox}_{H_2}}{dt} = \frac{RT_{wrox}}{M_{H_2}V_{wrox}} \left((1 + \eta_{wrox})W^{cpox}_{H_2} - x^{wrox}_{H_2}W^{wrox} \right) \tag{6.54}$$

where M_{wrox} is an average molecular weight of the gas in WROX, and T_{wrox} is an average temperature of WGSs and PROX. The WROX exit flow rate, W^{wrox}, is calculated using the nozzle equation (6.6) based on the pressure drop between WROX and anode volume, $p^{wrox} - p^{an}$. The hydrogen mass fraction in WROX, $x^{wrox}_{H_2}$, can be determined from the two states by

$$x^{wrox}_{H_2} = \frac{M_{H_2}}{M_{wrox}} \frac{p^{wrox}_{H_2}}{p^{wrox}} \tag{6.55}$$

The rate of water injected into WROX, $W^{wgs}_{H_2O}$, is equal to the amount that is required to cool the gas from CPOX down to the desired WGSs inlet temperatures. There are two WGS reactors and thus the total rate of water injected is $W^{wgs}_{H_2O} = W^{wgs1}_{H_2O} + W^{wgs1}_{H_2O}$. The flow rate of water into each WGS is calculated using energy balance between enthalpy of the gas flows, enthalpy of the flow at the desired temperature, and the heat of water vaporization. It is assumed that PROX air injection, W^{prox}_{air}, is scheduled based on the stack current at the value twice needed [23, 37] at the designed operating condition.

6.10 Anode (AN)

Mass conservation is used to model the pressure dynamic in the anode volume. To simplify the model, only three mass flows are considered, including flows into and out of the anode volume and the rate of hydrogen consumed in the fuel cell reaction. The dynamic equations are

$$\frac{dp^{an}}{dt} = \frac{RT_{an}}{M_{an}V_{an}} \left(W^{wrox} - W^{an} - W_{H_2,react} \right) \tag{6.56}$$

$$\frac{dp^{an}_{H_2}}{dt} = \frac{RT_{an}}{M_{H_2}V_{an}} \left(x^{wrox}_{H_2}W^{wrox} - x^{an}_{H_2}W^{an} - W_{H_2,react} \right) \tag{6.57}$$

where W^{an} is calculated as a function of the anode pressure, p^{an}, and the ambient pressure, p_{amb}, using Equation (6.6). The rate of hydrogen reacted is a function of stack current, I_{st}, through the electrochemistry principle [69]

$$W_{H_2,react} = M_{H_2} \frac{nI_{st}}{2F} \tag{6.58}$$

where n is the number of fuel cells in the stack and F is the Faraday's number.

Two meaningful variables which are hydrogen utilization, U_{H_2}, and stack H_2 starvation or anode hydrogen mole fraction, y_{H_2}, can be calculated by

$$U_{H_2} = \frac{W_{H_2,react}}{x^{wrox}_{H_2}W^{wrox}} \tag{6.59}$$

and

$$y_{H_2} = \frac{p^{an}_{H_2}}{p^{an}} \tag{6.60}$$

6.11   Simulation and Model Validation

The low-order (10 states) model described in the previous sections is parameterized and validated with the results of a high-order ($>$ 300 states) detailed model [40]. The detailed model includes spatial variation and exact chemical reaction rates for all the species. The detailed model is developed using the Dymola software [108] and is imported as an S-function in Simulink. The two models are compared with the same inputs. The model parameters for a system designed to be used in a commercial vehicle or a residential building are given in Table 6.3. The focus of our work is to capture the essential dynamic input/output behaviors, and, thus our main concern is reasonable agreement of transient responses. The FPS key performance variables are the O2C ratio, the CPOX temperature, the FPS exit total flow rate, and the FPS exit hydrogen flow rate. Several parameters, such as the orifice constants and the component volumes, are adjusted appropriately in order to obtain comparable transient responses. Note that the model is expected to provide close prediction of the transient response of the variables located upstream of the WGS inlet (WROX inlet). On the other hand, a relatively large discrepancy is expected for the variables downstream from the CPOX since the WGS and PROX reactors are approximately modeled as one lumped volume and are assumed perfectly controlled, which is not the case for the Dymola model.

The operating point used in the validation is chosen at the oxygen to carbon ratio $\lambda_{O2C} = 0.6$ and the stack hydrogen utilization $U_{H_2} = 80\%$ [37]. The final results are shown in Figures 6.8 to 6.12. Step changes of the three inputs: the stack current, I_{st}, the blower signal, u_{blo}, and the fuel valve signal, u_{valve}, are applied individually at time 400, 800, and 1200 seconds, respectively, followed by the simultaneous step changes of all inputs at 1600 seconds (see top three plots of Figure 6.8). The input u_{valve} has a value between 0 and 1 in these plots. Note here that, in practice, it is unlikely that an input is applied individually. Often, the blower and the valve inputs are applied simultaneously based on the changes in load current. It is therefore more critical to obtain good agreement on the responses in the case of simultaneous inputs (at 1600 seconds).

The responses of the key variables are shown in Figure 6.8. In the right column is the zoom-in of the response at 1600 seconds which represents the simultaneous input step increase. Various pressure and flow responses are shown in Figure 6.9. It can be seen that, despite the offset, there is a good agreement between the two models for most transient responses.

Small discrepancies can be spotted in the responses, for example, in the anode pressure. The discrepancies come mostly from the results of the assumptions used to simplify the model. The main assumption is that the WGS and PROX reactors are combined into one volume. This results in a crude approximation of the pressure in the WGS and PROX, as can be seen in Figure 6.11.

Steady-state offsets of the model can also be reduced. For example, the CPOX temperature offset shown in Figure 6.8 might be reduced if the enthalpy terms in the CPOX temperature equation (6.48) are directly calculated from gas composition and temperature rather than from a lumped specific heat.

From the validation results in this section, it can be concluded that the low-order model can be used to represent important dynamic behaviors that are relevant to the control study. A more accurate model can be developed with the expense of extra complexity or higher system order.
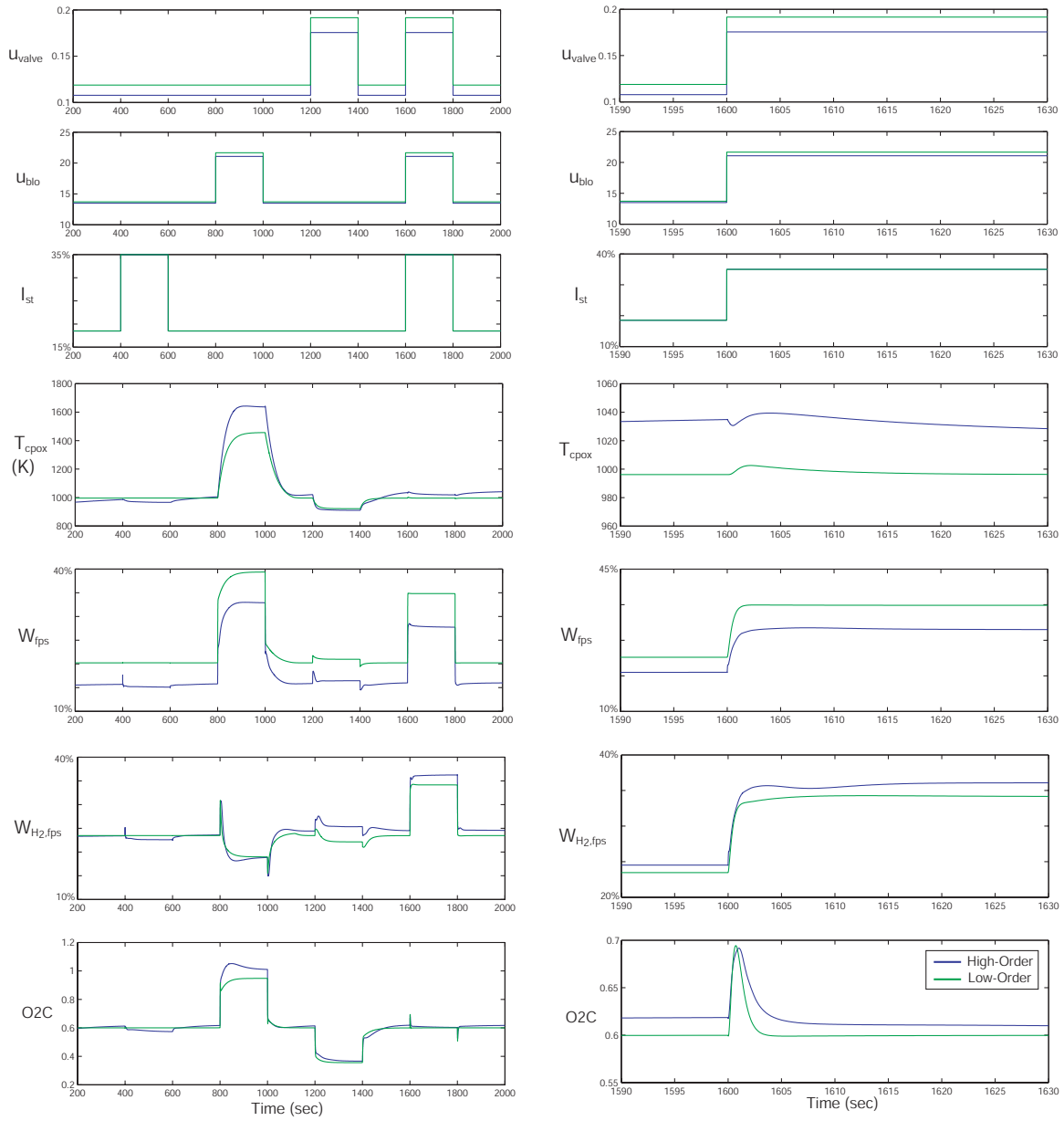
Figure 6.8: Model Validation Results: Inputs and Performance Variables. Blue (Dark) = high-order model; green (light) = low-order model
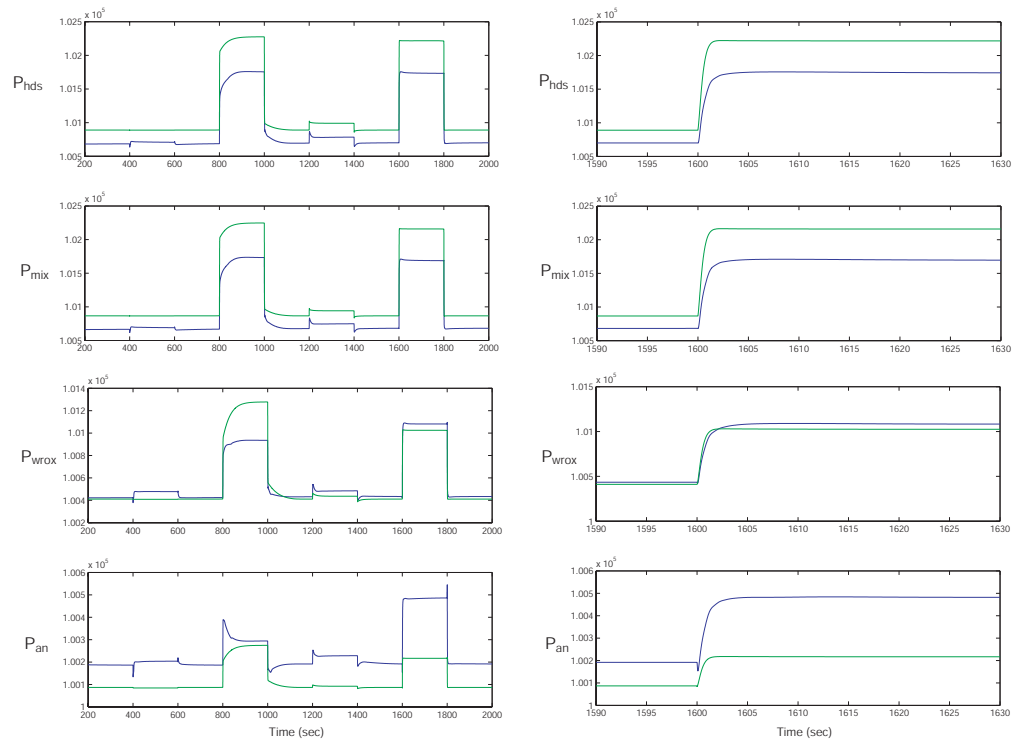
Figure 6.9: Model validation results: pressures (Pascal)
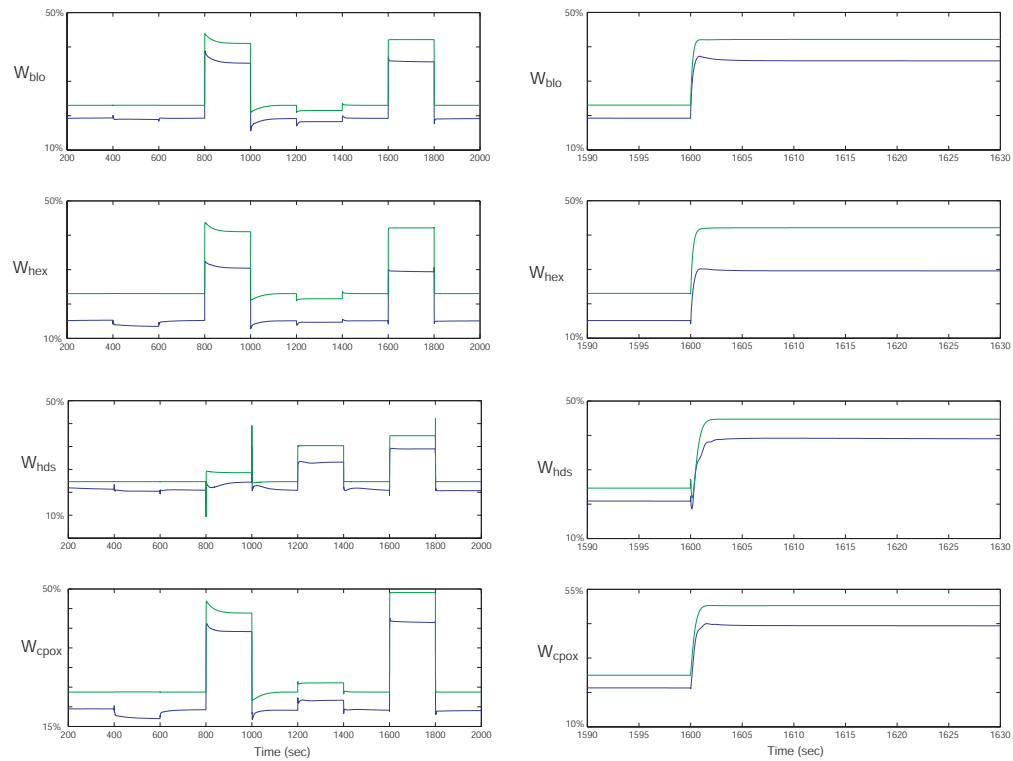
Figure 6.10: Model validation results: flow rates (% of full flow)
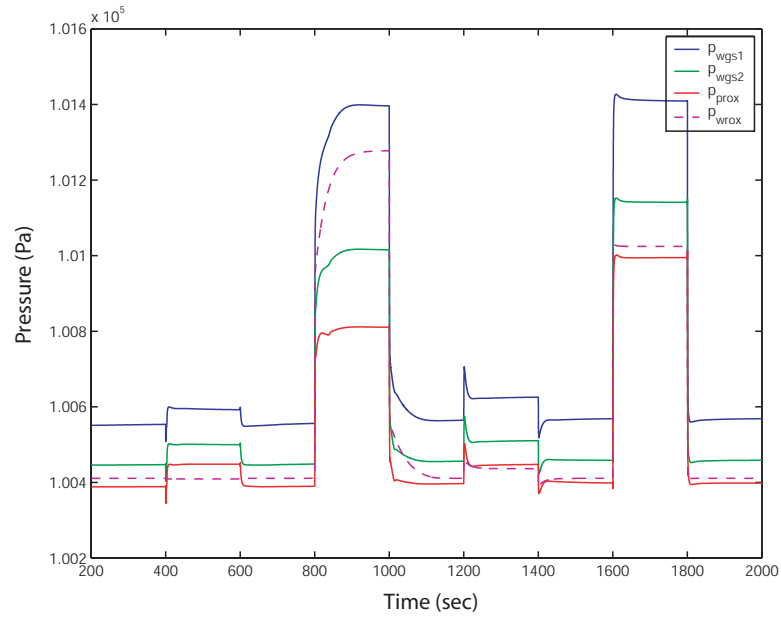
Figure 6.11: Model validation results: WROX pressure
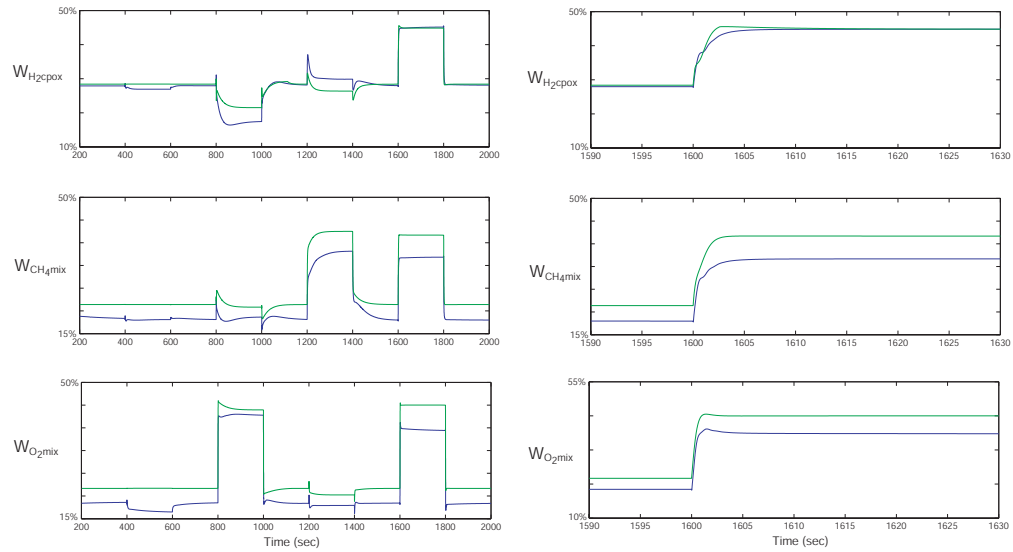
Figure 6.12: Model validation results: CPOX composition

Table 6.3: Typical model parameters for a 200kW system [23, 33, 36, 40, 92]

Parameter	Typical Value
T_{hex}	400-500 K
V_{hex}	0.05 m^3
$W_{0,hex}$	0.04 kg/s
$\Delta p_{0,hex}$	450-500 Pa
T_{hds}	350-400 °C
V_{hds}	0.3 m^3
p_{tank}	133 kPa
$W_{0,valve}$	0.0075 kg/s
$\Delta p_{0,valve}$	3600 Pa
$W_{0,hds}$	0.0075 kg/s
$\Delta p_{0,hds}$	100-110 Pa
T_{mix}	300 °C
V_{mix}	0.03 m^3
$C_{P,bed}^{cpox}$	450 J/kg·K
m_{bed}^{cpox}	2.8 kg
$W_{0,cpox}$	0.05 kg/s
$\Delta p_{0,cpox}$	3000 Pa
η_{wrox}	20-50 %
T_{wrox}	500 K
V_{wrox}	0.45 m^3
M_{wrox}	16×10^{-3} kg/mol
$T_{wgs1,in}^{des}$	400 °C
$T_{wgs2,in}^{des}$	200 °C
T_{wgs1}	400 °C
$W_{0,wrox}$	0.06 kg/s
$\Delta p_{0,wrox}$	2000 Pa
T_{an}	65-80 °C
V_{an}	0.0045 m^3
M_{an}	27.8×10^{-3} kg/mol
n	750-1000 Cells
$W_{0,an}$	0.06 kg/s
$\Delta p_{0,an}$	500-600 Pa

Chapter 7

Natural Gas Fuel Processor Control Study

Accurate control and coordination of the fuel processor reactant flows can prevent both large deviation of hydrogen concentration in the anode and large excursion of CPOX catalyst bed temperature. Good regulation of the CPOX temperature prevents the catalyst bed from overheating and ensures high conversion efficiency of the CPOX reaction, while accurate regulation of anode hydrogen concentration prevents the fuel cell stack from hydrogen starvation and ensures high fuel cell hydrogen utilization, i.e., low hydrogen waste. A control-oriented model of the natural gas fuel processing system developed in the previous chapter is used in this chapter for real-time management of these two objectives. The two main performance variables are the anode hydrogen mole fraction [99] and the CPOX catalyst bed temperature [113] and the two control actuators are the fuel (CH_4) valve command and the CPOX air blower command.

Typical fuel processing systems rely on a decentralized (single-input single-output) control of the air blower command to control CPOX temperature and of the fuel valve command to control the anode hydrogen concentration. In Section 7.4, an analysis using the relative gain array method confirms the appropriateness of input-output pairs for the decentralized control. The study also shows large interactions between the two loops at high frequencies, which suggest significant degradation of control performance during transient. Moreover, the magnitude of the interactions changes significantly at different operating powers. Large plant interactions at low power can result in instability if the decentralized controllers are designed separately with high bandwidth in both loops. Designing the two decentralized control loops at different bandwidth can prevent instability. This indicates the need to compromise one of the two objectives if a decentralized controller is used. Specifically, we show that fast control of the fuel loop is necessary to minimize stack H_2 starvation. The slow air flow loop is needed to prevent large controller performance degradation, which is caused by the plant interactions, and actuator saturation if a decentralized controller is used.

These interactions can be more efficiently handled with multivariable control which is studied in Section 7.5. The multivariable controller is designed based on a linearized model of the plant. The linear quadratic optimal control method is used to design the controller and the state estimator based on perfect measurements of the performance variables: the CPOX temperature and the anode H_2 mole fraction. An analysis of the controller and the closed loop performance shows that the model-based multivariable controller gives a significant improvement in the CPOX temperature regulation as compared to the decentralized controller. During load current changes, the regulation of the anode H_2 mole fraction depends strongly on the speed of the fuel valve command while the CPOX temperature regulation depends on the coordination of the two inputs.

An analysis of the multi-input multi-output controller, in Section 7.5.3, reveals one effective cross-coupling element of the controller. This is useful when simplifying the controller for implementation. The cross-coupling term from the anode H_2 mole fraction to the blower command significantly con-

tributes to the performance of the controller while the feedback term from the CPOX temperature to the valve command can be ignored without any degradation in performance. With additional analysis, the controller may be reduced further into a dynamic feedforward term from the valve command to the blower command, which can counterbalance the effects of the valve command on the CPOX temperature.

With realistic measurements where sensor lags are significant, the performance of the multivariable controller can degrade. The analysis of observability gramian, presented in Section 7.5.4, can be used to guide the control design and measurement selections. This observability analysis can also help in assessing the relative cost-benefit ratio in adding extra sensors for the flow and pressure measurements in the system.

7.1   Control Problem Formulation

As previously discussed, the main objectives of the FPS controller are (i) to protect the stack from damage due to H_2 starvation (ii) to protect CPOX from overheating and (iii) to keep overall system efficiency high, which includes high stack H_2 utilization and high FPS CH_4-to-H_2 conversion. Objectives (i) and (ii) are important during transient operations while objective (iii) can be viewed as a steady-state goal. Objectives (ii) and (iii) are also related since maintaining the desired CPOX temperature during steady-state implies proper regulation of the oxygen-to-carbon ratio which corresponds to high FPS conversion efficiency. In this study, the desired steady-state is selected at stack H_2 utilization U_{H_2}=80% [37] and CPOX oxygen-to-carbon ratio $\lambda_{O2C} = 0.6$. This condition results in the value of CPOX temperature, $T_{cpox} = 972$ K (corresponds to $\lambda_{O2C} = 0.6$), and the value of anode hydrogen mole fraction, $y_{H_2}^{an} \approx 8\%$ (corresponds to $U_{H_2} = 80\%$). The control objective is therefore to regulate T_{cpox} at 972 K and $y_{H_2}^{an}$ at 0.08. This desired value of $T_{cpox} = 972K$ also agrees with the value published in the literature [33].

The performance objectives are chosen based on the following rationale. High T_{cpox} can cause the catalyst bed to be overheated and be permanently damaged. Low T_{cpox} results in a low CH_4 reaction rate in the CPOX [113]. Large deviations of $y_{H_2}^{an}$ are undesirable. On one hand, a low value of $y_{H_2}^{an}$ means anode H_2 starvation [99, 97] which can permanently damage the fuel cell structure. On the other hand, a high value of $y_{H_2}^{an}$ means small hydrogen utilization which results in a waste of hydrogen.

In this control study, we ignore the effect of temperature on the CH_4 reaction rate. In other words, it is assumed that all CH_4 that enters the CPOX reacts. Note that these assumptions reduce the validity of the model for large T_{cpox} deviations. The effect of the modeling error due to these assumptions can degrade the performance of the model-based controller. However, achieving one of the control goals, which is the regulation of T_{cpox}, will ensure that this modeling error remains small.

The actuator dynamics are ignored. The stack current, I_{st}, is considered as an exogenous input that is measured. Since the exogenous input is measured, we consider a two degrees of freedom (2DOF) controller based on feedforward and feedback, as shown in Figure 7.1. The control problem is formulated using the general control configuration shown in Figure 7.2. The two control inputs, u, are
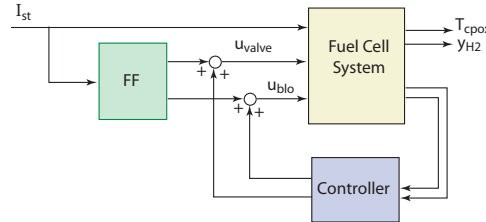
Figure 7.1: Feedback control study

the air blower signal, u_{blo}, and the fuel valve signal, u_{valve}. The feedforward terms that provide the valve and the blower signals that reject the steady-state effect of current to the outputs are integrated

in the plant:

$$u^* = \begin{bmatrix} u^*_{blo} \\ u^*_{valve} \end{bmatrix} = f_I(I_{st}) \tag{7.1}$$

The value of u^* is obtained by the nonlinear simulation and can be implemented with a lookup table. The performance variable, z, includes the CPOX temperature, T_{cpox}, and the anode exit hydrogen
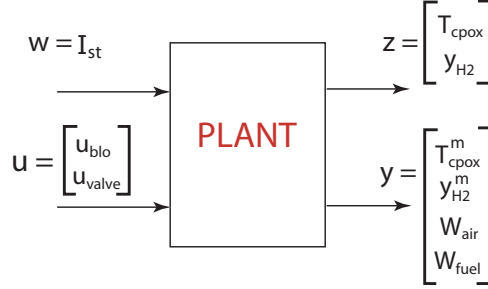
Figure 7.2: Control problem

mole fraction, $y^{an}_{H_2}$.

Several sets of measured variables are considered. The variables that can be potentially measured are the CPOX temperature, T^m_{cpox}, the hydrogen mole fraction, $y^m_{H_2}$, the air flow rate through the blower, W_{air}, and the fuel flow rate, W_{fuel}. The measured values, T^m_{cpox} and $y^m_{H_2}$, are the values obtained from realistic sensors, which are slow. The control objective is to reject or attenuate the response of z to the disturbance w by controlling the input, u, based on the measurement, y. In the transfer function form, we can represent the plant as

$$\begin{bmatrix} z \\ y \end{bmatrix} = G \begin{bmatrix} w \\ u \end{bmatrix} = \begin{bmatrix} G_{zw} & G_{zu} \\ G_{yw} & G_{yu} \end{bmatrix} \begin{bmatrix} w \\ u \end{bmatrix} \tag{7.2}$$

In order to determine the fundamental limitations or issues that are related to the plant based on the actuator topology and not the sensors, we first study the control design based on the perfect measurements of the performance variables, i.e., perfect measurements of T_{cpox} and $y^{an}_{H_2}$. Then, later in this chapter, we analyze the effect of realistic measurements, with sensor lag and noise, on the performance of the observer-based controller.

7.2 Analysis of Linearized Models

A linear model of the FPS is obtained by linearizing the nonlinear model developed in Chapter 6. The operating point is set at $\lambda_{O2C} = 0.6$ and $U_{H_2} = 0.8$ and static feedforward terms (illustrated in Figure 7.1) are included in the linear plant. The linearization of the plant is denoted by

$$\Delta \dot{x} = A\Delta x + B_u \Delta u + B_w \Delta w$$
$$\Delta z = C_z \Delta x + D_{zu} \Delta u + D_{zw} \Delta w$$

where the state, x, input, u, disturbance, w, and performance variables, z, are

$$x = \begin{bmatrix} T_{cpox} & p^{an}_{H_2} & p^{an} & p^{hex} & \omega_{blo} & p^{hds} & p^{mix}_{CH_4} & p^{mix}_{air} & p^{wrox}_{H_2} & p^{wrox} \end{bmatrix}^T$$

$$w = I_{st} \qquad u = \begin{bmatrix} u_{blo} & u_{valve} \end{bmatrix}^T \qquad z = \begin{bmatrix} T_{cpox} & y^{an}_{H_2} \end{bmatrix}^T \tag{7.3}$$

For simplicity, the symbol Δ, which denotes the deviation of the variables from the nominal point, will be dropped for the rest of the chapter. The specific set of matrices for a 50% current (load) level is given in Table A.3. The units of states are pressure in kPa, temperature in Kelvin, and rotational

speed in kRPM. The current input is in Ampere. The blower and the valve signals, u_{blo} and u_{valve}, vary between 0 and 100. The outputs are the CPOX temperature in Kelvin and the anode hydrogen mole fraction in percent. The comparison of time responses between the nonlinear and the linear models, in Figure A.2, shows acceptable agreements. The small offsets are the results of errors in the linearization of feedforward terms. The eigenvalues and eigenvectors of the linear system are shown in Table 7.1. It can be observed that the slow eigenvalue at -0.086 is associated with the CPOX temperature and the other slow eigenvalues at -0.358 and -1.468 are related to the hydrogen concentration in the stack anode volume and the WROX (water gas shift and preferential oxidation) volume. The controllability and observability data will be used later in Sections 7.5.1 and 7.5.2.

Table 7.1: Eigenvalues and eigenvectors of FPS linear model

Eigenvalues

λ	-1.4678	-0.3579	-660.66	-157.92	-89.097	-12.171	-2.7825+0.4612i	-2.7825-0.4612i	-0.085865	-3.3333

Eigenvectors

x1	T_{cpox}	0	0	-0.002922	-0.000033	0.035363	-0.248017	-0.7546	-0.7547	0.999908	0.699066
x2	p_{H2}^{an}	1	0.917378	-0.000284	0.164391	0.000331	0.138515	0.1135-0.0268i	0.1135+0.0268i	-0.006255	0.090218
x3	p^{an}	0	0	-0.000764	0.984706	-0.004846	-0.042203	-0.0024-0.0005i	-0.0024+0.0005i	0.000506	0.001705
x4	p^{hex}	0	0	0.283168	0.006251	0.367157	0.040987	0.0012-0.0072i	0.0012+0.0072i	0.001372	-0.007774
x5	ω_{blo}	0	0	0	0	0	0	0	0	0	0.000326
x6	p^{hds}	0	0	0.069280	0.000478	-0.065690	0.065140	0.0013-0.0085i	0.0013+0.0085i	0.001513	-0.009961
x7	p_{CH4}^{mix}	0	0	-0.733729	-0.001551	0.710624	-0.642110	-0.4437+0.0738	-0.4437-0.0739	0.003010	0.492812
x8	p_{air}^{mix}	0	0	-0.613602	-0.000305	-0.595383	0.682953	-0.4449-0.0815i	-0.4449+0.0815i	-0.001495	-0.501783
x9	p_{H2}^{wrox}	0	0.398016	0.003223	-0.013867	-0.006765	-0.013953	0.0991+0.0011i	0.0991-0.0011i	-0.011143	-0.091075
x10	p^{wrox}	0	0	0.011485	-0.055638	-0.009657	-0.180758	-0.011-0.0024i	-0.011+0.0024i	0.002347	0.007750

Controllability

cond(λI-A Bu)	5838.78	24130.73	12932.24	462598.60	5113.45	8426.44	5802.98	5803.98	5696.54	5800.03

Observability

cond(λI-A;Cz)	839.51	4245.69	275896.56	7375.08	17499.82	2539.83	924.46	924.46	2152.40	1000.53

The nonlinear plant model is linearized at three different current (load) levels, 30%, 50%, and 80%, which will be referred to as 30%, 50%, and 80% systems (or models), respectively. The Bode plots and step responses of the linear plants that are obtained from different system power levels are shown in Figures 7.3 and 7.4. For clarity, in these two figures, the units of current is ($\times$10 Amp). Note first that the static feedforward controller does well in rejecting the effect from I_{st} to y_{H_2} in steady-state. The H_2 recovery using feedforward is, however, relatively slow. A feedback controller is, thus, needed to speed up the system behavior and to reduce the sensitivity introduced by modeling uncertainties.

The responses of the output due to step changes in the actuator signals, in Figure 7.4, show a strongly coupled system. The fuel dynamics are slower than the air dynamics, primarily due to the large HDS volume. Note that a right half plane (RHP) zero exists in the path $u_{blo} \rightarrow y_{H_2}$ can be easily detected from an initial inverse response of the y_{H_2} due to a step change in u_{blo}. Moreover, as can be seen in the step responses from u_{blo} to y_{H_2}, the RHP zero that causes the non-minimum phase behavior moves closer to the imaginary axis and causes larger initial inverse response at low power level (30%). It can also be seen in the Bode plot that, at high frequencies, the disturbance, I_{st}, has considerably more effect on the H_2 mole fraction than CPOX temperature, as compared to that at low frequencies. This is because the current has direct impact on the amount of hydrogen used in the anode, which is coupled with the H_2 mole fraction only through the fast dynamics of the gas in anode volume.

Table 7.2: Gap between two linearized systems

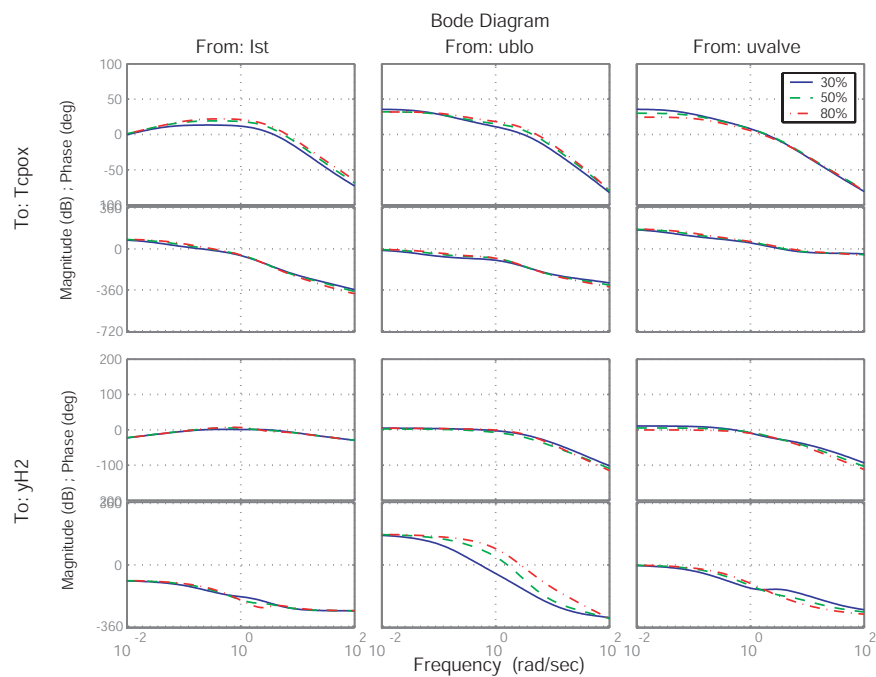| Linearization Points (power level)	Gap
30% and 50%	0.3629
50% and 80%	0.3893
30% and 80%	0.6624

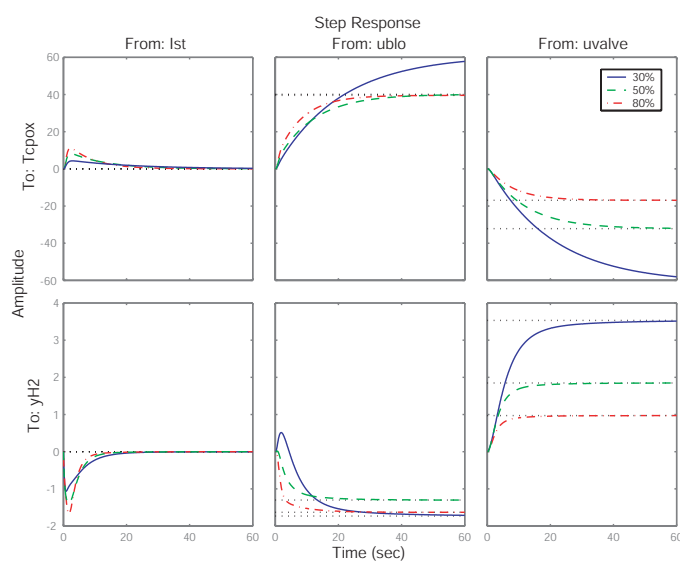Figure 7.3: Bode plot of linearized models at 30%, 50%, and 80% power

Figure 7.4: Step responses of linearized models at 30%, 50%, and 80% power

The characteristics of the FPS plant can vary when operating at different load levels or operating points. The distance between two system matrices is represented by the gap metric [50], which has values between zero and one. More specifically, the gap metric represents the degradation of stability margins when the first system is perturbed to become the second system [103]. A value closer to one indicates a large distance between the two systems. The gap metrics of three linear models of the plant, which are obtained by linearizing the nonlinear model at three different current (load) levels, 30%, 50%, and 80%, are presented in Table 7.2. MATLAB μ-Analysis Toolbox is used to calculate the gap metrics. From the large value of the gap between 30% and 80% models, it is expected that there will be a large degradation of control performance when a linear controller designed for one model is used on the other. This suggests the need for gain scheduling that can be pursued in the future. The linearization of the system at the 50% power level which is shown in Table A.3 is used in the control study in the following sections.

7.3   Input-Output Pairing

One of the most common approaches to controlling a multi-input multi-output (MIMO) system is to use a diagonal controller, which is often referred to as a decentralized controller. The decentralized control works well if the plant is close to diagonal which means that the plant can be considered as a collection of individual single-input single-output (SISO) sub-plants with no interaction among them. In this case, the controller for each sub-plant can be designed independently. If an off-diagonal element is large, then the performance of the decentralized controller may be poor.

The design of a decentralized controller involves two steps: input-output pairing and controller tuning. Interactions in the plant must be considered as we choose input-output pairs. For example, having a choice, one would drop the pairing between u_{blo} and y_{H_2} due to the RHP non-minimum phase relationship. One method used to measure the interactions and assess appropriate pairing is called the Relative Gain Array (RGA) [22]. The RGA is a complex non-singular square matrix defined as

$$RGA(G) = G \times (G^{-1})^T \tag{7.4}$$

where $\times$ denotes element by element multiplication. Each element of the RGA matrix indicates the interaction between the corresponding input-output pair. It is preferred to have a pairing that gives an RGA matrix close to an identity matrix. The useful rules for pairing are defined in [96]:

1. To avoid instability caused by interactions at low frequencies one should *avoid* pairings with negative steady-state RGA elements.
2. To avoid instability caused by interactions in the crossover region one should *prefer* pairings for which the RGA matrix in this frequency range is close to identity.

The 2×2 RGA matrices of G_{zu} defined in (7.2)-(7.3) and calculated for the 50% load in section 7.2 are given in (7.5) for different frequencies. According to the first rule, it is clear that the preferred pairing choices are $u_{blo} \rightarrow T_{cpox}$ pair and $u_{valve} \rightarrow y_{H_2}$ pair to avoid instability at low frequencies.

$$
\begin{aligned}
RGA(0 \text{ rad/s}) &= \begin{bmatrix} 2.302 & -1.302 \\ -1.302 & 2.302 \end{bmatrix} \\
RGA(0.1 \text{ rad/s}) &= \begin{bmatrix} 2.1124 - 0.36663i & -1.1124 + 0.36663i \\ -1.1124 + 0.36663i & 2.1124 - 0.36663i \end{bmatrix} \\
RGA(1 \text{ rad/s}) &= \begin{bmatrix} 1.1726 - 0.50797i & -0.17264 + 0.50797i \\ -0.17264 + 0.50797i & 1.1726 - 0.50797i \end{bmatrix} \\
RGA(10 \text{ rad/s}) &= \begin{bmatrix} 0.24308 - 0.0021386i & 0.75692 + 0.0021386i \\ 0.75692 + 0.0021386i & 0.24308 - 0.0021386i \end{bmatrix}
\end{aligned}
\tag{7.5}
$$

However, it can be seen that at high frequencies, the diagonal and off-diagonal elements are closer, which indicates more interactions. In fact, a plot of the magnitude difference between the diagonal and

off-diagonal elements of the RGA matrices in Figure 7.5 shows that the interactions increase at high frequencies [80, 96]. At low power levels, the values of the off-diagonal elements of the RGA matrix are even higher than the diagonal elements ($|RGA_{11}| - |RGA_{12}| < 0$), indicating large coupling. At these frequencies, we can expect poor performance from a decentralized controller.
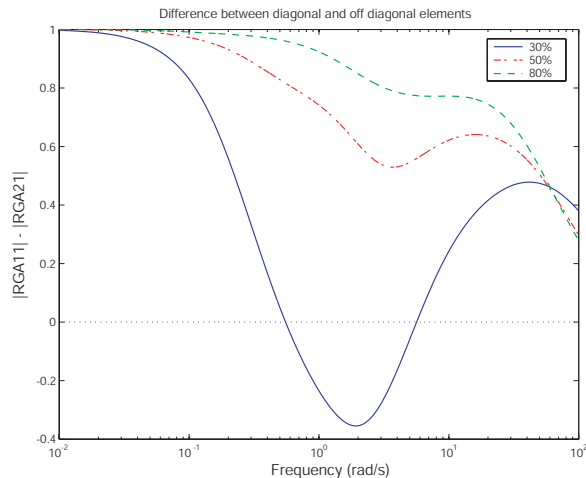
Figure 7.5: Difference between diagonal and off-diagonal elements of the RGA matrix at different frequencies for three power setpoints

7.4 Decentralized Control

To illustrate the effect of the interactions, we design several PI controllers for the two single-input single-output (SISO) systems that correspond to the diagonal subsystem of G_{zu}, i.e., $u_{blo} \rightarrow T_{cpox}$ ($G_{zu}(1,1)$), and $u_{valve} \rightarrow y_{H_2}$ ($G_{zu}(2,2)$). The diagram in Figure 7.6 shows the decentralized controller.
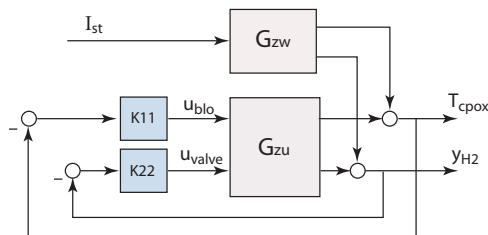
Figure 7.6: Decentralized Control

Each controller gives different closed loop characteristics, as shown in Tables 7.3 and 7.4. The closed loop bode plots and step responses of the system with different controllers are shown in Figures 7.7 to 7.12. Three responses are shown in each figure which are open loop or feedforward response (solid), decentralized feedback response of the full plant (dashed), and the ideal decentralized control response (dotted) which is the expected response if the off-diagonal elements of G_{zu} (see (7.2)) are zero.

Relatively slow controllers (K11a and K22a) in both loops are used for the response in Figure 7.7. It can be seen that the performance of the slow decentralized controller does not deteriorate significantly when the cross-coupling interactions are introduced. Despite its robustness, the slow controller corresponds to large y_{H_2} excursions during transient. Thus, a faster controller is needed. Figure 7.8 shows

Table 7.3: Controller for $G_{zu}(1,1)$

Controller	Transfer Function	Rise Time (s)	Overshoot (%)
K11a	$0.0389\dfrac{(4.1s+1)}{s}$	3.14	11
K11b	$0.0667\dfrac{(4.3s+1)}{s}$	1.0	7
K11c	$0.0135\dfrac{(5.6s+1)}{s}$	6.58	12

Table 7.4: Controller for $G_{zu}(2,2)$

Controller	Transfer Function	Rise Time (s)	Overshoot (%)
K22a	$0.268\dfrac{(2.8s+1)}{s}$	3.95	6
K22b	$0.165\dfrac{(21s+1)}{s}$	1.33	10

the closed-loop response when faster controllers (K11b and K22b) are employed in both loops. The control performance starts deteriorating due to system interactions. Moreover, since the interaction is larger for the low power (30%) system, the performance of fast decentralized control deteriorates significantly and can even destabilize the system as shown in Figure 7.9. To prevent the deteriorating effect of the interactions, it is possible to design the two controllers to have different bandwidth. Figure 7.10 shows the response when using slow controller in the fuel loop (K22a) and fast controller in the air loop (K11b). It can be observed here that the recovery speed of y_{H_2} mainly depends on the speed of the fuel valve, or fuel flow, and thus fast H2-valve loop is necessary. Therefore, we tune the PI controller K22 of the $u_{valve} \rightarrow y_{H_2}$ subsystem to achieve the desired y_{H_2} response ($|y_{H_2}| < 0.08$). To get fast y_{H_2} response while avoiding the effect of the interactions, the T_{cpox}-air loop needs to be much slower or faster than the $u_{valve} \rightarrow y_{H_2}$ closed loop subsystem. Unfortunately, faster $u_{blo} \rightarrow T_{cpox}$ is not feasible due to actual magnitude constraints. Thus K11 = K11c is selected, which slows down the first subsystem loop compromising the T_{cpox} response, as shown in Figures 7.11 and 7.12. These two figures show that large time scale separation is needed in order to use the decentralized control method. In the following sections, for comparison with other controllers, the PI controllers K11c and K22b are used.

The gains of the PI controllers (Tables 7.3 and 7.4) used in this study are obtained by trial and error to match the desired speed and overshoot of each controller. These gains are used only to illustrate the effect of plant interactions and difficulties in tuning the PI controllers without systematic MIMO control tools. The conclusion from this section is that the large plant interactions illustrated by Figure 7.5 must be considered in the control design.

7.5 Multivariable Control

We show in the previous section that the interactions in the plant limit the performance of the decentralized controller. In this section, we determine the improvement that can be gained by using

Figure 7.7: Bode magnitude and unit step response of 50% model with controllers K11a and K22a

Figure 7.8: Bode magnitude and unit step response of 50% model with controllers K11b and K22b

Figure 7.9: Bode magnitude and unit step response of 30% model with controllers K11b and K22b
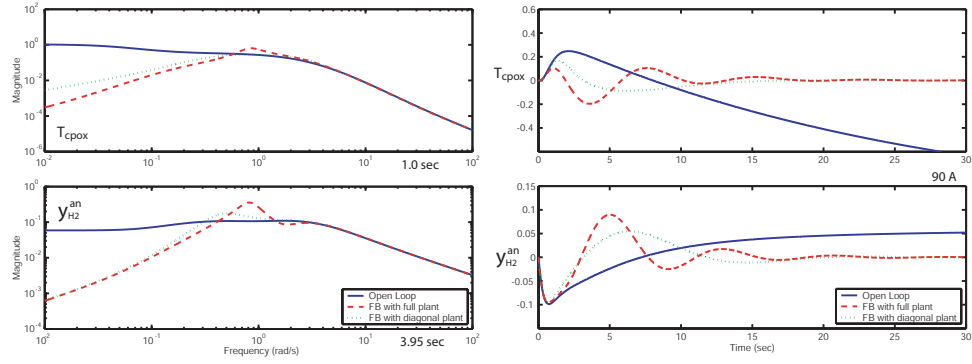
Figure 7.10: Bode magnitude and unit step response of 30% model with controllers K11b and K22a
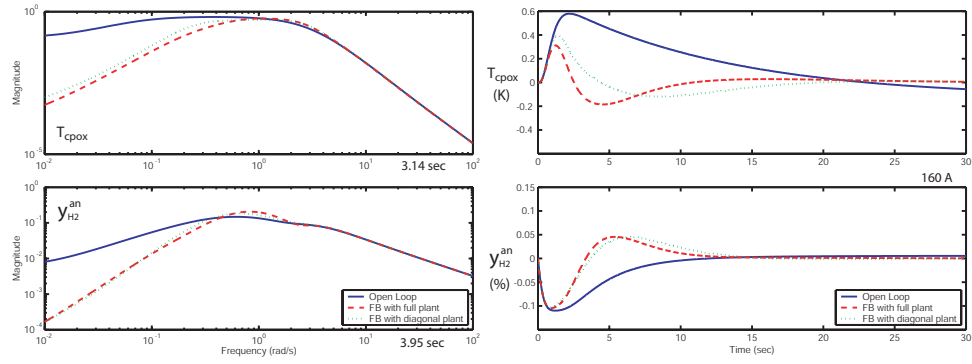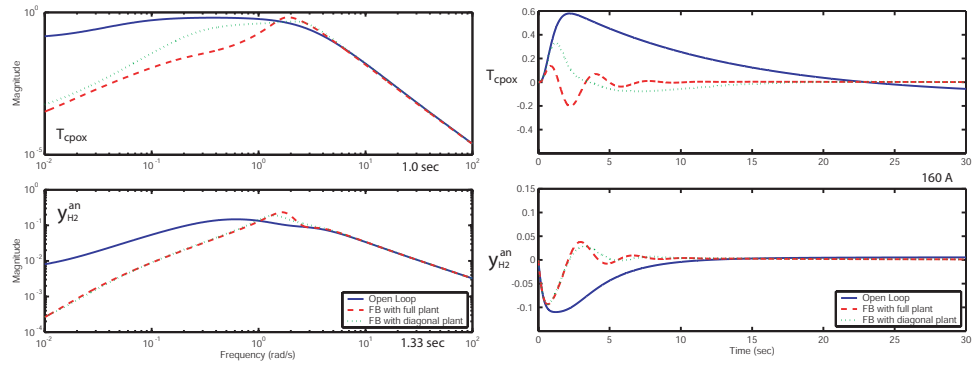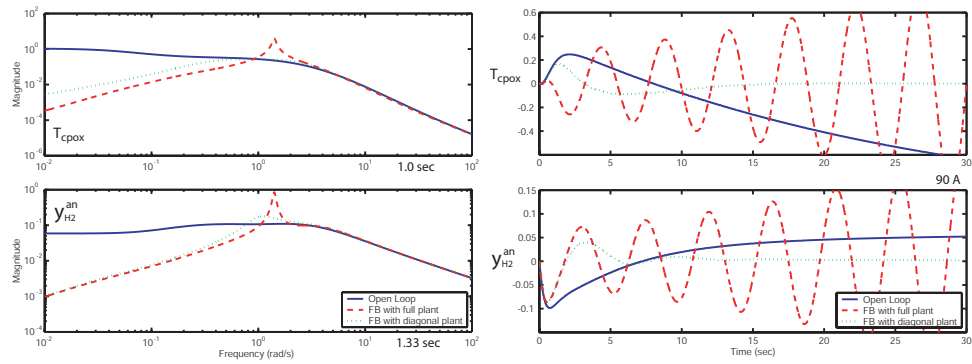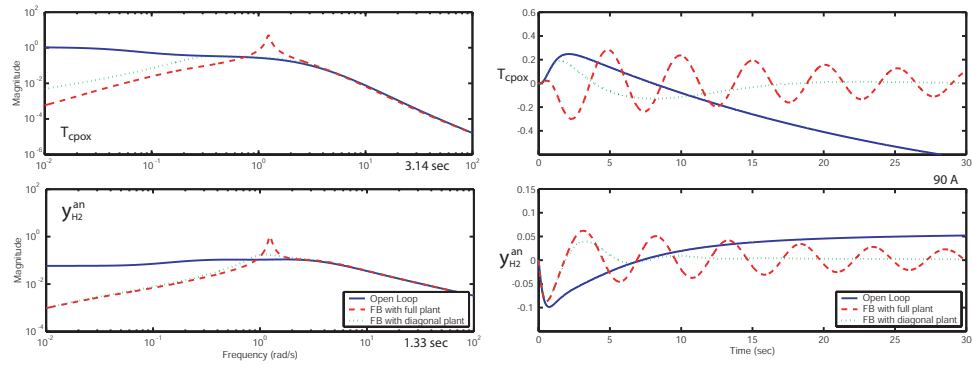

Figure 7.11: Bode magnitude and unit step response of 30% model with controllers K11a and K22b
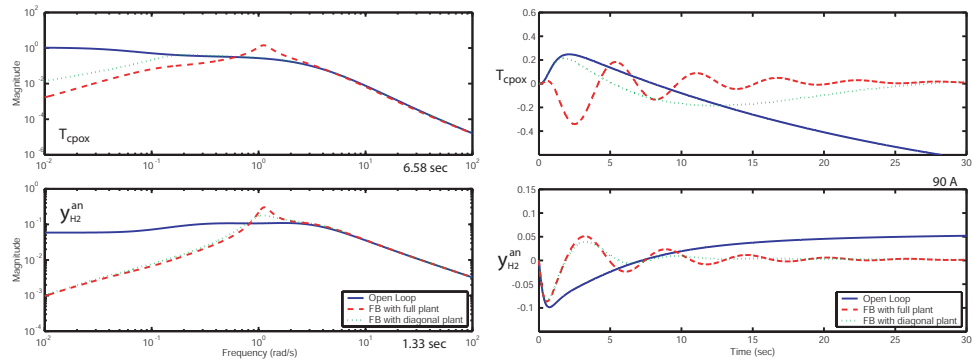
Figure 7.12: Bode magnitude and unit step response of 30% model with controllers K11c and K22b

a multi-input multi-output (MIMO) controller and model-based control design techniques. The controller is designed using the linear quadratic (LQ) method. The control development consists of two steps. First, a full state feedback controller is designed using linear quadratic optimization for the controller gains. Since the plant states can not be practically measured, the second step is to build a state observer or state estimator based on the measurement of the performance variables.

7.5.1 Full State Feedback with Integral Control

To eliminate steady-state error, we add to the controller the integrators on the two performance variables, T_{cpox} and y_{H_2}. Note that in this section, we assume that these two variables can be directly and instantaneously measured. The state equations of the integrators are

$$\frac{d}{dt}\left[\begin{array}{c} q_1 \\ q_2 \end{array}\right] = \left[\begin{array}{c} T_{cpox}^{ref} - T_{cpox} \\ y_{H_2}^{ref} - y_{H_2} \end{array}\right] \tag{7.6}$$

where $T_{cpox}^{ref} = 972$ K and $y_{H_2}^{ref} = 8.8$ % are the desired values of T_{cpox} and y_{H_2}, respectively. In the linear domain, the desired deviation from the reference values is thus zero for all current commands. The augmented plant, which combines the original states, x, and the integrator states, q, is represented by

$$\dot{x}_a = \left[\begin{array}{c} \dot{x} \\ \dot{q} \end{array}\right] = \left[\begin{array}{cc} A & 0 \\ Cz & 0 \end{array}\right]\left[\begin{array}{c} x \\ q \end{array}\right] + \left[\begin{array}{c} B_u \\ D_{zu} \end{array}\right] u = A_a x_a + B_a u \tag{7.7}$$

The controller is designed with the objective of minimizing the cost function

$$J = \int_0^\infty z^T Q_z z + u^T R u + q^T Q_I q \, dt \tag{7.8}$$

where $u = [u_{blo} \quad u_{valve}]^T$ and Q_z, R, and Q_I are weighting matrices on the performance variables, z, control input, u, and integrator state, q, respectively. The cost function can be written in the linear quadratic form of the augmented states, x_a, as

$$J = \int_0^\infty x_a^T \left[\begin{array}{cc} C_z^T Q_z C_z & 0 \\ 0 & Q_I \end{array}\right] x_a + u^T R u \, dt = \int_0^\infty x_a^T Q x_a + u^T R u \, dt \tag{7.9}$$

The control law that minimizes (7.9) is in the form

$$u = -K_P(x - x_d) - K_I q = -K\left[\begin{array}{c} (x - x_d) \\ q \end{array}\right] = -R^{-1}B_a^T P\left[\begin{array}{c} (x - x_d) \\ q \end{array}\right] \tag{7.10}$$

where P is the solution to the Algebraic Riccati Equation (ARE)

$$P A_a + A_a^T P + Q - P B_a R^{-1} B_a^T P = 0 \tag{7.11}$$

which can be solved using MATLAB. Variable x_d in (7.10) can be viewed as the desired value of the states (as a function of w) that gives the desired value of $z = 0$. In other words, the term $K_p x_d$ is an additional feedforward term that compensates for the changes in the output steady-state value due to the feedback. As a result, this additional feedforward term is a function of the feedback gain, K_p. The value of x_d can be found by simulation or by the linear plant matrices, i.e.,

$$x_d = \left[A^{-1}B_w\right] w \tag{7.12}$$

which results in

$$x_d^T = 10^{-3} \times \left[\begin{array}{cccccccccc} 0 & 0.67 & 7.538 & 84.148 & 7.941 & 79.219 & 18.197 & 59.761 & 8.9 & 35.72 \end{array}\right] w \tag{7.13}$$

As it is based on the linear model, the value of x_d calculated in (7.12) will be different from the actual desired state in the nonlinear plant. The error in x_d definitely influences the steady-state error of

the performance variables, T_{cpox} and y_{H_2}. The integral control implemented through the augmented integrators (7.6) then becomes more critical. The fact that x_d is not accurate must be taken into account when choosing the weighting between Q_z and Q_I. Large integrator gain slows down the response, thus relatively small Q_I shows a better (faster) performance in the linear design. However, the response in nonlinear simulation with small Q_I gives poor steady-state performance since the performance is based heavily on the proportional part of the controller and therefore suffers from the error in x_d. Thus, if a more accurate value of x_d can not be obtained, the transient performance must be compromised in order to get satisfactory steady-state performance of the controller through the integral part. Alternatively, a more accurate x_d can be obtained by numerically solving the nonlinear simulation and stored in a lookup table.

Figures 7.13 and 7.14 show the closed-loop responses when different weighting matrices are used in the LQ design. The effect of varying u_{valve}, while constraining the magnitude of u_{blo}, is shown in Figure 7.13. When the magnitude of u_{valve} increases, a faster response of y_{H_2} can be achieved with a small degradation of the T_{cpox} response. On the other hand, Figure 7.14 shows large tradeoff between two performance variables when the magnitude of u_{blo} is varied while maintaining the magnitude of u_{valve}. It can be seen that a small improvement in y_{H_2} can be obtained using u_{blo}. However, there is a large degradation in T_{cpox} response because large u_{blo} is needed to improve y_{H_2} (due to the non-minimum phase relation) and, thus significantly affects T_{cpox}. These two figures imply that the improvement in H_2 starvation (y_{H_2}) mainly depends on the speed and magnitude of the valve command, u_{valve}. The blower command, u_{blo}, has little impact on y_{H_2}, but if well coordinated with the valve command, it can provide a large improvement in T_{cpox} regulation.
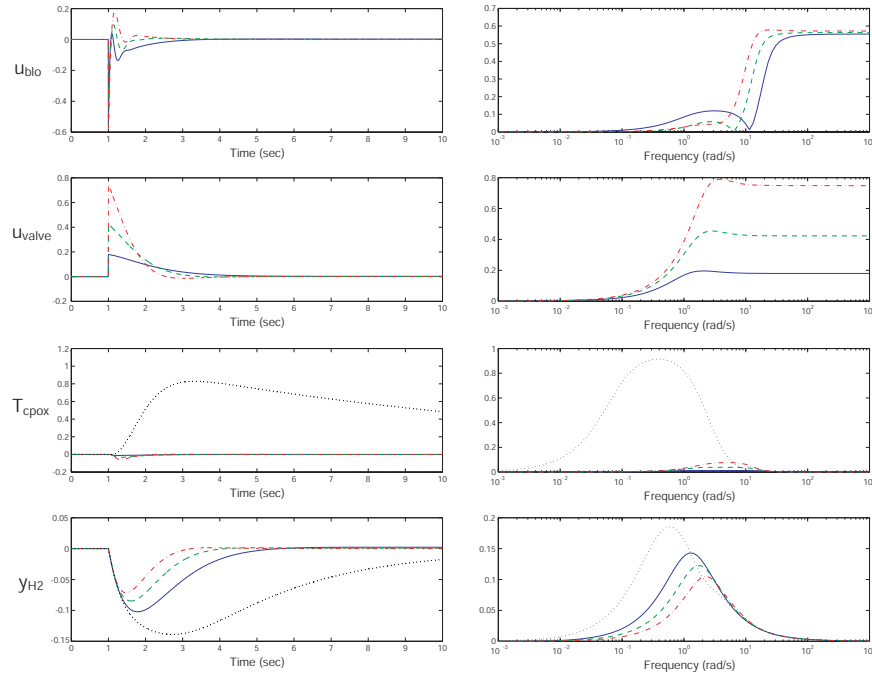
Figure 7.13: Tradeoff between two performance variables, T_{cpox} and y_{H_2}, with respect to magnitude of u_{valve}

The final design of the controller gives the response shown in Figure 7.15. The controller gains are obtained by using the weighting matrices

$$Q_z = \begin{bmatrix} 80 & 0 \\ 0 & 1100 \end{bmatrix} \qquad Q_I = \begin{bmatrix} 150 & 0 \\ 0 & 100 \end{bmatrix} \qquad R = \begin{bmatrix} 100 & 0 \\ 0 & 120 \end{bmatrix} \qquad (7.14)$$
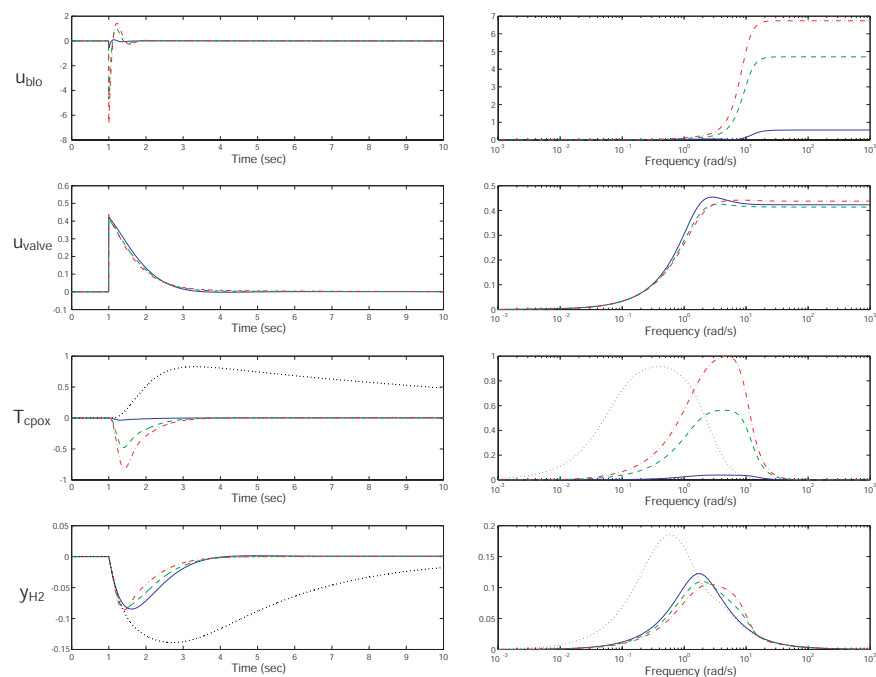
Figure 7.14: Tradeoff between two performance variables, T_{cpox} and y_{H_2}, with respect to magnitude of u_{blo}
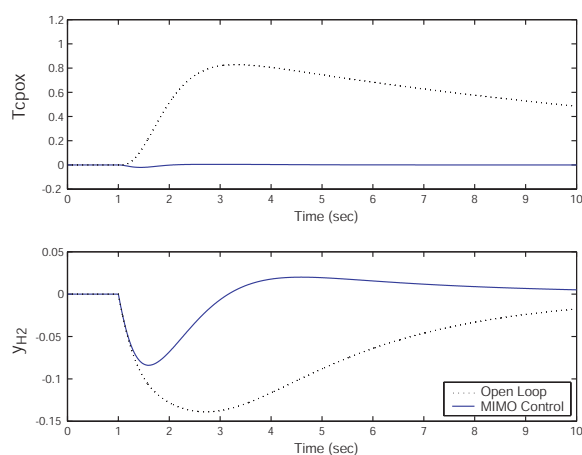
Figure 7.15: Response of the FPS linear model with the controller from LQ design

which results in the gains

$$K_P = \begin{bmatrix} 1.405 & 0.182 & 0.029 & 1.066 & 39.04 & -6.611 & -0.705 & 0.604 & 0.767 & 0.939 \\ -0.130 & 1.150 & -0.132 & -0.244 & -8.422 & 6.111 & 0.618 & -0.139 & 3.787 & 0.127 \end{bmatrix}$$

$$K_I = \begin{bmatrix} -1.207 & -0.169 \\ 0.189 & -0.9 \end{bmatrix} \tag{7.15}$$

The closed loop eigenvalues are given in the Appendix (Equation A.5).

There are a few slow closed loop eigenvalues which may be the result of the weakly controllable mode associated with the plant eigenvalue $\lambda_2 = -0.3579$, as suggested by the large condition number of $[\lambda_2 I - A \ Bu]$ in Table 7.1.

A comparison of the decentralized controller, explained in Section 7.4, and the full state feedback controller in nonlinear simulation is shown in Figure 7.16. The significant improvements in both T_{cpox} and y_{H_2} regulation when using MIMO controller are the result of considering system interactions via the model-based state feedback design. To be able to implement the MIMO controller, in the next section, the full state feedback controller is converted into output feedback using available measurements.
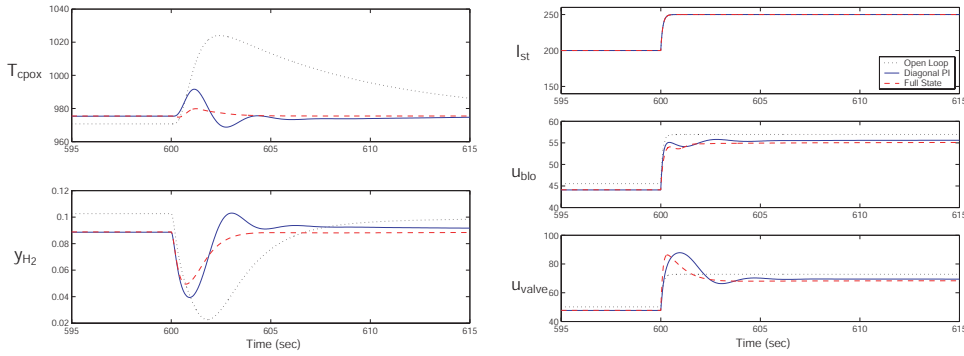
Figure 7.16: Comparison of decentralized control and full state feedback control in nonlinear simulation

7.5.2   State Estimator

The plant states can be estimated using the dynamic model of the plant together with available measurements. It is assumed here that perfect measurement of T_{cpox} and y_{H_2} can be obtained. The observer state equations are

$$\dot{\hat{x}} = A\hat{x} + B_u u + B_w w + L(z - \hat{z})$$
$$\hat{z} = C_z \hat{x} + D_{zu} u + D_{zw} w \tag{7.16}$$

where $\hat{x}$ is the estimator state vector and L is the estimator gain. The observability gramian, Q_{obs}, i.e. solution of

$$A^T Q_{obs} + Q_{obs} A = -C_z^T C_z, \tag{7.17}$$

has full rank but the condition number of the observability gramian is high, indicating rank deficiency, i.e., weak observability. Sometimes, this result arises because of poor selection of units of the model states (scaling). Thus, to better evaluate system observability, we normalize the condition number of the observability gramian (c_{obs}^N) by the value when all the states are measured, $C_x = I$.

$$c_{obs}^N = \frac{\text{cond}\left(Q_{obs, \{C=C_z\}}\right)}{\text{cond}\left(Q_{obs, \{C=I\}}\right)} = 2 \times 10^5 \tag{7.18}$$

Large normalized observability gramian implies that the pair (A, C_z) is weakly observable.

The L gain in (7.16) is used to place the observer eigenvalue at the desired points, which is normally at least twice as fast as the dominant closed loop eigenvalues. Since the plant has several fast eigenvalues (Table 7.1) that do not need to be moved using output feedback, the reduced-order observer can be applied to simplify the observer. This can be done by first transforming the system matrices into the modal canonical form [26], $x_1 = Tx$, such that the new system matrices are

$$A_1 = TAT^{-1} = \begin{bmatrix} \lambda_1 & & 0 \\ & \ddots & \\ 0 & & \lambda_{10} \end{bmatrix} \tag{7.19}$$

$$C_1 = C_z T^{-1} \qquad B_1 = [\, B_{1w}\ B_{1u}\,] = T\,[\, B_w\ B_u\,] \qquad D_1 = [D_{zw}\ D_{zu}\,] \tag{7.20}$$

Note the special structure of the matrix A_1 which has eigenvalues on the diagnonal. The system matrices in the new coordinates are shown in Table A.4. The matrices are then partitioned into

$$\begin{bmatrix} A_{1\bar{o}} & 0 \\ 0 & A_{1o} \end{bmatrix}, \qquad \begin{bmatrix} B_{1\bar{o}} \\ B_{1o} \end{bmatrix}, \qquad [\, C_{2\bar{o}}\ C_{2o}\,] \tag{7.21}$$

where

$$A_{1o} = \begin{bmatrix} -3.333 & 0 & 0 & 0 & 0 & 0 \\ 0 & -2.782 & 0.4612 & 0 & 0 & 0 \\ 0 & -0.4612 & -2.782 & 0 & 0 & 0 \\ 0 & 0 & 0 & -1.468 & 0 & 0 \\ 0 & 0 & 0 & 0 & -0.358 & 0 \\ 0 & 0 & 0 & 0 & 0 & -0.086 \end{bmatrix} \tag{7.22}$$

which contains the slow eigenvalues of the plant. The reduced-order observer gain, L_1, is then designed for the set $A_{1x} = A_{1o} + \alpha I$, B_{1o} and C_{1o}. The modification of A_{1o} to A_{1x} follows the method described in [7] to guide the observer pole placement for fast response as prescribed by the constant α. Using the Kalman filter method, the observer gain, L_1, is determined by solving the optimal quadratic problem

$$L_1 := SC_{1o}^T W_y^{-1} \tag{7.23}$$

$$0 = SA_{1o}^T + A_{1o}S + V_x + SC_{1o}^T W_y^{-1}C_{1o}S \tag{7.24}$$

The weighting matrices, V and W, represent the process noise and measurement noise, respectively. The weighting matrices chosen are

$$V_x = 100\,\text{diag}[\,10\ 200\ 200\ 20\ 50\ 80\,] + B_{1o}\,B_{1o}^T \tag{7.25}$$
$$W_y = 1{\times}10^{-6}\,\text{diag}\,[\,0.1\ 0.01\,] \tag{7.26}$$

The reduced-order observer gain, L_1, is then transformed to the original coordinate, L,

$$L = T^{-1}\begin{bmatrix} 0_{4\times 2} \\ L_1 \end{bmatrix} \tag{7.27}$$

which results in the gain given in Equation A.6. Figure 7.17 shows the response of the observer error $(x - \hat{x})$ in linear simulation. The initial errors of all states are set at 1% of the maximum deviation from the nominal point. It can be seen that most states stabilize within 1 second. The nonlinear simulation of the system with full state feedback and with output observer feedback is shown in Figure 7.18. The output feedback gives satisfactory performance in both y_{H_2} and T_{cpox} regulations.
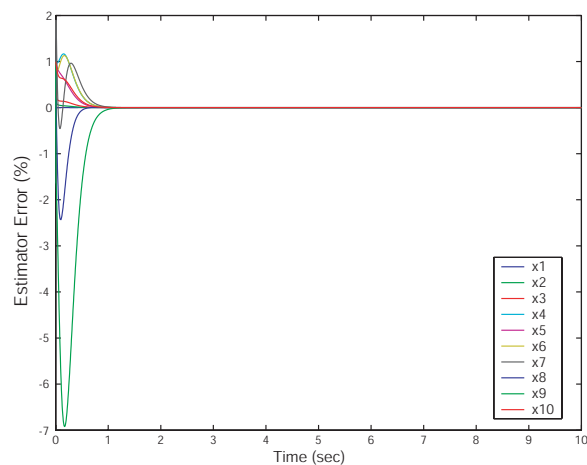
Figure 7.17: Estimator error for 1% initial error
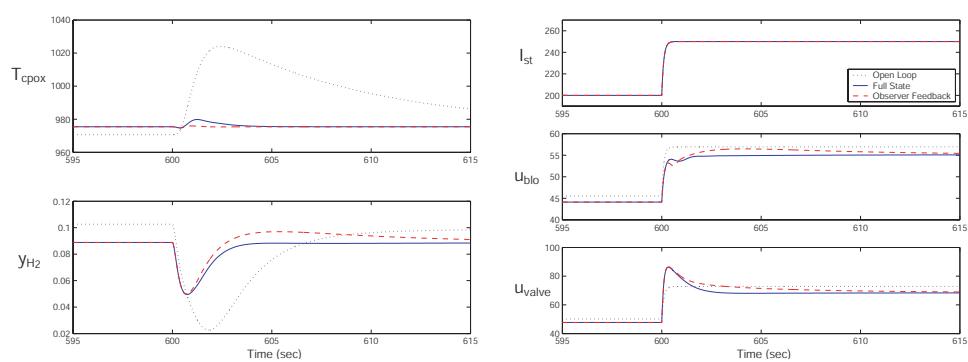
Figure 7.18: Comparison of full state feedback and estimated state feedback using perfect measurements

7.5.3   Insight into a Better Performance of MIMO Controller

The combination of the state feedback control and the state observer results in a model-based multivariable output-feedback controller. The state space representation of the controller can be written as

$$
\begin{bmatrix} \dot{\hat{x}} \\ \dot{q} \end{bmatrix} = \begin{bmatrix} A - B_u K - L C_z & -B_u K_I \\ 0 & 0 \end{bmatrix} \begin{bmatrix} \hat{x} \\ q \end{bmatrix} + \begin{bmatrix} B_w + B_u K_P \alpha_d & L \\ 0 & -I \end{bmatrix} \begin{bmatrix} w \\ z \end{bmatrix}
$$

$$
u = \begin{bmatrix} -K_p - K_I \end{bmatrix} \begin{bmatrix} \hat{x} \\ q \end{bmatrix} + \begin{bmatrix} K_p \alpha_d & 0 \end{bmatrix} \begin{bmatrix} w \\ z \end{bmatrix} \tag{7.28}
$$

where the output of the controller is the plant input, $u = \begin{bmatrix} u_{blo} & u_{valve} \end{bmatrix}^T$. Variable α_d is equal to the coefficient of x_d in Equation (7.13). Note that Equation (7.28) is formed taking into account that $D_{zu} = D_{zw} = 0$. In transfer function form, the controller can be written as

$$
u = C_{uw} w + C_{uz} z = \begin{bmatrix} C_{w1} \\ C_{w2} \end{bmatrix} w + \begin{bmatrix} C_{11} & C_{12} \\ C_{21} & C_{22} \end{bmatrix} z \tag{7.29}
$$

The Bode plot of each element of the controller, C, is shown in Figure 7.19. The C_{uw} term is an additional dynamic feedforward that is superimposed on the original static feedforward u^* in (7.1). The term C_{uz} is the feedback part of the controller.
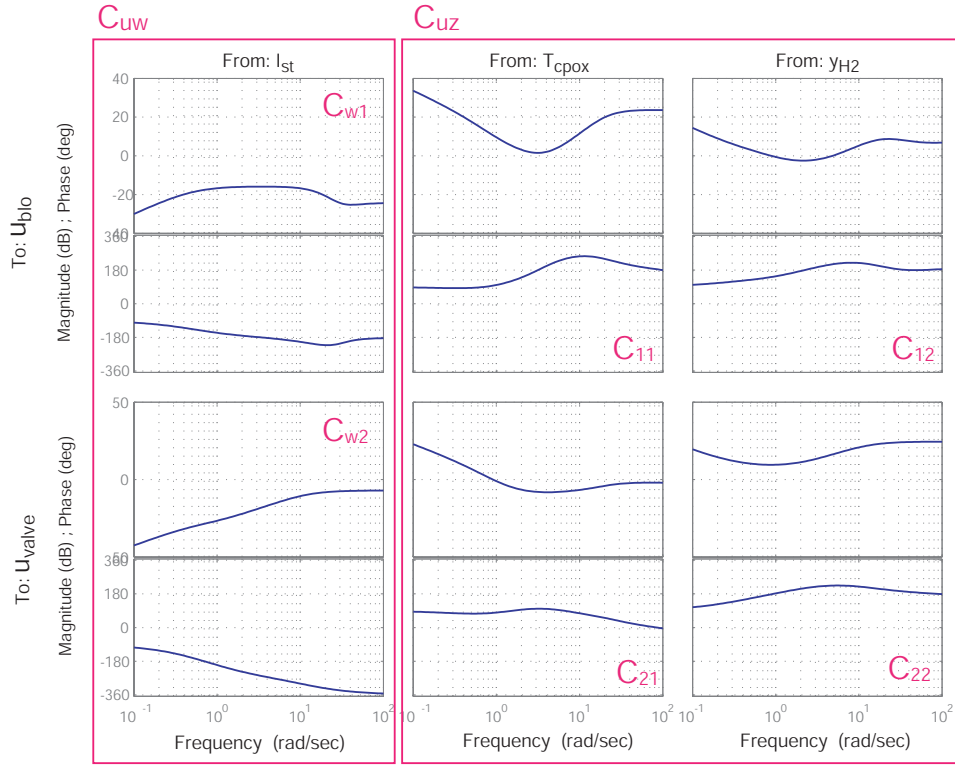
Figure 7.19: Frequency response of the controller

In an effort to simplify the feedback controller for gain scheduling and implementation purposes, we investigate which cross-coupling term of the feedback contributes to the improvement by the MIMO controller. By zeroing out the cross-coupling term and plotting the closed loop frequency and time responses in Figures 7.20 and 7.21, we can see that the performance of the full controller is maintained when $C_{21} = 0$. However, the performance degrades when $C_{12} = 0$ and thus it is clear that the C_{12} term

is the critical cross-coupling term that provides the MIMO control improvement. This analysis gives a different result, however, if the blower bandwidth is allowed to be higher as shown in Figures 7.22 and 7.23. These plots are generated by lowering the LQ weight on u_{blo} in the state feedback design, i.e., $R(1,1) = 1$ in (7.14). There is more actuator activity (high bandwidth controller) of u_{blo}, as shown in Figure 7.22, and the diagonal controller ($C_{12} = C_{21} = 0$) performs similarly to the full multivariable controller.
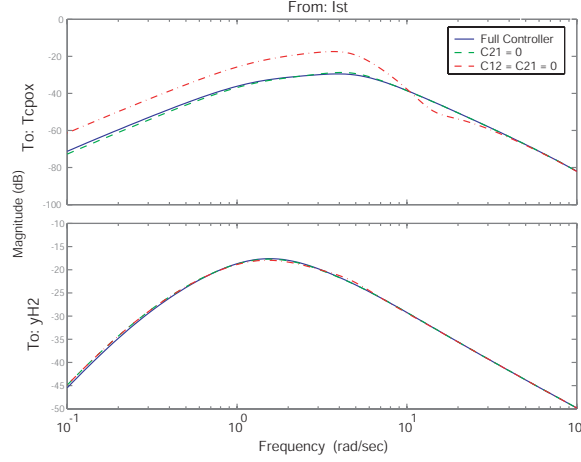
Figure 7.20: Closed-loop frequency response for analysis of elements in the feedback controllers
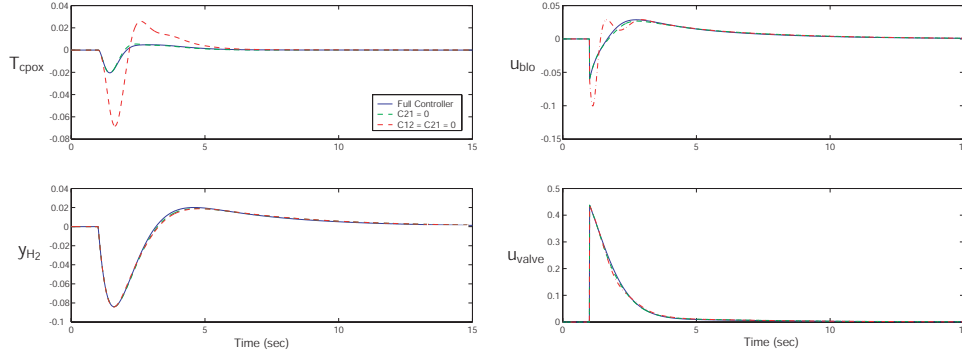
Figure 7.21: Closed-loop time response for analysis of elements in the feedback controllers

The importance of C_{12} when high control bandwidth in u_{blo} is not feasible is interpreted as follows. Following Figure 7.25, the current disturbance, I_{st}, almost instantaneously affects y_{H_2} during fast transient as can be seen by the large high-frequency magnitude of the transfer function from I_{st} to y_{H_2} (Figure 7.24) for the plant with feedforward control:

$$\tilde{G}_{zw} = G_{zw} + G_{zu}C_{uw} \tag{7.30}$$

On the contrary, the magnitude of the I_{st} to T_{cpox} transfer function is very low at high frequencies. The valve signal, u_{valve}, tries to reject the effect of $\tilde{G}_{w2} \times w$ to y_{H_2} (see Figure 7.25) by using the feedback C_{22} term through G_{22}. The blower signal, on the other hand, cannot help reject the $\tilde{G}_{w2} \times w$ to y_{H_2} through the $G_{21} \times C_{12}$ because of the non-minimum phase zero of the G_{21}. Meanwhile, the valve that tries hard to reject the $\tilde{G}_{w2} \times w$ to y_{H_2} causes disturbances to T_{cpox} through the G_{12} cross-coupling term. The controller cross-coupling term C_{12} is thus needed to compensate for the effect of u_{valve} to T_{cpox}. If the blower has high bandwidth, the $G_{11} \times C_{11}$ term can reject the disturbance by itself. Thus, controller C_{12} is not needed to cancel the $G_{12} \times C_{22}$ effect.
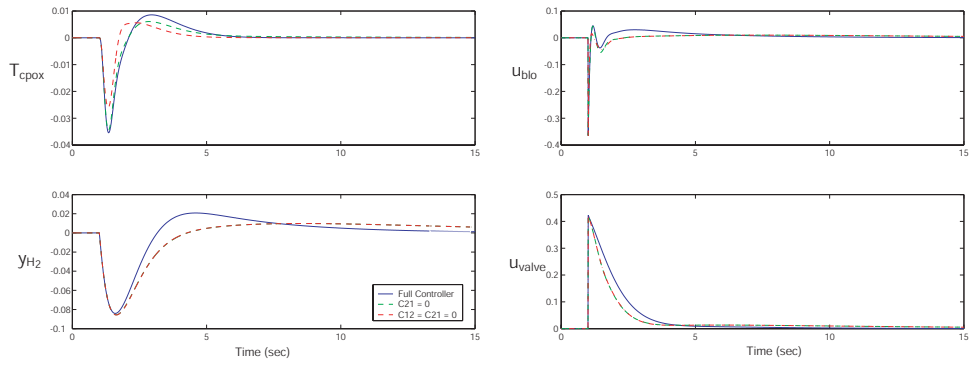
Figure 7.22: Closed-loop time response for analysis of elements in the feedback controllers assuming high-bandwidth blower
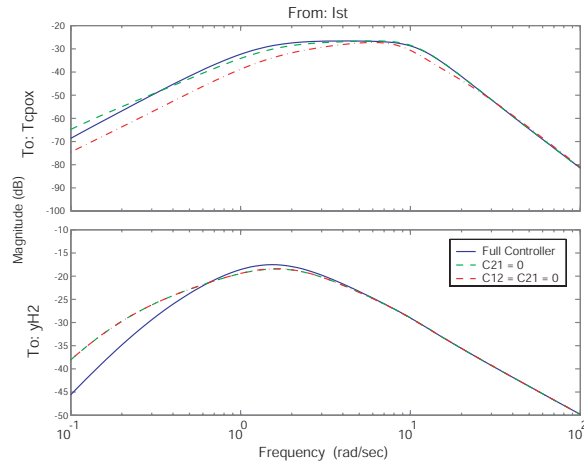
Figure 7.23: Closed-loop frequency response for analysis of elements in the feedback controllers assuming high-bandwidth blower
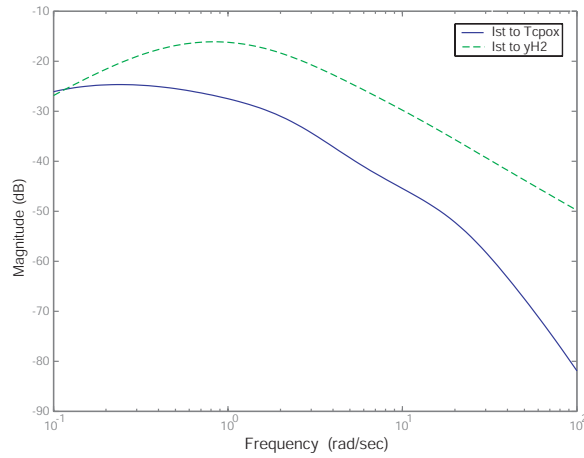
Figure 7.24: Frequency magnitude plot of the plant with dynamic feedforward part of the controller $\tilde{G}_{zw}$ in (7.30)
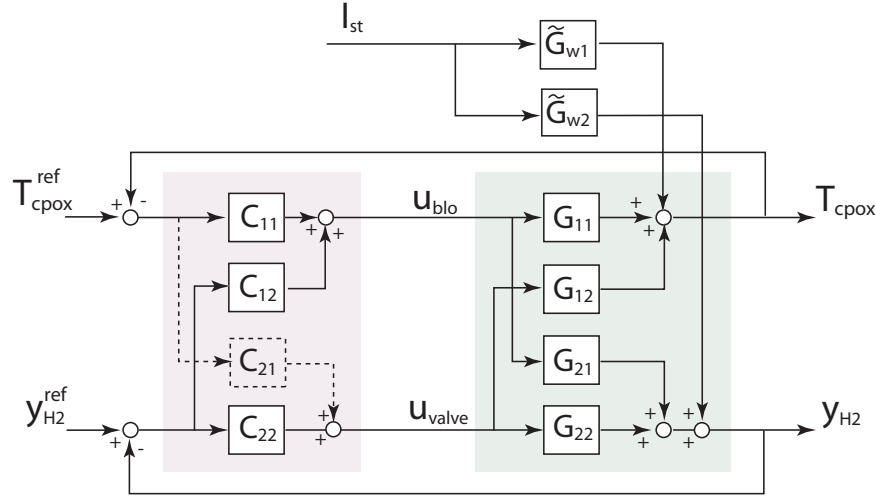
Figure 7.25: Block Diagram of FPS plant and simplified controller; comparing this structure with the one showing in Figure 7.6

7.5.4   Effect of Measurements

In practice, the CPOX temperature measurement and anode hydrogen mole fraction can not be instantaneously measured. The temperature and hydrogen sensors are normally slow, with time constants of approximately 40 seconds and 10 seconds [54], respectively. In this section, we show that the lag in the measurements can potentially degrade the estimator performance, and thus the feedback bandwidth must be detuned in favor of robustness. For fast response, the system has to rely more on feedforward control of the fuel valve and the blower command based on the measured exogenous input, I_{st}. The feedforward controller, in turn, depends on the actuator response and reliability. A common method to speed up and robustify actuator performance is a cascade configuration of a 2DOF controller for each actuator based on measurement of the air flowrate, W_{air}, and the fuel flowrate, W_{fuel} (both in g/sec). The cascade controller architecture in Figure 7.26 shows a decentralized version of the cascade controller. The decentralized version, which is very popular in industrial settings [85], uses feedforward and PI controllers to achieve the desired fuel and air flows.
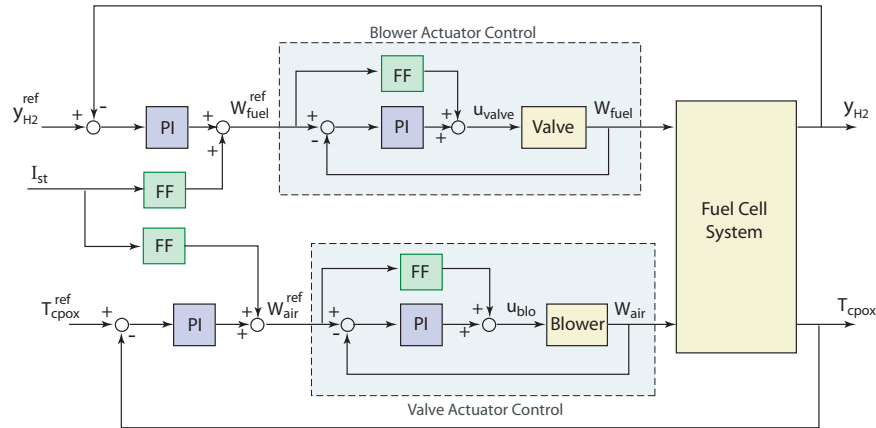
Figure 7.26: Typical FPS control configuration

Two additional dynamic states are added to the plant when we consider the dynamics of the sensors. Two sensor state equations that are augmented to the plant (Equation (7.3)) are

$$\begin{bmatrix} \dot{s_T} \\ \dot{s_H} \end{bmatrix} = \begin{bmatrix} -0.025 & 0 \\ 0 & -0.01 \end{bmatrix} \begin{bmatrix} s_T \\ s_H \end{bmatrix} + \begin{bmatrix} 0.025 & 0 \\ 0 & 0.01 \end{bmatrix} \begin{bmatrix} T_{cpox} \\ y_{H_2} \end{bmatrix} \tag{7.31}$$

where S_T is the CPOX temperature sensor state and S_H is the hydrogen sensor state. The order of the plant and sensor dynamics is 12 (10 for the plant and 2 for the sensors).

$$x_s = \begin{bmatrix} x^T & s_T & s_H \end{bmatrix}^T \tag{7.32}$$

where x is from Equation (7.3). The measurements are

$$y = \begin{bmatrix} T_{cpox}^m & y_{H_2}^m & W_{air} & W_{fuel} \end{bmatrix}^T = C_y x_1 + D_{yu} u + D_{yw} w \tag{7.33}$$

where T_{cpox}^m and $y_{H_2}^m$ are the measured value of T_{cpox} and y_{H_2}, respectively. The matrices in (7.33) are shown in Equation A.7 in the Appendix.

Each set of measurements provides a different degree of observability as can be seen by comparing the normalized condition number of the observability gramian in Table 7.5. The lag contributed by the sensors significantly degrades the system observability. However, adding the fuel and air flow measurements lowers the observability condition number to a value lower than the one obtained with perfect measurement of T_{cpox} and y_{H_2}. We can, thus, expect a better estimation performance. Even better estimation can be expected if additional measurements such as mixer pressure are available, as shown in the table below. More work is needed to define the critical measurements that will be beneficial for the observer-based controller.

Table 7.5: Normalized condition number of observability gramian

Measurements	Condition Number
T_{cpox}, y_{H_2}	2×10^5
T_{cpox}^m, $y_{H_2}^m$	1.348×10^{10}
T_{cpox}^m, $y_{H_2}^m$, W_{air}, W_{fuel}	3672.7
T_{cpox}^m, $y_{H_2}^m$, W_{air}, W_{fuel}, p^{mix}	1928.8

Chapter 8

Conclusions

A satisfactory transient behavior is one of the critical requirements of the fuel cell system for both automotive and residential applications. A well-designed control system is needed in order to provide fast and consistent transient behavior of the fuel cell system. The system consists of four main subsystems, namely, reactant supply, heat and temperature, water management, and power management subsystems. Additional complexities arise for the system with a hydrogen fuel processor that converts carbon-based fuel into hydrogen. Interactions among the subsystems lead to a complex control problem.

Two control problems related to the fuel cell system are presented in this thesis. The first problem is the control of the cathode oxygen reactant for a high-pressure direct hydrogen fuel cell system (FCS). The control goal is to effectively regulate the oxygen concentration in the cathode by replenishing fast and accurately the oxygen depleted during power generation. The second problem is the multi-input multi-output control of a low-pressure partial-oxidation based natural gas fuel processor system (FPS). The control objectives are to regulate both catalytic partial oxidation (CPOX) temperature and anode hydrogen concentration. System dynamic analysis and control design are carried out using the model-based linear control approach.

A control oriented nonlinear dynamic model suitable for each control problem is developed from physics-based principles. Not only are they easily scalable and expandable, but the system level dynamic models built from physics-based component models are also very useful in understanding system behaviors and interactions and in designing the model-based controller. The models of the FCS and FPS are developed using physical principles such as chemical reaction, electrochemistry, thermodynamics, mechanics, and lumped parameter fluid dynamic principles. The transient behaviors captured in the model include flow characteristics, inertia dynamics, manifold filling dynamics, time evolving reactant pressure or mole fraction, membrane humidity, and the relevant CPOX converter temperature.

8.1   Fuel Cell Stack System

The stack voltage is calculated based on time varying load current, cell temperature, air pressure, oxygen and hydrogen partial pressure, and membrane humidity. The fuel cell voltage is determined using a polarization curve based on the reversible cell voltage, activation losses, ohmic losses, and concentration losses. Flow equations, mass conservation, and electrochemical relations were used to calculate changes in partial pressures and the humidity of the gas in the fuel cell stack flow channels. The FCS model contains nine states representing the masses of various gases inside the component volumes.

In this study, we focus on the control of the cathode oxygen supply. For this purpose, a proportional controller for the hydrogen flow and an ideal controller for the humidifier are incorporated into the FCS model. The hydrogen flow control ensures a minimum pressure difference between the anode

and the cathode channels while the humidifier control ensures a fixed humidity of the air entering the stack. Furthermore, perfect conditions of temperature and humidity are assumed at several places in the model, for example, the temperature and humidity of the inlet air, of the inlet hydrogen, and of the cell membrane. The control input is the compressor command. The performance variable is the oxygen excess ratio, which is defined as the ratio between oxygen supplied to the cathode and oxygen used in the reaction.

The steady-state optimal value of the oxygen excess ratio is around 2 for the FCS considered in this study. The value is obtained from a steady-state analysis of the nonlinear FCS model. Operating the system at the optimal value ensures that the maximum net power is achieved for a specific current load. This value also agrees with the fuel cell specification and its desired operating point given in the literature, thus validating indirectly the accuracy of our model.

Features and properties of different control configurations such as dynamic feedforward, observer feedback, and proportional plus integral are presented. The advantages and disadvantages, such as simplicity and robustness, of each configuration are succinctly explained. Depending on the characteristics of the fuel cell system and the system model, such as source of unknown disturbance, degree of parameter variations, and/or model accuracy, a control engineer can select the most suitable control configuration.

Control performance limitations due to sensor availability are also illustrated. The performance variable, i.e., the oxygen excess ratio, λ_{O_2}, itself, cannot be measured. The compressor flow rate, which is located upstream of the λ_{O_2} location is used. The fact that W_{cp} is measured instead of λ_{O_2} limits the uses of integral control. The two main reasons are as follows: First, the reference value needs to be calculated from a known atmospheric condition, which in reality varies. Second, a large integral gain cannot be used as it enforces a fast compressor response to the setpoint upstream of the manifold filling volume, and thus slows down the λ_{O_2} response.

Using the stack voltage measurement as one of the feedback signals to the controller increases the system observability. Voltage is currently used for monitoring, diagnostic, and emergency shut-down procedures. The observability analysis presented suggests that the voltage should be used in the feedback, especially for estimation purposes.

There is a tradeoff between fast regulation of the oxygen excess ratio and fast delivery of the desired net power during transient operations. The conflict arises from the fact that the compressor is using part of the stack power to accelerate. The tradeoff is shown to be associated with frequencies between 0.11 to 3.2 Hz for the FCS in this study. One way to resolve this conflict is to augment the FCS with an auxiliary battery or an ultra-capacitor that can drive the auxiliary devices or can potentially filter current demand to frequencies lower than 0.11 Hz.

8.2   Natural Gas Fuel Processor System

A low-order (10 states) model of the FPS is developed with a focus on the dynamic behavior associated with the flow and the pressures in the FPS and the temperature of the CPOX. The effects of both CPOX temperature and O_2 to CH_4 ratio on the CPOX reaction are included. The FPS model is parameterized and validated with a high-order detailed fuel cell system model. The model allows us to analyze the FPS control problem. Specifically, the FPS two-input two-output (TITO) control problem has the air blower and the fuel valve as inputs and the CPOX temperature and the anode hydrogen mole fraction as performance variables.

A typical control configuration for the FPS system is a decentralized control where the air blower is paired with the CPOX temperature and the fuel valve command is paired with the anode hydrogen mole fraction. A relative gain array (RGA) analysis justifies this pairing for the decentralized control. However, the study shows large plant interactions at high frequencies, which degrade the decentralized control performance during transient. Moreover, plant interactions measured by the RGA increase when the system is operated at low power. The effects of interactions are illustrated by implementing simple PI controllers for each decentralized loop.

The model-based multivariable controller designed using the linear quadratic (LQ) optimal method

gives a significant improvement in the CPOX temperature regulation as compared to the decentralized controller. During load (current) changes, the regulation of the anode H_2 mole fraction depends strongly on the speed and the magnitude of the fuel valve command, while the CPOX temperature regulation depends on the coordination of the two inputs.

Analysis of the MIMO control architecture shows that the controller can be simplified into a triangular controller. One of the controller cross-coupling terms is found to be effective and contributes largely to the performance of the MIMO controller. The controller cross-coupling term from the anode H_2 mole fraction to the blower command significantly contributes to the performance of the controller. This result is very useful for implementation purposes. Moreover, we also provide physical insights into the reasons for the multivariable controller performance superiority.

Additional measurements are needed if the MIMO controller is to be implemented with realistic sensors that have slow dynamics. The observability analysis can help in assessing the relative cost-benefit ratio for adding extra sensors in the system.

8.3 Future Study

Modeling: Even though the FCS model behavior agrees with several experimental results published in the literature, the model and its parameters have not yet been verified with experimental data from an actual fuel cell system. An extensive model validation is needed to increase the model fidelity. Each component model, such as the compressor, the blower, or the manifolds, can be validated with the actual component separately. A considerable amount of validation is also needed for the stack model, especially for the parameters related to the humidity, for example, those used to calculate the water transfer rate across the membrane and those used to calculate the effects of membrane humidity on the cell voltage. These parameters can be validated with an experiment on a single cell or a single membrane. Other parameters, such as the orifice constant, need to be obtained from a stack level experiment.

The fuel cell voltage also depends on the liquid water residing in the fuel cell stack. Accumulation of liquid water in the fuel cell, also know as a "flooding phenomenon" needs to be included in the model. Several publications [13, 15, 76] suggested that cathode water flooding can significantly reduce the fuel cell performance since it decreases the porosity of the electrode, which affects the diffusion ability of the gas. Temperature changes also have a significant impact on the humidity of the gases and the membrane. The temperature effects need to be taken into account in the model by either developing dynamic models of the gas and stack temperatures or, if the temperature dynamics is considered slow, analyzing the system behavior at different temperature setpoints.

A substantial amount of information is lost when using the lumped parameter models. Important fuel cell variables such as partial pressures and temperature are, in fact, spatially distributed along the flow channel. As a result, the current density is not uniformly distributed over the fuel cell area. The effect of spatial variation needs to be included in the model especially if the model is to be used for estimation purposes. Flow pattern must also be incorporated to improve estimation accuracy.

FC stack control: Several interesting control problems can be addressed using the existing model. In a typical fuel cell operation, extra hydrogen is supplied to the stack in order to avoid hydrogen starvation at the end of the anode channel. Thus, there is always unused hydrogen leaving the stack. To make use of the remaining hydrogen, the anode re-circulation, in which the exit hydrogen flow is re-routed to the anode inlet flow, is implemented similarly to that in the P2000 system [1]. This re-circulation improves the steady-state hydrogen utilization, thus system efficiency. However, the re-circulation may magnify the difficulties in controlling the anode hydrogen concentration during transient. This is due to the additional volume associated with the re-circulation. It might be interesting to analyze the dynamic behavior of the anode re-circulation process and the tradeoffs associated with the steady-state and transient operations.

The problem of finding a steady-state optimal oxygen excess ratio will be useful in enhancing the efficiency of the fuel cell system. The optimal value of the excess ratio varies with different operating loads and may change depending on system age and environmental conditions. Extremum-seeking or

other maximum-finding techniques can be used to search online for the optimum excess ratio levels.

FPS control: The two main assumptions of the FPS model used in the control study are: 1) full conversion of CH_4 and 2) a combined lumped volume of the water gas shift (WGS) and preferential oxidation (PROX) reactors. It is desirable to eliminate these FPS assumptions in order to improve the fidelity of the model. However, if the first assumption is relaxed, the FPS model will become highly nonlinear with respect to the O_2 to CH_4 ratio and the CPOX temperature. Thus, nonlinear techniques are needed to analyze and design the controller for the system. The assumption on the WGS and the PROX volume may result in erroneous predictions of the anode variables. Separate dynamic models of the two reactors can be integrated into the current FPS model, which will result in additional model complexity. The FPS control problem will become more complicated with additional control inputs (WGS water and PROX air flow). Furthermore, the problem becomes even more challenging if the supply of PROX air flow is shared with that of the CPOX air flow, which represents a system with space and cost limitations, typical in mobile applications.

Appendix A

Miscellaneous Equations, Tables, and Figures

A.1 FCS Air Flow Control Design

This section presents the tables, figures, and equations related to the FCS control design presented in Chapter 5. Tables A.1 and A.2 show the system matrices obtained by linearizing the FCS nonlinear model with and without static feedforward. Figure A.1 shows that the responses from nonlinear and linearized models agree very well.

Table A.1: Linearization results without static feedforward

A

-6.30908	0	-10.9544	0	83.74458	0	0	24.05866
0	-161.083	0	0	51.52923	0	-18.0261	0
-18.7858	0	-46.3136	0	275.6592	0	0	158.3741
0	0	0	-17.3506	193.9373	0	0	0
1.299576	0	2.969317	0.3977	-38.7024	0.105748	0	0
16.64244	0	38.02522	5.066579	-479.384	0	0	0
0	-450.386	0	0	142.2084	0	-80.9472	0
2.02257	0	4.621237	0	0	0	0	-51.2108

B_u

0
0
0
3.946683
0
0
0
0

B_w

-0.03159
-0.00398
0
0
0
0
-0.05242
0

C_z

-2.48373	-1.9773	0.109013	-0.21897	0	0	0	0
-0.63477	0	-1.45035	0	13.84308	0	0	0

D_{zu}

0.169141
0

D_{zw}

-0.0108
-0.01041

C_y

0	0	0	5.066579	-116.446	0	0	0
0	0	0	0	1	0	0	0
12.96989	10.32532	-0.56926	0	0	0	0	0

D_{yu}

0
0
0

D_{yw}

0
0
-0.29656

The eigenvalues of the FCS linear plant are

$$\lambda = \begin{bmatrix} -219.63 & -89.485 & -46.177 & -22.404 & -18.265 & -2.9161 & -1.6474 & -1.4038 \end{bmatrix} \tag{A.1}$$

The required compressor flow rate that satisfy the desired oxygen excess ratio can be calculated from

$$W_{cp} = (1 + \omega_{atm}) W_{air} \tag{A.2}$$

$$= \left(1 + \frac{M_v}{M_a} \frac{p_{sat}(T_{atm})}{p_{atm} - p_{sat}(T_{atm})}\right) \frac{1}{x_{O_2}} \lambda_{O_2} M_{O_2} \frac{nI}{4F} \tag{A.3}$$

where ω_{atm} is the humidity ratio of the atmospheric air, W_{air} is the required mass flow rate of dry air, M_a is the dry air molar mass, x_{O_2} is the oxygen mass fraction in dry air. If the mole fraction of oxygen in the dry air is 0.21, the value of M_a and x_{O_2} are 28.84×10^{-3} kg/mol and 0.23301, respectively.

Table A.2: Linearization results including static feedforward

A

-6.30908	0	-10.9544	0	83.74458	0	0	24.05866
0	-161.083	0	0	51.52923	0	-18.0261	0
-18.7858	0	-46.3136	0	275.6592	0	0	158.3741
0	0	0	-17.3506	193.9373	0	0	0
1.299576	0	2.969317	0.3977	-38.7024	0.105748	0	0
16.64244	0	38.02522	5.066579	-479.384	0	0	0
0	-450.386	0	0	142.2084	0	-80.9472	0
2.02257	0	4.621237	0	0	0	0	-51.2108

B_u

0
0
0
3.942897
0
0
0
0

B_w

-0.03159
-0.00398
0
2.681436
0
0
-0.05242
0

C_z

-2.48373	-1.9773	0.109013	-0.21897	0	0	0	0
-0.63477	0	-1.45035	0	13.84308	0	0	0

D_{zu}

0.168979
0

D_{zw}

0.104116
-0.01041

C_y

0	0	0	5.066579	-116.446	0	0	0
0	0	0	0	1	0	0	0
12.96989	10.32532	-0.56926	0	0	0	0	0

D_{yu}

0
0
0

D_{yw}

0
0
-0.29656

Figure A.1: Comparison of FCS responses between nonlinear and linear models

The observer gain here is used in (5.25) for the FCS system observer.

$$L = \begin{bmatrix} 17.667 & -0.31359 & 2785.1 \\ -9.1023 & 5.9184 & 20.78 \\ 23.741 & 99.245 & -247.9 \\ 8159.8 & 446.15 & 1496 \\ -20.122 & 19.43 & 54.645 \\ -155.13 & 265.91 & 1057 \\ -72.553 & 5.7114 & -31.406 \\ 7.2343 & 6.6423 & 65.186 \end{bmatrix} \tag{A.4}$$

A.2   FPS Control Design

Table A.3 shows the matrices of the linearized FPS model with static feedforward included and Figure A.2 shows the responses from both linear and nonlinear model.

Table A.3: FPS linear model system matrices

A

-0.074	0	0	0	0	0	-3.53	1.0748	0	1E-06
0	-1.468	-25.3	0	0	0	0	0	2.5582	13.911
0	0	-156	0	0	0	0	0	0	33.586
0	0	0	-124.5	212.63	0	112.69	112.69	0	0
0	0	0	0	-3.333	0	0	0	0	0
0	0	0	0	0	-32.43	32.304	32.304	0	0
0	0	0	0	0	331.8	-344	-341	0	9.9042
0	0	0	221.97	0	0	-253.2	-254.9	0	32.526
0	0	2.0354	0	0	0	1.8309	1.214	-0.358	-3.304
0.0188	0	8.1642	0	0	0	5.6043	5.3994	0	-13.61

Bu

0	0
0	0
0	0
0	0
0.12	0
0	0.1834
0	0
0	0
0	0
0	0

Bw

0
-0.328
-0.024
0
0.0265
0.0504
0
0
0
0

Cz

1	0	0	0	0	0	0	0	0	0
0	0.994	-0.088	0	0	0	0	0	0	0

Dzu

0	0
0	0

Dzw

0
0
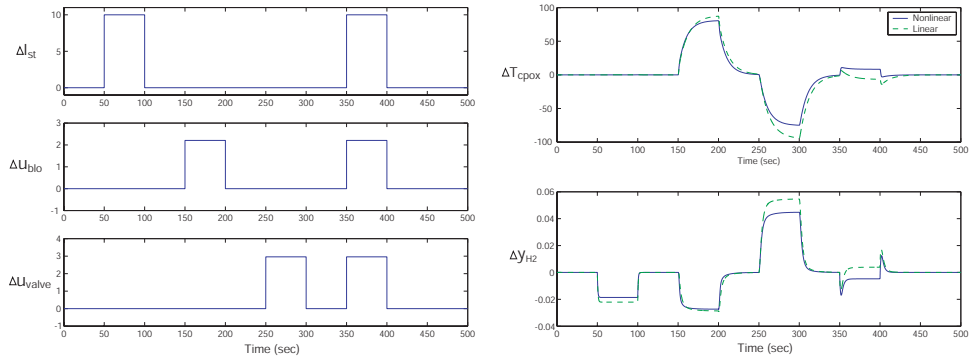
Figure A.2: Comparison of FPS responses between nonlinear and linear models

The closed loop eigenvalues of the FPS system in Section 7.5.1 are

$$\lambda(A_a - B_a K) = \begin{bmatrix} -660.66 \\ -157.92 \\ -89.097 \\ -12.174 \\ -5.8954 \\ -3.0122 + 3.8238i \\ -3.0122 - 3.8238i \\ -1.3514 + 0.6979i \\ -1.3514 - 0.6979i \\ -1.3578 \\ -0.27348 \\ -0.35855 \end{bmatrix} \tag{A.5}$$

Table A.4 shows the FPS system matrices after the state is transformed to the modal canonical form.

Table A.4: FPS linear model system matrices in modal canonical form

A_1

-660.7	0	0	0	0	0	0	0	0	0
0	-89.1	0	0	0	0	0	0	0	0
0	0	-157.9	0	0	0	0	0	0	0
0	0	0	-12.17	0	0	0	0	0	0
0	0	0	0	-3.333	0	0	0	0	0
0	0	0	0	0	-2.782	0.4612	0	0	0
0	0	0	0	0	-0.461	-2.782	0	0	0
0	0	0	0	0	0	0	-1.468	0	0
0	0	0	0	0	0	0	0	-0.358	0
0	0	0	0	0	0	0	0	0	-0.086

B_{1u}

-0.011	0.0646
-0.661	-0.386
-0.001	0.0004
-0.155	0.4411
368.64	0
345.79	-4.027
-378.3	-15.9
-3.555	-1.855
-0.568	0.9745
3.2203	-2.916

B_{1w}

0.0154
-0.251
-0.024
0.0937
81.314
75.166
-87.76
-1.618
0.1421
-0.09

C_{1z}

-0.003	0.0354	-3E-05	-0.248	0.6991	-0.755	0	0	0	0.9999
-2E-04	0.0008	0.0764	0.1414	0.0895	-0.113	-0.027	0.994	0.9119	-0.006

D_{1zu}

0	0
0	0

D_{1zw}

0
0

The observer gain for the FPS estimator with perfect measurements in Section 7.5.2 is

$$L = \begin{bmatrix} 469.67 & 138.59 \\ 5.6245 & 818.34 \\ -93.622 & -12.759 \\ -742.29 & -99.077 \\ -30.245 & -4.7928 \\ -795.89 & -104.2 \\ -2149.2 & -392.69 \\ 1400.7 & 294.09 \\ 1559.8 & 3547.1 \\ -430.89 & -58.728 \end{bmatrix} \tag{A.6}$$

The C and D matrices for the FPS system with realistic measurements are given in (A.7).

$$C_y = \begin{bmatrix} 0 & 0 & 0 & 0 & 0 & 0 & 0 & 0 & 0 & 0 & 1 & 0 \\ 0 & 0 & 0 & 0 & 0 & 0 & 0 & 0 & 0 & 0 & 0 & 1 \\ 0 & 0 & 0 & 0 & 0 & 0 & -4.274 & 77.17 & 0 & 0 & 0 & 0 \\ 0 & 0 & 0 & 0 & 0 & 0 & 0 & -0.135 & 0 & 0 & 0 & 0 \end{bmatrix} \tag{A.7}$$

$$Dyu = \begin{bmatrix} 0 & 0 \\ 0 & 0 \\ 0 & 0 \\ 0 & 0.202 \end{bmatrix} \quad Dyw = \begin{bmatrix} 0 \\ 0 \\ 0 \\ 0.0555 \end{bmatrix}$$

Bibliography

[1] J.A. Adams, W-C Yang, K.A. Oglesby, and K.D. Osborne. The development of Ford's P2000 fuel cell vehicle. *SAE Paper 2000-01-1061*.

[2] S. Ahmed and M. Krumpelt. Hydrogen from hydrocarbon fuels for fuel cells. *International Journal of Hydrogen Energy*, 26:291–301, 2001.

[3] S. Akella, N. Sivashankar, and S. Gopalswamy. Model-based systems analysis of a hybrid fuel cell vehicle configuration. *Proceedings of 2001 American Control Conference*, 2001.

[4] J.C. Amphlett, R.M. Baumert, R.F. Mann, B.A. Peppley, and P.R. Roberge. Performance modeling of the Ballard Mark IV solid polymer electrolyte fuel cell. *Journal of Electrochemical Society*, 142(1):9–15, 1995.

[5] J.C. Amphlett, R.M. Baumert, R.F. Mann, B.A. Peppley, P.R. Roberge, and A. Rodrigues. Parametric modelling of the performance of a 5-kW proton-exchange membrane fuel cell stack. *Journal of Power Sources*, 49:349–356, 1994.

[6] J.C. Amphlett, R.F. Mann, B.A. Peppley, P.R. Roberge, and A. Rodrigues. A model predicting transient responses of proton exchange membrane fuel cells. *Journal of Power Sources*, 61:183–188, 1996.

[7] Brian D. O. Anderson and John B. Moore. *Optimal Control: Linear Quadratic Methods*. Prentice-Hall, New Jersey, 1989.

[8] A.J. Appleby and F.R. Foulkes. *Fuel Cell Handbook*. Van Nostrand Reinhold, New York, 1989.

[9] P. Atwood, S. Gurski, D.J. Nelson, K.B. Wipke, and T. Markel. Degree of hybridization AD-VISOR modeling of a fuel cell hybrid electric sport utility vehicle. *Proceedings of 2001 Joint ADVISOR/PSAT vehicle systems modeling user conference*, pages 147–155, 2001.

[10] P. Badrinarayanan, S. Ramaswamy, A. Eggert, and R.M. Moore. Fuel cell stack water and thermal management: Impact of variable system power operation. *SAE Paper 2001-01-0537*.

[11] F. Barbir, B. Balasubramanian, and J. Neutzler. Trade-off design analysis of operating pressure and temperature in PEM fuel cell systems. *Proceedings of the ASME Advanced Energy Systems Division*, 39:305–315, 1999.

[12] F. Barbir, M. Fuchs, A. Husar, and J. Neutzler. Design and operational characteristics of automotive PEM fuel cell stacks. *SAE Paper 2000-01-0011*.

[13] J.J. Baschuk and X. Li. Modelling of polymer electrolyte membrane fuel cells with variable degrees of water flooding. *Journal of Power Sources*, 86:186–191, 2000.

[14] M. D. Di Benedetto and P. Lucibello. Inversion of nonlinear time-varying systems. *IEEE Transactions on Automatic Control*, 38(8):1259–1264, 1993.

127

[15] D.M. Bernardi. Water-balance calculations for solid-polymer-electrolyte fuel cells. *Journal of Electrochemical Society*, 137(11):3344–3350, 1990.

[16] D.M. Bernardi and M.W. Verbrugge. A mathematical model of the solid-polymer-electrolyte fuel cell. *Journal of the Electrochemical Society*, 139(9):2477–2491, 1992.

[17] D. Bevers, M. Wöhr, K. Yasuda, and K. Oguro. Simulation of a polymer electrolyte fuel cell electrode. *Journal of Applied Electrochemistry*, 27(11):1254–1264, 1997.

[18] S. Birch. Ford's focus on the fuel cell. *Automotive Engineering International*, pages 25–28, June 2001.

[19] D.D. Boettner, G. Paganelli, Y.G. Guezennec, G. Rizzoni, and M.J. Moran. Component power sizing and limits of operation for proton exchange membrane (PEM) fuel cell/battery hybrid automotive applications. *Proceedings of 2001 ASME International Mechanical Engineering Congress and Exposition*, 2001.

[20] D.D. Boettner, G. Paganelli, Y.G. Guezennec, G. Rizzoni, and M.J. Moran. Proton exchange membrane (PEM) fuel cell system model for automotive vehicle simulation and control. *Proceedings of 2001 ASME International Mechanical Engineering Congress and Exposition*, 2001.

[21] Meherwa P. Boyce. *Gas Turbine Engineering Handbook*. Gulf Publishing, Houston, Texas, 1982.

[22] E.H. Bristol. On a new measure of interactions for multivariable process control. *IEEE Transactions on Automatic Control*, AC-11:133–134, 1966.

[23] L.F. Brown. A comparative study of fuels for on-board hydrogen production for fuel-cell-powered automobiles. *International Journal of Hydrogen Energy*, 26:381–397, 2001.

[24] F.N. Büchi and S. Srinivasan. Operating proton exchange membrane fuel cells without external humidification of the reactant gases. *Journal of Electrochemical Society*, 144(8):2767–2772, 1997.

[25] S.H. Chan and H.M. Wang. Thermodynamic analysis of natural-gas fuel processing for fuel cell applications. *International Journal of Hydrogen Energy*, 25:441–449, 2000.

[26] Chi-Tsong Chen. *Linear System Theory and Design*. Oxford University Press, New York, 1998.

[27] D. Chu and R. Jiang. Comparative studies of polymer electrolyte membrane fuel cell stack and single cell. *Journal of Power Sources*, 80:226–234, 1999.

[28] D. Chu and R. Jiang. Performance of polymer electrolyte membrane fuel cell (PEMFC) stacks, part I evaluation and simulation of an air-breathing PEMFC stack. *Journal of Power Sources*, 83:128–133, 1999.

[29] Ford Motor Company. Fuel cell power system (FCPS) spreadsheet model.

[30] J.M. Cunningham, M.A Hoffman, R.M Moore, and D.J. Friedman. Requirements for a flexible and realistic air supply model for incorporation into a fuel cell vehicle (FCV) system simulation. *SAE Paper 1999-01-2912*.

[31] K. Dannenberg, P. Ekdunge, and G. Lindbergh. Mathematical model of the PEMFC. *Journal of Applied Electrochemistry*, 30:1377–1387, 2000.

[32] S.C. Davis. *Transportation Energy Data Book*. DOE, 2000.

[33] C.R.H. de Smet, M.H.J.M. de Croon, R.J. Berger, G.B. Marin, and J.C. Schouten. Design of adiabatic fixed-bed reactors for the partial oxidation of methane to synthesis gas. Application to production of methanol and hydrogen-for-fuel-cells. *Chemical Engineering Science*, 56:4849–4861, 2001.

[34] S. Devasia. Should model-based inverse inputs be used as feedforward under plant uncertainty? *IEEE Transactions on Automatic Control*, 41(11):1865–1871, 2002.

[35] S. Devasia, D. Chen, and B. Paden. Nonlinear inversion-based output tracking. *IEEE Transactions on Automatic Control*, 41(7):930–942, 1996.

[36] A.L. Dicks. Hydrogen generation from natural gas for the fuel cell systems of tomorrow. *Journal of Power Sources*, 61:113–124, 1996.

[37] E.D. Doss, R. Kumar, R.K. Ahluwalia, and M. Krumpelt. Fuel processors for automotive fuel cell systems: a parametric analysis. *Journal of Power Sources*, 102:1–15, 2001.

[38] J. C. Doyle and G. Stein. Robustness with observers. *Transactions on Automatic Control*, AC-24(4):607–611, 1979.

[39] S. Dutta, S. Shimpalee, and J.W. Van Zee. Numerical prediction of mass-exchange between cathode and anode channels in a PEM fuel cell. *International Journal of Heat and Mass Transfer*, 44:2029–2042, 2001.

[40] J. Eborn, L.M. Pedersen, C. Haugstetter, and S. Ghosh. System level dynamic modeling of fuel cell power plants. *to be presented in 2003 American Control Conference*, 2003.

[41] EPA. *Latest Findings on National Air Quality*, 2000.

[42] B.A. Francis and W.M. Wonham. The internal model principle of control theory. *Automatica*, 12(5):457–465, 1976.

[43] Gene F. Franklin, J. David Powell, and Abbas Emani-Naeini. *Feedback Control of Dynamic Systems*. Addison-Wesley, New York, 1994.

[44] J.S. Freudenberg. A first graduate course in feedback control, 2002. University of Michigan, EECS 565 Coursepack.

[45] D.J. Friedman, A. Egghert, P. Badrinarayanan, and J. Cunningham. Balancing stack, air supply and water/thermal management demands for an indirect methanol PEM fuel cell system. *SAE Paper 2001-01-0535*.

[46] M.H. Fronk, D.L. Wetter, D.A. Masten, and A. Bosco. PEM fuel cell system solutions for transportation. *SAE Paper 2000-01-0373*.

[47] M. Fuchs, F. Barbir, A. Husar, J. Neutzler, D.J. Nelson, M. Ogburn, and P. Bryan. Performance of automotive fuel cell stack. *SAE Paper 2000-01-1529*.

[48] T.F. Fuller and J. Newman. Water and thermal management in solid-polymer-electrolyte fuel cells. *Journal of Electrochemical Society*, 140(5):1218–1225, 1993.

[49] T.H. Gardner, D.A. Berry, K.D. Lyons, S.K. Beer, and A.D. Freed. Fuel processor integrated H_2S catalytic partial oxidation technology for sulfur removal in fuel cell power plants. *Fuel*, 81:2157–2166, 2002.

[50] T.T. Georgiou and M.C. Smith. Optimal robustness in the gap metric. *IEEE Transactions on Automatic Control*, 35(6):673–686, 1990.

[51] H.K. Geyer, R.K. Ahluwalia, and R. Kumar. Dynamic response of steam-reformed, methanol-fueled, polymer electrolyte fuel cell systems. *Proceedings of the Intersociety Energy Conversion Engineering Conference*, 2:1101–1106, 1996.

[52] R.S. Glass. Sensor needs and requirements for fuel cells and CIDI/SIDI engines. Technical report, Department of Energy, April 2000. Published by Lawrence Livermore National Laboratory.

[53] Jan Tommy Gravdahl and Olav Egeland. *Compressor Surge and Rotating Stall*. Springer, London, 1999.

[54] The Argus Group. Hydrogen sensor for automotive fuel cells from the Argus Group. *http://www.fuelcellsensor.com/*, 2001.

[55] W.R. Grove. A small voltaic battery of great energy. *Philosophical Magazine*, 15:287–293, 1839.

[56] V. Gurau, H. Liu, and S. Kakac. Mathematical model for proton exchange membrane fuel cells. *Proceedings of the 1998 ASME Advanced Energy Systems Division*, pages 205–214, 1998.

[57] L. Guzzella. Control oriented modelling of fuel-cell based vehicles. *Presentation in NSF Workshop on the Integration of Modeling and Control for Automotive Systems*, 1999.

[58] K-H Hauer, D.J. Friedmann, R.M. Moore, S. Ramaswamy, A. Eggert, and P. Badrinarayana. Dynamic response of an indirect-methanol fuel cell vehicle. *SAE Paper 2000-01-0370*.

[59] John B. Heywood. *Internal Combustion Engine Fundamentals*. McGraw-Hill, New York, 1988.

[60] R. Jiang and D. Chu. Stack design and performance of polymer electrolyte membrane fuel cells. *Journal of Power Sources*, 93:25–31, 2001.

[61] R. Jiang and D. Chu. Voltage-time behavior of a polymer electrolyte membrane fuel cell stack at constant current discharge. *Journal of Power Sources*, 92:193–198, 2001.

[62] K. Jost. Fuel-cell concepts and technology. *Automotive Engineering International*, March 2000.

[63] Thomas Kailath. *Linear Systems*. Prentice-Hall, New Jersey, 1980.

[64] F. R. Kalhammer, P. R. Prokopius, V. P. Roan, and G. E. Voecks. Status and prospects of fuel cells as automobile engines. Technical report, State of California Air Resources Board, July 1998.

[65] J. Kim, S-M Lee, and S. Srinivasan. Modeling of proton exchange membrane fuel cell performance with an empirical equation. *Journal of the Electrochemical Society*, 142(8):2670–2674, 1995.

[66] Y-H Kim and S-S Kim. An electrical modeling and fuzzy logic control of a fuel cell generation system. *IEEE Transactions of Energy Conversion*, 14(2):239–244, 1999.

[67] Karl Kordesch and Günter Simader. *Fuel Cells and Their Applications*. VCH, Weinheim, Germany, 1996.

[68] A.L. Larentis, N.S. de Resende, V.M.M. Salim, and J.C. Pinto. Modeling and optimization of the combined carbon dioxide reforming and partial oxidation of natural gas. *Applied Catalysis*, 215:211–224, 2001.

[69] James Larminie and Andrew Dicks. *Fuel Cell Systems Explained*. John Wiley & Sons Inc, West Sussex, England, 2000.

[70] F. Laurencelle, R. Chahine, J. Hamelin, K. Agbossou, M. Fournier, T.K. Bose, and A. Laperriere. Characterization of a Ballard MK5-E proton exchange membrane fuel cell stack. *Fuel Cells Journal*, 1(1):66–71, 2001.

[71] K. Ledjeff-Hey, J. Roses, and R. Wolters. CO_2-scrubbing and methanation as purification system for PEFC. *Journal of Power Sources*, 86:556–561, 2000.

[72] J.H. Lee and T.R. Lalk. Modeling fuel cell stack systems. *Journal of Power Sources*, 73:229–241, 1998.

[73] J.H. Lee, T.R. Lalk, and A.J. Appleby. Modeling electrochemical performance in large scale proton exchange membrane fuel cell stacks. *Journal of Power Sources*, 70:258–268, 1998.

[74] L.E. Lesster. Fuel cell power electronics: Managing a variable-voltage DC source in a fixed-voltage AC world. *Fuel Cells Bulletin*, 2(25):5–9, 2000.

[75] H. Lorenz, K-E Noreikat, T. Klaiber, W. Fleck, J. Sonntag, G. Hornburg, and A. Gaulhofer. Method and device for vehicle fuel cell dynamic power control. *United States Patents 5,646,852*, 1997.

[76] G. Maggio, V. Recupero, and L. Pino. Modeling polymer electrolyte fuel cells: an innovative approach. *Journal of Power Sources*, 101:275–286, 2001.

[77] R.F. Mann, J.C. Amphlett, M. Hooper, H.M. Jensen, B.A. Peppley, and P.R. Roberge. Development and application of a generalized steady-state electrochemical model for a PEM fuel cell. *Journal of Power Sources*, 86:173–180, 2000.

[78] C. Marr and X. Li. Performance modelling of a proton exchange membrane fuel cell. *Proceedings of Energy Sources Technology Conference and Exhibition*, pages 1–9, 1998.

[79] P. Moraal and I. Kolmanovsky. Turbocharger modeling for automotive control applications. *SAE Paper 1999-01-0908*.

[80] Manfred Morari, Evanghelos Zafiriou, and Morari Zafiriou. *Robust Process Control*. Prentice Hall, 1997.

[81] W.E. Mufford and D.G. Strasky. Power control system for a fuel cell powered vehicle. *United States Patents 5,991,670*, 1999.

[82] T.V. Nguyen and R.E. White. A water and heat management model for proton-exchange-membrane fuel cells. *Journal of Electrochemical Society*, 140(8):2178–2186, 1993.

[83] M. Ogburn, D.J. Nelson, W. Luttrell, B. King, S. Postle, and R. Fahrenkrog. Systems integration and performance issues in a fuel cell hybrid electric vehicle. *SAE Paper 2000-01-0376*.

[84] M. Ogburn, D.J. Nelson, K. Wipke, and T. Markel. Modeling and validation of a fuel cell hybrid vehicle. *SAE Paper 2000-01-1566*.

[85] Babatunde A. Ogunnaike and W. Harmon Ray. *Process Dynamics, Modeling, and Control*. Oxford University Press, 1994.

[86] T. Okada, G. Xie, and M. Meeg. Simulation for water management in membranes for polymer electrolyte fuel cells. *Electrochimica Acta*, 43, 1998.

[87] J. Padulles, G.W. Ault, C.A. Smith, and J.R. McDonald. Fuel cell plant dynamic modelling for power systems simulation. *Proceedings of 34th Universities Power Engineering Conference*, 34(1):21–25, 1999.

[88] F. Panik. Fuel cells for vehicle applications in cars - bringing the future closer. *Journal of Power Sources*, 71:36–38, 1998.

[89] L. Pino, V. Recupero, S. Beninati, A.K. Shukla, M.S. Hegde, and P.Bera. Catalytic partial-oxidation of methane on a ceria-supported platinum catalyst for application in fuel cell electric vehicles. *Applied Catalysis A: General*, 225:63–75, 2002.

[90] S. Pischinger, C. Schönfelder, W. Bornscheuer, H. Kindl, and A. Wiartalla. Integrated air supply and humidification concepts for fuel cell systems. *SAE Paper 2001-01-0233*.

[91] K. Rajashekara. Propulsion system strategies for fuel cell vehicles. *SAE Paper 2000-01-0369*.

[92] V. Recupero, L. Pino, R.D. Leonardo, M. Lagana, and G. Maggio. Hydrogen generator, via catalytic partial oxidation of methane for fuel cells. *Journal of Power Sources*, 71:208–214, 1998.

[93] K. Ro and S. Rahman. Control of grid-connected fuel cell plants for enhancement of power system stability. *Renewable Energy*, 28:397–407, 2003.

[94] M. Sadler, A.J. Stapleton, R.P.G. Heath, and N.S. Jackson. Application of modeling techniques to the design and development of fuel cell vehicle systems. *SAE Paper 2001-01-0542*.

[95] D. Singh, D.M. Lu, and N. Djilali. A two-dimensional analysis of mass transport in proton exchange membrane fuel cells. *International Journal of Engineering Science*, 37:431–452, 1999.

[96] Sigurd Skogestad and Ian Postlethwaite. *Multivariable Feedback Control: Analysis and Design*. Wiley, 1996.

[97] R-H Song, C-S Kim, and D.R. Shin. Effects of flow rate and starvation of reactant gases on the performance of phosphoric acid fuel cells. *Journal of Power Sources*, 86:289–293, 2000.

[98] Richard E. Sonntag, Claus Borgnakke, and Gordon J. Van Wylen. *Fundamentals of Thermodynamics*. John Wiley & Sons Inc, fifth edition, 1998.

[99] T.E. Springer, R. Rockward, T.A. Zawodzinski, and S. Gottesfeld. Model for polymer electrolyte fuel cell operation on reformate feed. *Journal of The Electrochemical Society*, 148:A11–A23, 2001.

[100] T.E. Springer, T.A. Zawodzinski, and S. Gottesfeld. Polymer electrolyte fuel cell model. *Journal of Electrochemical Society*, 138(8):2334–2342, 1991.

[101] P. Sridhar, R. Perumal, N. Rajalakshmi, M. Raja, and K.S. Dhathathreyan. Humidification studies on polymer electrolyte membrane fuel cell. *Journal of Power Sources*, 101:72–78, 2001.

[102] R. K. Stobart. Fuel cell power for passenger cars - what barriers remain? *SAE Paper 1999-01-0321*.

[103] The MathWorks, Inc. μ-analysis and synthesis toolbox users guide, 2001.

[104] D. Thirumalai and R.E. White. Mathematical modeling of proton-exchange-membrane fuel-cell stacks. *Journal of Electrochemical Society*, 144(5), 1997.

[105] C.E. Thomas, B.D. James, F.D. Lomax Jr, and I.F. Kuhn Jr. Fuel options for the fuel cell vehicle: hydrogen, methanol or gasoline? *International Journal of Hydrogen Energy*, 25:551–567, 2000.

[106] Sharon Thomas and Marcia Zalbowitz. Fuel cells green power. Technical report, Los Alamos National Laboratory.

[107] B. Thorstensen. A parametric study of fuel cell system efficiency under full and part load operation. *Journal of Power Sources*, 92:9–16, 2001.

[108] Michael Tiller. *Introduction to Physical Modeling with Modelica*. Kluwer Academic Publishers, Boston, 2001.

[109] W. Turner, M. Parten, D. Vines, J. Jones, and T. Maxwell. Modeling a PEM fuel cell for use in a hybrid electric vehicle. *Proceedings of the 1999 IEEE 49th Vehicular Technology Conference*, 2:1385–1388, 1999.

[110] M. Wöhr, K. Bolwin, W. Schnurnberger, M. Fischer, W. Neubrand, and G. Eigenberger. Dynamic modelling and simulation of a polymer membrane fuel cell including mass transport limitation. *International Journal for Hydrogen Energy*, 23(3):213–218, 1998.

[111] W-C Yang, B. Bates, N. Fletcher, and R. Pow. Control challenges and methodologies in fuel cell vehicle development. *SAE Paper 98C054*.

[112] T-H Yanga, Y-G Yoona, C-S Kima, S-H Kwakb, and K-H Yoon. A novel preparation method for a self-humidifying polymer electrolyte membrane. *Journal of Power Sources*, 102:328–332, 2002.

[113] J. Zhu, D. Zhang, and K.D. King. Reforming of CH_4 by partial oxidation: thermodynamic and kinetic analyses. *Fuel*, 80:899–905, 2001.